Operational issues of grid-interactive hybrid microgrid

Gitu Das
Enrolment No. : `ENGE-02-2016` Registration No. : `291887`
Date of Admission : `27/09/2016`

Department of Electrical Engineering
Assam Engineering College

This thesis is submitted to
Gauhati University as requirement for the degree of
Doctor of Philosophy

Faculty of Engineering June 2023

I would like to dedicate this thesis to my teachers, parents, wife, family and friends.

Declaration

I hereby declare that this thesis is the result of my own research work which has been carried out under the guidance of Prof. (Dr.) Durlav Hazarika of Assam Engineering College. I further declare that this thesis as a whole or any part thereof has not been submitted to any university (or institute) for the award of any degree or diploma.

This thesis contains less than 90,000 (ninety thousand) words excluding bibliography and captions.

Gitu Das
June 2023

Certificate

This is to certify that the thesis titled “Operational issues of grid-interactive hybrid microgrid” is the result of research work of Gitu Das, carried under my supervision, submitted to Gauhati University for the award of the degree of Doctor of Philosophy in Electrical Engineering.

This thesis conforms to the standard of PhD Thesis under Gauhati University including the standard related to plagiarism and has a similarity index not more than 20% (twenty percent), excluding the bibliography.

Prof. (Dr.) Durlav Hazarika, Supervisor
June 2023

Dr. D. Agarwal, Electrical Engineering Department, AEC

Dr. A. Bardalai, Electrical Engineering Department, AEC

Dr. B. K. Talukdar, Electrical Engineering Department, AEC

Acknowledgements

I would like to express my deep appreciation to my supervisor, Prof. (Dr.) Durlav Hazarika, Professor, Department of Electrical Engineering, Assam Engineering College. Without his guidance and persistent help, this project would not have been possible. I am truly grateful for his exemplary guidance and encouragement.

I would also like to express my sincere gratitude to the Department of Electrical and Instrumentation Engineering at Assam Engineering College, especially the head of the department, Prof. (Dr.) Aroop Bardalai, and all the faculty members who provided enthusiastic support and encouragement throughout this endeavor.

I would also like to acknowledge the Assam Don Bosco University, especially the department of Electrical and Electronics Engineering for constant help, support and encouragement I received throughout this endeavor.

I am also deeply grateful for the support of my family and friends, who have been a constant source of encouragement throughout this journey.

I would like to express my heartfelt gratitude to my friend, Dr. Jyoti Kumar Barman of Assam Don Bosco University, for providing constant support, encouragement, and guidance throughout this endeavor. His guidance and mentorship have been instrumental in helping me achieve this milestone, and I am truly grateful for his unwavering support.

I am deeply indebted to my late parents who instilled in me the values of hard work and perseverance. They were my guiding light and a constant source of inspiration. Although they are no longer with me, their love and support continue to motivate me every day. I would like to dedicate this achievement to them and express my gratitude for everything they have done for me. I know they would have been proud of me, and I will always cherish their memory.

Finally, I would like to express my heartfelt thanks to my wife, Mrs. Krishna Nath Das, and my daughter, Miss. Ritushna Das, for their constant support and encouragement.

Abstract

The need for decentralized and resilient power systems, coupled with advancements in energy generation and storage technologies, led to the development of hybrid microgrids. While there are several issues facing a hybrid microgrid, the problem of voltage unbalance at the three-phase distribution buses stands out as one of the most significant operational issues in low-voltage hybrid microgrids. It can have severe effects on the operation and lifespan of power system installations, equipment, and home appliances. Therefore, it is necessary to apply corrective measures to keep voltage unbalance within specified limits. The root cause of this unbalance can be mainly attributed to the unbalanced distribution of single-phase loads across the phases. However, non-linear loads and faulty equipment may also contribute to the voltage unbalance in a low-voltage microgrid/distribution system. Existing methods to mitigate voltage unbalance often rely on network parameter information that cannot be directly measured by inverters. Moreover, these methods require additional equipment or hardware modifications, and some heavily rely on communication between distributed generators. To address these limitations, this work proposes a novel perturb-and-observe-based unbalance voltage mitigation strategy suitable for four-leg inverters interfacing distributed generators to low-voltage microgrids. The proposed method involves injecting negative sequence current into the point of inverter connection to the microgrid. A systematic approach is adopted, perturbing the system in four orthogonal directions and observing the resulting voltage unbalance. The system is then adjusted towards the state with the minimum observed unbalance, followed by further perturbations, observations, and adjustments until the system reaches and maintains a state of minimum unbalance. A control strategy is developed to implement the voltage unbalance mitigation method in the four-leg inverter, accompanied by a guide for modelling three-dimensional space vector modulation. Furthermore, optimisation techniques are employed to determine the optimal positioning of the inverters, aiming to minimize both total voltage unbalance and active power distribution loss. The

effectiveness of these methods has been validated through simulations conducted on several unbalanced radial distribution systems.

List of Publications

1. G. Das and D. Hazarika, *“Multi-objective Particle Swarm Optimization-Based Placement and Sizing of Distributed Generators Integrated to Unbalanced Low-Voltage Microgrids by Four-Leg Inverters”*, J. Inst. Eng. India Ser. B 104, 731–747 (2023), doi: 10.1007/s40031-023-00890-3.
2. G. Das and D. Hazarika, *“Perturb and Observe-Based Control of Four-Leg Grid-Feeding Inverters to Mitigate Voltage Imbalances in Low-Voltage Microgrids,”* J. Inst. Eng. India Ser. B 103, 1707–1717 (2022), doi: 10.1007/s40031-022-00734-6.

Table of contents

List of figures

List of tables

1

Introduction

1.1 Microgrid

A traditional electrical grid is a centralized electric power distribution system that serves a large geographical area, typically an entire country or region. Power is generated at large-scale power plants and transmitted over long distances to customers via a network of transmission and distribution systems. A *microgrid*, on the other hand, is a small, localized electric power distribution system that can operate independently or in tandem with a traditional grid. It serves a smaller geographical area, such as a neighbourhood, campus, island, industrial park, etc. and can include a variety of generation sources, such as renewable energy sources, storage systems, and traditional generators [**?**]. The primary distinction between the two is their size, autonomy, and the presence of Distributed Energy Resources (DER). Fig. 1.1 shows a typical microgrid and its components.

1.1.1 Grid-interactive hybrid microgrid

A *hybrid microgrid* is one that combines multiple sources of energy and energy storage technologies to provide reliable and sustainable electricity supply [**?**]. In a hybrid microgrid, various sources of energy generation can be integrated, such as solar panels, wind turbines, diesel or natural gas generators, and even micro-hydroelectric systems. Most of these energy sources are renewable and have different characteristics and availability patterns, allowing for a diverse and flexible energy mix. Apart from these

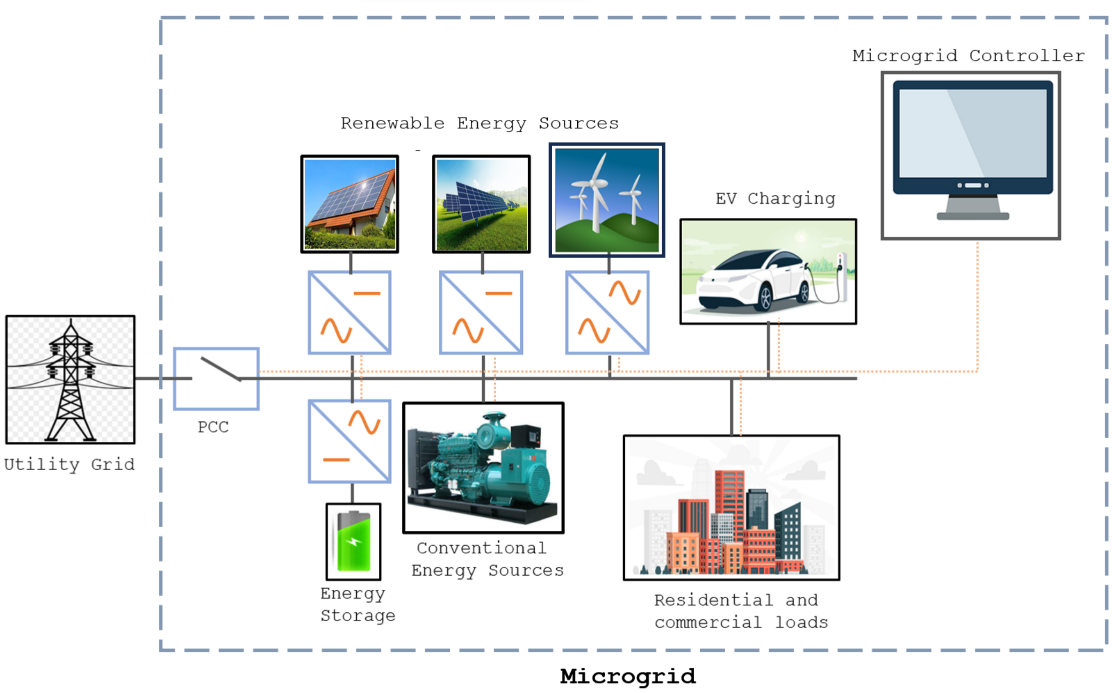

Fig. 1.1 A typical microgrid

energy generation sources, energy storage technologies, such as batteries, flywheels and compressed air systems are crucial components of hybrid microgrids. They store excess energy generated during times of low demand or high availability and release it during peak demand periods or when renewable energy sources are not actively generating electricity. Energy storage systems help ensure a stable and continuous power supply. Hybrid microgrids can also have both ac and dc distribution networks.

Grid-interactive hybrid microgrids are one that seamlessly interact with the main electrical grid while also incorporating various energy sources and storage systems for enhanced flexibility and resilience. The grid-interactive nature of these microgrids allows for bidirectional power flow, enabling them to both import and export electricity to and from the utility grid. This feature provides several advantages, such as the ability to sell excess power generated by the microgrid to the utility grid during periods of high production or to import power from the grid when the local generation is insufficient. The integration of renewable energy sources, such as solar and wind, in a grid-interactive hybrid microgrid promotes the utilization of clean and sustainable energy. During times of high renewable energy generation, surplus electricity can be fed into the grid, reducing dependence on conventional fossil fuel-based power generation. Furthermore, grid-interactive hybrid microgrids can enhance energy reliability and resilience by leveraging energy storage systems, which allow for the storage of excess energy during times of low demand or high generation, as well as when power from the main utility grid is available at lower rates. This stored energy can be later dispatched to the microgrid or the utility grid when needed, ensuring a consistent power supply even in the event of grid outages or fluctuations in renewable energy generation.

1.1.2 Basic components of a hybrid microgrid

The basic components of a hybrid microgrid are as follows:

- **Distributed Energy Resources:** DERs refer to a range of decentralized energy technologies, including generators, storage systems, and demand response programs. They provide localized energy generation, storage, and consumption capabilities, increasing grid flexibility, promoting renewable energy integration, and enhancing overall energy system resilience. DERs typically consist of various components that contribute to decentralized energy generation, storage, and management. Some common components of DERs include:
    - **Distributed Generators (DG):** These are the sources of energy within the microgrid that generate electricity. They can include various renewable energy sources such as solar panels, wind turbines, hydroelectric generators, and biomass systems. DGs can also include conventional generators like diesel or natural gas generators [**? ? ?**].
    - **Energy storage systems:** These systems store excess electricity generated by DGs for later use. Energy storage technologies commonly used in microgrids include batteries, flywheels, supercapacitors, and pumped hydro storage. They help balance the supply and demand of electricity, improve stability, and provide backup power during outages [**? ? ?**].
    - **Electric Vehicles (EV):** EVs can act both as load as well as source in a microgrid. EV batteries can serve as storage resources when connected to the grid, enabling vehicle-to-grid applications.
- **Power conversion systems:** Microgrids require power conversion systems to convert electricity from various sources and manage its distribution within the grid. These systems include inverters, rectifiers, and other power electronics converters that ensure compatibility with a wide range of sources and loads [**?**].
- **Microgrid controller:** The microgrid controller oversees the operation of the entire microgrid. It makes decisions based on real-time data and controls various components to optimize energy generation, storage, and consumption. The controller manages power flow, frequency control, and grid connection/disconnection. The microgrid controller utilizes control algorithms, sensors, and communication infrastructure to monitor and regulate the generation, storage, and consumption of electricity within the microgrid [**? ? ? ?**].
- **Grid interconnection:** Microgrids can be connected to the utility grid at the Point of Common Coupling (PCC), allowing them to import or export electricity as needed. Grid interconnection enables the sharing of resources, such as selling

excess electricity back to the grid or accessing additional power during high demand periods. It also provides a backup power source when the microgrid cannot meet its demand. There are, however, instances of off-grid microgrids in which the PCC is absent [?].

- **Loads and consumers:** Microgrids serve local loads and consumers within their geographical area. These can include residential, commercial, or industrial buildings and their associated electrical appliances, equipment, and machinery. EVs serve as a significant load due to their increased adoption, which has implications for grid management, charging infrastructure, and energy demand patterns. Loads are the devices that consume electricity within the microgrid, and consumers are the end-users who benefit from the electricity supply [?].

1.1.3 Modes of operation of a microgrid

A microgrid has the ability to run in either *islanded mode* or *grid-connected mode*. Grid-connected mode connects the microgrid to the main utility grid at PCC, whereas islanded mode disconnects the microgrid from the main utility grid.

Grid-connected mode:

The following are some important points about a microgrid's grid-connected mode of operation:

- **Power exchange with the utility grid:** In grid-connected mode, the microgrid can import or export power to and from the utility grid, depending on the overall demand and generation within the microgrid. During periods of high demand or when the microgrid's generation sources and energy storages are insufficient, the microgrid can draw power from the utility grid. Conversely, when the microgrid's generation exceeds local demand, excess power can be exported back to the utility grid [? ?].
- **Grid as a backup or supplement:** The utility grid serves as a backup or supplemental power source for the microgrid in grid-connected mode. If the microgrid's generation capacity is temporarily inadequate or if there is a system failure, the microgrid can rely on the utility grid for uninterrupted power supply. This ensures a continuous power supply to critical loads within the microgrid [? ?].
- **Grid frequency and voltage synchronization:** In grid-connected mode, the microgrid needs to maintain synchronization with the utility grid's frequency and voltage. This synchronization is crucial to facilitate seamless power transfer and to avoid any disruption or instability in the grid. Control mechanisms such as grid-support inverters, are employed to regulate the microgrid's output and maintain synchronization with the utility grid [? ?].

- **Grid stability and power quality:** When operating in grid-connected mode, the microgrid must adhere to power quality standards and contribute to grid stability. It needs to maintain the appropriate voltage and frequency levels within acceptable limits, ensuring a reliable and stable power supply to both the microgrid and the utility grid. Control strategies, such as droop control or power factor correction, can be implemented to support grid stability and enhance power quality [**?**].
- **Import/export tariffs and regulations:** The grid-connected mode involves adherence to utility regulations, import/export tariffs, and net metering policies. Depending on the specific regulatory framework and policies in place, the microgrid may receive financial incentives for exporting excess power to the utility grid or may be subject to tariffs when importing power. Compliance with these regulations is essential for ensuring a fair and transparent energy exchange between the microgrid and the utility grid [**? ?**].

Islanded mode:

The following are some important points about a microgrid's islanded mode of operation:

- **Energy self-sufficiency:** In islanded mode, the microgrid relies solely on its internal DERs to meet the local electricity demand. These DERs can include renewable energy sources like solar panels, wind turbines, biomass, or small-scale hydroelectric generators, energy storage systems such as batteries, supercapacitors, flywheels, etc. as well as conventional generation such as diesel and natural gas engine-based generators. The microgrid aims to achieve energy self-sufficiency by balancing its generation and load without drawing power from the utility grid [**? ?**].
- **Autonomous operation:** The islanded mode allows the microgrid to operate autonomously, independent of the utility grid. It is designed to handle its own power generation, distribution, and consumption within its boundaries. In this mode, the microgrid employs advanced control strategies and energy management systems to maintain a stable and reliable power supply to its local loads, even during fluctuations in demand or intermittent renewable energy generation [**? ?**].
- **Microgrid islanding detection and protection:** To transition into islanded mode, the microgrid must detect a grid disturbance or loss of connection from the utility grid. Microgrid islanding detection methods are employed to ensure that the microgrid operates independently only when it is safe to do so. Protection schemes, such as anti-islanding relays, are implemented to prevent power backflow into the utility grid and to ensure the safety of utility workers during grid maintenance or repairs [**? ?**].

- **Load shedding and prioritization:** In islanded mode, the microgrid may need to prioritize its loads and implement load shedding strategies during periods of high demand or limited generation capacity. Load shedding involves selectively shedding non-critical or lower-priority loads to maintain the balance between supply and demand within the microgrid. Advanced control algorithms are employed to determine load shedding priorities and optimize the utilization of available generation resources [**?**].

- **Reconnection to the utility grid:** While operating in islanded mode, the microgrid may reconnect to the utility grid when it becomes available again. This reconnection allows the microgrid to import or export power to and from the utility grid, facilitating the exchange of surplus energy or acquiring additional power if local generation is insufficient. Proper synchronization and protection mechanisms are implemented to ensure a seamless and safe transition during grid reconnection [**?**].

1.1.4 Advantages of hybrid microgrids

- **Increased resilience:** Microgrids provide enhanced resilience and reliability in energy supply. By operating as independent systems, they can continue to function even during disruptions in the utility grid. This makes microgrids particularly valuable in areas prone to natural disasters or grid failures, as they can ensure uninterrupted power supply to critical facilities such as hospitals, emergency services, and communication networks.

- **Localized power generation:** Microgrids enable localized power generation, allowing electricity to be produced closer to the point of consumption. This reduces transmission losses and enhances overall energy efficiency. Moreover, by incorporating renewable energy sources like solar or wind, microgrids contribute to reducing greenhouse gas emissions and promoting sustainable energy practises.

- **Integration of distributed energy resources:** Microgrids seamlessly integrate a variety of distributed energy resources, such as solar panels, wind turbines, and energy storage systems. This allows for optimized utilization of renewable energy sources, load balancing, and peak shaving. It also enables the effective integration of electric vehicles, further promoting sustainable transportation and grid flexibility.

- **Cost savings:** Microgrids can result in significant cost savings for end-users. By generating electricity locally, they reduce reliance on centralized power generation and associated transmission costs. Additionally, microgrids offer opportunities for energy trading and demand response programmes, enabling consumers to actively manage their energy consumption and potentially earn revenue through excess generation [**?**].

- **Grid support and energy independence:** Microgrids can provide ancillary services to the utility grid, such as voltage regulation, frequency control, and grid stabilization. In certain cases, they can operate autonomously, ensuring energy independence for communities or facilities. This independence reduces vulnerability to external factors and enhances overall energy security.

1.1.5 Microgrid control

There are two distinct approaches that can be distinguished in terms of the architecture of microgrid control: centralized and decentralized. A completely centralized control relies on extensive information transfer amongst involved units before a decision is reached at one location. Since microgrids involve a huge number of units, this will pose a significant implementation difficulty. On the other hand, in a fully decentralized control system, each unit is managed locally by a controller who is unaware of the circumstances of other units. A hierarchical control system with three levels of control—primary, secondary, and tertiary—can be used to reach a balance between those two schemes [**?** **?**].

Primary control

The primary control is the lowest and fastest level of control. It is responsible for stabilizing the microgrid's frequency and voltage, providing plug-and-play functionality to the DERs, appropriately sharing real and reactive power among the DERs and providing references for DERs' inner current and voltage controllers.

Secondary control

The secondary control is the intermediate level of control that operates in a centralized manner. It is slower than the primary control. It is responsible for providing the primary control set-point, restoring frequency as well as voltage deviations in the microgrid brought on by changes in the load or DER plug-and-play, and maintaining the necessary requirements for power quality.

Tertiary control

Tertiary control, the highest and slowest level of control, manages the power flow between the microgrid and the utility grid while taking into account financial considerations for the microgrid's optimal operation. This level involves creating a generator dispatch plan that maximizes financial savings by forecasting load, grid prices, and weather for the upcoming few hours or days.

1.2 Different operational issues of grid-interactive hybrid microgrids

A grid-interactive hybrid microgrid faces several operational challenges, and overcoming these challenges is critical for the microgrid's reliable and efficient operation. The following are the most important challenges:

- **Voltage unbalance:** In order to accommodate both single-phase and three-phase loads and sources microgrids are pre-dominantly four-wire distribution systems. Due to various reasons the voltages at the three-phase buses may become unbalanced, leading to significant operational issues. Voltage unbalance may lead to equipment malfunctions, reduced life span, increased energy losses, and reduced efficiency. Also, it may lead to failure of protection systems. It is therefore essential to address the issue of voltage unbalance to ensure the reliable and smooth operation of the microgrid [**? ? ? ?**].

- **System stability:** Microgrids often face challenges related to voltage regulation and stability. Fluctuations in load demand, intermittent generation from renewable energy sources, and inadequate control mechanisms can lead to voltage deviations, voltage drops, or voltage surges. These issues can impact the quality of the power supply and the performance of connected electrical devices. To overcome these challenges, microgrids require sophisticated control systems to manage the balance between power generation and consumption within the system. It is crucial to maintain stable voltage and frequency levels for the reliable operation of the microgrid. Effective control algorithms and communication systems are needed to balance power generation and consumption, regulate voltage and frequency, and prevent system instability or blackouts [**? ? ?**].

- **Modelling:** In conventional power systems, certain characteristics, such as three-phase balanced conditions, mostly inductive transmission networks, and constant-power loads, are predominant. However, these characteristics do not always apply to microgrids. Therefore, it is necessary to revise the existing models and adapt them to the unique characteristics of microgrids. Unlike bulk power networks with a large number of synchronous generators providing high inertia, microgrids exhibit low inertia characteristics. This behaviour becomes more prominent when a significant percentage of power electronic-interfaced distributed generation units are present. Without a suitable control strategy, the low inertia of the system may cause significant frequency variations, especially in stand-alone mode. In contrast, synchronous generators operating at the grid's frequency naturally dampen erratic frequency changes.

- **Intermittent renewable energy integration:** Microgrids often include intermittent renewable energy sources such as solar and wind power. The varying output of these sources can make maintaining a stable and reliable power supply difficult. Effective forecasting of renewable energy generation, in conjunction with advanced energy management systems, is thus required to optimise resource utilisation. By storing excess energy for use during periods of low renewable generation, energy storage systems can play a critical role in mitigating the impact of intermittency [**?** **?** **?** **?**].

- **Energy management and optimization:** Microgrids need to efficiently manage the balance between energy supply and demand. This involves optimizing the dispatch of power sources, including renewable energy generation, energy storage systems, and backup generators, to meet the varying load requirements. Effective energy management strategies, demand response mechanisms, and load forecasting techniques are crucial to ensure efficient utilization of available resources and minimize energy wastage. Advanced algorithms and real-time monitoring systems are required to optimize energy utilization, minimize energy wastage, and reduce operational costs. Demand response programs, which incentivize consumers to adjust their electricity usage during peak periods, can also contribute to effective energy management within the microgrid [**?** **?** **?**].

- **Placement of energy sources and storage:** The optimal placement of energy sources and storage is a critical issue in designing efficient and cost-effective microgrids. It involves determining the most suitable locations for installing these units within the existing infrastructure. The primary objective is to minimize power losses, improve voltage stability, and enhance overall system performance. Several factors need to be considered when determining the optimal placement of these energy sources and storage systems in a microgrid. These include load demand patterns, generation capacity, energy storage systems, and the desired objectives of the microgrid, such as minimizing power losses, improving energy self-sufficiency, or enhancing system resilience [**?** **?**].

- **Grid connection and islanding transitions:** Microgrids can operate in grid-connected mode or as an independent entity during islanding events when disconnected from the utility grid. The transition between these modes can present operational challenges. Smoothly transitioning from grid-connected to islanded operation and vice versa requires sophisticated control systems and protection mechanisms. During islanding events, the microgrid must maintain its stability, balance supply and demand, and ensure uninterrupted power supply to critical loads. When reconnecting to the utility grid, synchronization of frequency, voltage, and phase angle is essential to avoid grid disturbances. Inadequate control and protection mechanisms can result in grid synchronization issues and equipment damage [**?** **?** **?**].

- **Maintenance and fault management:** Microgrids comprise various components and equipment that require regular maintenance and effective fault management. Generators, inverters, energy storage systems, and control systems must be monitored, maintained, and repaired as needed to avoid unexpected failures and ensure reliable operation. Fault detection, localization, and timely fault resolution pose difficulties, particularly in complex microgrid architectures. Advanced fault detection and isolation techniques, combined with rapid restoration protocols, are critical for minimising downtime and maintaining continuous power supply within the microgrid. When DERs are present in the network at low voltage levels, reverse power flows can occur. These reverse power flows can complicate protection coordination and result in undesirable distribution of fault current, power flow patterns, and voltage control issues [**? ? ? ? ? ?**]

- **Cybersecurity and data protection:** As microgrids become more digitised and interconnected, cybersecurity becomes a critical concern. Protecting control systems, communication networks, and data from cyber threats is critical for preventing unauthorised access, system disruptions, and data breaches. To protect the microgrid infrastructure, strong cybersecurity measures such as firewalls, encryption protocols, and intrusion detection systems must be implemented. Regular security audits and employee training programmes can raise awareness and ensure adherence to cybersecurity best practises [**? ? ? ?**].

- **Regulatory and economical:** Microgrids are frequently confronted with regulatory and policy challenges that have an impact on their operation and development. Microgrid implementation and expansion are hampered by complex interconnection processes, uncertain regulatory frameworks, and conflicting standards. To encourage the growth and deployment of microgrids, simplified regulations, supportive policies, and clear guidelines are required. Aside from the critical technical issues of distribution system management, coordination of operation between microgrid and utility grid, and islanded operation, more needs to be done in terms of levelling the playing field, developing the market for aggregators, and cost reflective network pricing to recognise the costs and benefits of distributed generation to the networks [**? ? ? ? ?**].

1.3 Voltage unbalance in microgrids

Voltage unbalance refers to the uneven distribution of voltage magnitudes or phase angles across the phases of a three-phase power system. It occurs when there is a deviation from the ideal balanced conditions, where the voltages in all phases are equal in magnitude and have a 120-degree phase separation. In a low-voltage microgrid, maintaining a balanced voltage is crucial for the efficient and reliable operation of the system. However, there are instances when the voltage becomes unbalanced, leading to potential issues and challenges. Some of the important causes and effects of voltage unbalance in a microgrid are highlighted next.

1.3.1 Causes of voltage unbalance in microgrids:

- **Uneven distribution of single-phase loads:** Microgrids often have single-phase loads connected to the system, such as residential appliances or lighting systems. If these single-phase loads are not distributed evenly across the three phases, it can lead to voltage unbalance. For example, if a significant number of single-phase loads are connected to one phase while the other phases have relatively fewer loads, the voltage distribution becomes unbalanced [**?**].

- **Non-linear loads:** Non-linear loads are devices that draw non-sinusoidal current waveforms from the power supply, such as electronic equipment, variable speed drives, and certain types of lighting. These loads introduce harmonics and create imbalances in the current flowing through the system. When non-linear loads are connected to a three-phase system, they can cause uneven distribution of current among the phases. This unequal distribution of currents results in unbalanced voltages across the phases, leading to voltage unbalance [**? ? ?**].

- **Faulty equipment:** Faulty equipment or electrical components within the microgrid can introduce voltage unbalance. For instance, an open or short-circuited winding in a transformer or a faulty phase connection in a generator can result in unequal voltage distribution across the phases [**?**].

- **Grid disturbances:** Grid disturbances, such as voltage sags or swells, can cause voltage unbalance in microgrids. These disturbances can result from grid faults, rapid changes in load demand, or the operation of large industrial loads. When the grid experiences disturbances, the voltages in the microgrid can deviate from the balanced conditions, leading to voltage unbalance.

1.3.2 Effects of voltage unbalance in microgrids:

- **Increased equipment stress:** Voltage unbalance can have detrimental effects on the electrical equipment connected to the microgrid. Unbalanced voltages lead to unbalanced currents in the equipment, causing uneven heating and mechanical stress. This can accelerate equipment ageing, reduce its lifespan, and increase the likelihood of premature failures [**? ? ?**].

- **Reduced efficiency:** Voltage unbalance can negatively impact the efficiency of electrical devices and systems within the microgrid. Unbalanced voltages can lead to unbalanced currents in motors, resulting in increased losses, decreased power factor, and reduced energy efficiency. This inefficiency can lead to higher energy consumption and increased operational costs [**? ?**].

- **Equipment malfunctions:** Voltage unbalance can trigger equipment malfunctions, particularly in sensitive electronic devices. Unequal voltages can cause erratic behavior, malfunctioning, or even damage to electronic components, leading to disruptions in the microgrid's operation and reliability [**? ?**].

- **Poor power quality:** Voltage unbalance is a significant contributor to poor power quality. It can result in increased voltage fluctuations, harmonic distortion, and poor voltage regulation. These power quality issues can affect the performance of sensitive equipment, cause flickering lights, and introduce noise and interference in communication systems [?].
- **Unstable system operation:** Voltage unbalance can destabilize the operation of the microgrid. It can lead to voltage fluctuations, voltage drops, or voltage surges, which can disrupt the normal functioning of the connected devices and systems. Unstable voltage conditions can cause issues with control systems, protection relays, and overall system stability, affecting the reliability of the microgrid [?].

Unbalanced voltage in a microgrid can have adverse effects on the system's performance, energy efficiency, and equipment lifespan. Hence, it is important to identify the causes of voltage unbalance and take appropriate control measures to mitigate its effects.

1.4 Literature survey

Several works have been published on unbalanced voltage mitigation. Many researchers have proposed installing dedicated voltage correction devices, such as series and shunt active filters, in their work. Some of these methods involve measuring and supplying the negative sequence load current demand, whereas others involve injecting the negative sequence voltage. In [?], Barrero et al. utilized one parallel and one series active filter to address the issue. The parallel filter was used to eliminate the non-ideal component of the load current, while the series filter was used to reduce voltage perturbations by injecting negative sequence voltage. Graovac et al. suggested a power quality conditioning system in [?] that accounts for voltage imperfections by injecting negative sequence voltage. George et al. proposed injection of negative sequence current through a shunt active power filter for unbalanced voltage compensation in [?], while Singh et al. used a shunt active power filter for unbalanced voltage mitigation in [?]. Similarly, Chandra et al. proposed a shunt active filter for unbalanced voltage compensation in [?]. Wang et al. proposed a series-parallel compensator in [?], which utilizes negative sequence voltage and current injection. Lee et al. used a distributed static synchronous compensator to mitigate negative sequence voltage in [?]. Although these methods are effective for mitigating voltage unbalance issues, their overall utilisation is less as they are either unused or only lightly loaded when there are no voltage unbalance issues; additionally, this equipment increases the overall cost of the system.

Many distributed energy resources are integrated into the microgrid using power electronic converters. The controllers of these converters are typically designed to supply only positive sequence current to the microgrid. However, there are many converter topologies that can operate in an unbalanced mode and thus provide negative sequence current in addition to positive sequence current. Many researchers have taken advantage of this feature of these converters for unbalance voltage mitigation. In their paper [?], Hojo et al. proposed a method to first measure the load's negative sequence current demand and then supply it using the inverter. While this approach is simple, there are several significant challenges. For instance, the inverter hardware can only measure inverter current and voltage; load current measurement is not directly available to the inverter. As a result, additional external hardware is required to implement this method. The inverter hardware must also be modified to support the external measurements. Furthermore, because the inverter only supplies negative sequence current of the load connected to the same bus as the inverter, this method may not have a significant impact on overall voltage unbalance reduction, implying that the inverter's capability may be underutilised. In another method, presented in [?], the negative-sequence current to be injected into the microgrid by the inverter is estimated by measuring the negative-sequence voltage and negative-sequence line impedance angle at the point of connection of the inverter. This method is better than those that rely on measuring load current; however, because the negative sequence impedance angle is not constant, repeated measurements are required. The negative sequence impedance angle is calculated by injecting a known amount of negative sequence current and measuring the resulting negative sequence voltage at the inverter terminals. However, determining the negative sequence impedance angle and controlling the voltage unbalance by injecting a controlled amount of negative sequence injection cannot be done simultaneously, making this method difficult to implement. In [?], Savaghebi et al. used negative sequence reactive power as one of the inputs to the voltage control loop to compensate for unbalanced voltages. In [?], Wang et al. proposed mitigating negative sequence voltage by absorbing negative sequence current from the grid. This approach is not very effective as the negative sequence current absorbed by the converter is small, and hence the correction obtained is not significant. In [?], Tianyi et al. suggested injecting negative sequence current by adding an adjustable virtual negative sequence impedance into the controller.

In some reported works, coordinated operation of DERs using communication among them is used for unbalance voltage correction. In [?], Nejabatkhah et al. proposed a method for compensating unbalanced voltage by controlling DER's negative sequence current to be in-phase with the grid negative sequence current. Similarly, in [?], negative sequence current is shared among the DERs to achieve unbalanced voltage compensation. Meng et al. in [?] and Savaghebiin et al. in [?] used DERs as compensators and employed hierarchical control methods for optimal unbalanced voltage compensation. In [?], DERs are also used as compensators, with the negative sequence voltage of the DERs controlled through tertiary control to reduce voltage unbalance at critical buses. Coordinated operation of DERs through a communication channel is a feasible solution, but has the inherent risk of communication failure.

In [?], asymmetric operation of single-phase loads and sources is used to reduce unbalanced voltage. Kadam et al. in [?] proposed assigning DERs to heavily loaded phases to reduce voltage unbalance. Injecting more power into the heavily loaded phase and shifting transferable loads to the lightly loaded phase is suggested by Weckx et al. in [?] and [?]. These approaches require complex converter topologies and switching algorithms. Additionally, shifting sources and loads between phases can compromise the quality of power supply. Asymmetric operation of battery energy storage is proposed in [?]. Methods involving the network operator directly controlling appliances in households or motivating end-users to shift their consumption through price changes have also been shown to impact the voltage unbalance in [?].

The literature survey reveals various methods for mitigating unbalanced voltage in microgrids. Existing approaches, such as dedicated voltage correction devices and coordinated operation of distributed energy resources, have demonstrated effectiveness but come with limitations including additional equipment, increased costs, and the risk of communication failures. Moreover, methods involving asymmetric operation and load shifting require complex topologies and can compromise power supply quality. An alternative approach involves leveraging the capabilities of power electronic converters used in distributed energy resources. Some converter topologies can operate in an unbalanced mode, providing negative sequence current in addition to positive sequence current. Researchers have explored utilizing this feature for voltage unbalance mitigation. However, these methods face challenges such as the need for external hardware, modifications to the inverter, and the difficulty of simultaneous estimation of required network parameters and control of negative sequence current injection. These limitations highlight the need for alternative methods that are more efficient, practical, and cost-effective, ensuring reliable voltage balance in microgrid systems. By exploring the capabilities of converters to provide negative sequence current in addition to positive sequence current, more efficient and practical solutions for voltage unbalance mitigation can be developed.

The placement of DERs in a hybrid microgrid has a significant impact on various network indices and power quality. Sub-optimal installation of these devices can lead to insignificant improvements in network parameters, such as distribution losses and voltage unbalance. Therefore, it is crucial to determine the ideal capacity and placement of these devices. The optimal placement and sizing of DERs and compensation devices in both balanced and unbalanced microgrids has been extensively researched; however, work on the placement of distributed generators (DGs) in unbalanced systems is significantly less than in balanced systems. In some of the reported works analytical methods are used to determine the ideal location and size of DGs. In these methods, network equations are formed and solved iteratively for each bus. Bhimarasetti et al. developed loss-saving equations in [?]. For each bus in a 25-bus Unbalanced Radial Distribution System (URDS), they computed the amount of current that must be delivered to achieve the greatest loss-saving. Then, for each bus, the matching DER size was calculated, and the bus with the greatest loss savings was chosen for DER placement. Ponnam et al. used sensitivity analysis in [?] to find the best size and position of DER in the 25-bus URDS for minimizing system real power loss. Oladeji utilized nodal hosting capacity and critical voltage indices to place multiple DERs in the URDS in [?]. Rekha et al. used deviations in voltage profile index and stability in [?] to minimize power loss by optimally placing DERs in the URDS. Analytical methods have the disadvantage that, as the number of unknown variables and distribution buses increases, so does the complexity and time required to solve the problems.

Meta-heuristics algorithms, due to their ability to solve multi-dimensional optimisation problems and their ease of implementation, are widely used for determining the optimal placement and sizing of different types of DGs. The main objectives considered in most of the reported works are the minimization of distribution power loss and the improvement of the voltage profile. For instance, Swain et al. [?] used an Exhaustive search technique to place solar DGs in URDS with the goal of minimising real power loss. Routray et al. [?] employed Black widow optimization to achieve optimal placement and sizing of DGs in URDS with the objective of minimizing loss. Improved particle swarm optimization was utilized by Werkie et al. [?] for the placement of multiple DGs in Radial Distribution systems (RDS) with the goal of reducing power losses and improving voltage profile. In [?], Fathy et al. used the Artificial humming bird algorithm to determine the placement of biomass DGs in RDS. Similarly, Khan et al. [?] used the Honey badger algorithm to size and place different types of DGs in RDS. Balu et al. [?] employed the weighting factor-based student psychology algorithm with a weighted-factor based multi-objective function to solve the problem of sizing and placement of DGs in RDS. Eid et al. [?] utilized the Improved marine predators algorithm to optimize the placement and active power of DGs and the sizing of shunt capacitors for optimal reactive power. Modified symbiotic organisms search algorithm was used by Saha et al. [?] to optimally size and place wind, solar and biomass-based DGs in RDS. Ogunsina et al. [?] used Ant colony optimization for DG sizing and placement with the objective of minimizing loss. Nguyen et al. [?] used Enhanced sunflower optimization to determine the optimal sizing and placement of DGs with the goal of minimizing loss. In [?], Eid et al. employed Enhanced artificial ecosystem-based optimization for the placement of multiple DGs in RDS with the objective of minimizing total voltage deviation, maximizing system stability, and reducing total power losses. Prommee et al. [?] used Improved reinitialized social structures particle swarm optimization with the goal of minimizing loss for DG sizing and placement in RDS. Naderipour et al. [?] used the Spotted hyena optimizer, while Particle swarm optimization was utilized by Tooryan et al. [?] and Ghanbari et al. [?]. Simulated annealing was used by Mitra et al. [?] for the sizing and placement of DGs.

In some studies, a combination of analytical methods and meta-heuristic algorithms has been utilized. For instance, Das et al. [?] used sensitivity analysis to identify the optimal location of shunt capacitors and DGs and employed a genetic algorithm to determine their sizes. The main objectives considered were minimizing the annual energy loss and improving the voltage profile. Similarly, in [?], the optimal placement of DGs in an URDS was determined using a modified sensitivity factor method, while the optimal size was found using the Adaptive Particle Swarm Optimization technique.

In some of the reported works, multiple objectives are considered for sizing and placing the DGs. In their study [?], Arulprakasam et al. utilized a rainfall optimization-based technique to solve the multi-objective problem of DG placement and network reconfiguration. Another study on the same problem was conducted by Haider et al. [?]. Purlu et al. [?] used a combined genetic and particle swarm optimization algorithm to determine the rating and location of DGs with the aim of minimizing annual energy loss and reducing voltage deviation. Ramadan et al. [?] used a multi-objective artificial gorilla troop optimization method to identify the optimal position and size of renewable DGs while minimizing net emissions, voltage deviations, and voltage stability. Anbuchandran et al. [?] employed a firefly algorithm for the sizing and installation of DGs. They formulated the objective function by considering distribution loss reduction, voltage profile and stability improvement, pollutant emission reduction, and harmonic distortion elimination. Janamala et al. [?] used an Archimedes optimization-based algorithm to determine the positioning and sizing of a solar photovoltaic system with the goal of minimizing grid dependence and reducing greenhouse gas emissions. Raut et al. [?] used a sine-cosine-based algorithm for sizing and siting of DGs, aiming to reduce annual energy loss, voltage stability index, and pollutant gas emissions. Tan et al. [?] proposed an objective function that considers integrated power losses, voltage profile, and pollution emissions, using the swarm moth flame optimization algorithm (SMFO). Additionally, other methods such as the genetic algorithm [?], artificial bee colony algorithm [?], non-dominated sorting genetic algorithm, and fuzzy method in [?] have been used for solving the problem of sitting and sizing.

The placement DERs in microgrids plays a crucial role in optimizing network performance and power quality. While extensive research has been conducted on optimal placement and sizing of DERs in balanced microgrids, studies focusing on unbalanced systems are limited. Analytical methods have been used to determine optimal locations and sizes of DERs in unbalanced systems, but their complexity increases with the number of variables and buses. To overcome this, meta-heuristic algorithms have gained popularity due to their ability to solve multi-dimensional optimization problems effectively. These algorithms, such as Exhaustive search, Black widow optimization, improved particle swarm optimization, and others, aim to minimize power losses and improve voltage profiles. Additionally, a combination of analytical methods and meta-heuristic algorithms has been employed in some studies. However, there is a research gap in exploring the combined study of DER placement and the impact of converter placement on overall voltage unbalance. Further investigation is needed to address this gap and enhance the understanding of DER placement in unbalanced microgrids.

Objectives of the work Voltage unbalance is a significant issue in low voltage microgrids, particularly at the distribution buses. However, this problem can be reduced by using suitable converters that ensure the microgrid's reliability and stability. The main objectives of the work can be summarized as follows:

- To investigate the effect of negative sequence current injection on voltage unbalance of low-voltage microgrids.
- To develop a technique for mitigating voltage unbalances in low-voltage microgrids by utilising the unbalanced operation of inverters interfacing distributed generators while requiring minimal changes to existing hardware.
- To design a suitable controller for implementing the developed unbalanced voltage compensation method in four-leg inverters.
- To determine the optimal size and location of the Four-Leg Inverter-interfaced distributed Generators (FLIG) that will achieve the least voltage unbalance and the least active power distribution loss.

Main contributions of the work The main contributions of the work are as follows:

- Development of a novel control strategy for four-leg inverter-interfaced distributed generators to reduce voltage unbalances in low-voltage microgrids. The method involves injecting a controlled amount of negative sequence current into the microgrid at the point of inverter connection. The negative sequence current reference is determined using the proposed method, which has the major advantage of only requiring voltage and current measurements at the inverter terminal for implementation. As these measurements are already available in an inverter control circuit, no hardware modification is necessary to implement the proposed method.
- Design of controller for the FLIGs capable of injecting the required real and reactive power as well as implementing the proposed unbalance voltage correction method. The reference current for the current controller is generated by adding positive sequence reference current and negative sequence reference current. The real power and reactive power injection is controlled by the positive sequence current injection, and unbalance voltage correction is controlled by negative sequence current injection.
- Development of algorithms based on particle swarm optimization and grey wolf optimization for determining the optimal size and location of FLIGs in radial microgrids. The objective function is formulated as a multi-objective function with the first objective being to minimize active power distribution loss and the second objective being to minimize total voltage unbalance across all buses in the microgrid.
- Development of a step-by-step procedure for modelling and simulating three-dimensional space vector modulation using MATLAB/Simulink in natural coordinate and $\alpha\beta\gamma$ coordinate. The model is useful for power system studies involving control of four-leg inverters with three-dimensional space vector modulation, and is used in this work to generate gate pulses for the four-leg inverter.

The organization of the thesis

- Chapter 1: This chapter provides a brief introduction to hybrid microgrids and their operational challenges, with a focus on the problem of voltage unbalance. It includes a literature review of methods for correcting unbalanced voltages and optimal sizing and placement of DERs.

- Chapter 2: In this chapter, the significance of negative sequence current in addressing voltage unbalance is elucidated, alongside an overview of converters suitable for this task. A detailed discussion on creating a MATLAB/Simulink model for the three-dimensional space vector modulation of four-leg inverters is provided. Furthermore, the effect of negative sequence current injection using four-leg inverters on unbalance voltage correction is demonstrated.

- Chapter 3: This chapter presents a novel perturb and observe-based control strategy for four-leg inverter-interfaced distributed generators to reduce voltage unbalances in low-voltage microgrids. The effectiveness of this approach is verified through extensive testing on various unbalanced radial distribution systems. Additionally, a closed-loop control strategy is presented for the implementation of the voltage mitigation method.

- Chapter 4: In this chapter, a multi-objective particle swarm optimization-based method and a grey wolf optimization-based method are proposed for determining the ideal position and rating of four-leg inverter-interfaced distributed generators. The optimization has two objectives: to determine the positions and ratings of DG units for which the real power distribution loss is minimum, and to determine the locations at which the total voltage unbalances in the microgrid are at their lowest after applying unbalance voltage correction. The optimization is obtained using a weighted factor-based approach and a Pareto-based approach.

- Chapter 5: This chapter provides a brief summary of the research work done and discusses the future scope of the work.

2

Unbalanced voltage mitigation in low-voltage microgrids using four-leg inverters

A low-voltage microgrid comprises single-phase and three-phase loads and sources, as well as non-linear loads. The presence of single-phase loads and sources necessitates a four-wire distribution system configuration. Because it is not always possible to distribute the single-phase loads and sources equally among the three phases, unbalanced currents flow through the lines, causing unequal voltage drops in the line impedance and hence voltage unbalance in the distribution buses. Non-linear loads, faulty equipment, and grid faults are also contributing factors to voltage unbalance. Voltage unbalance can cause a variety of issues, including reduced equipment lifespan, increased energy consumption, and decreased system efficiency. Therefore, it is important to measure and monitor voltage unbalance and adopt additional controls for unbalanced voltage mitigation.

In this chapter, the significance of negative sequence current in addressing voltage unbalance is investigated. Converters suitable for this task are investigated, and the four-leg inverter topology for unbalance voltage correction is put forward. A comprehensive guide on developing a MATLAB/Simulink model of three-dimensional space vector modulation for the four-leg inverter in *abc* and $\alpha\beta\gamma$ coordinates is presented. The guide includes step-by-step instructions and thorough explanations of the required theory for implementing the algorithms. Furthermore, the effect of negative sequence current injection on unbalance voltage using four-leg inverter is also demonstrated.

2.1 Significance of negative sequence current in unbalance voltage mitigation

According to the theory of symmetrical components, an unbalanced system of phasors can be resolved into positive sequence, negative sequence, and zero sequence components [?]. As a result, the unbalanced voltage and current at the distribution buses can be resolved into positive, negative, and zero sequence voltages and currents by eqns. (2.1) and (2.2).

$$\begin{bmatrix} V_a^+ \\ V_a^- \\ V_a^0 \end{bmatrix} = \frac{1}{3} \begin{bmatrix} 1 & 1 & 1 \\ 1 & a & a^2 \\ 1 & a^2 & a \end{bmatrix} \begin{bmatrix} V_a \\ V_b \\ V_c \end{bmatrix} \tag{2.1}$$

$$\begin{bmatrix} I_a^+ \\ I_a^- \\ I_a^0 \end{bmatrix} = \frac{1}{3} \begin{bmatrix} 1 & 1 & 1 \\ 1 & a & a^2 \\ 1 & a^2 & a \end{bmatrix} \begin{bmatrix} I_a \\ I_b \\ I_c \end{bmatrix} \tag{2.2}$$

Where $a = e^{j2\pi/3}$. The superscript '+', '-' and '0' are used to represent positive, negative, and zero sequence components, respectively.

Several types of DER in a microgrid connect to distribution lines via power electronic converters. Most of these converters' topologies allow only positive-sequence current injection into the grid. As a result, the negative and zero sequence current demands at the distribution buses are met by either the utility grid or the microgrid's synchronous generators. However, with suitable converters, the DERs can share the negative sequence and zero sequence current demands at the distribution buses, reducing system voltage unbalance [?]. The role that converters can play in unbalanced voltage mitigation can be understood using the following example.

Fig. 2.1 illustrates a grid-connected microgrid with converter-interfaced DER and unbalanced loads. The microgrid is connected to the utility grid at the PCC. The microgrid can be represented by an equivalent Thevenin's circuit in which all of the elements on the left side of 'A' are represented by a voltage source, V_{grid}, and an equivalent line impedance, Z_L. A constant current source, I_L, represents the loads on the right side of 'A', and a controlled current source, I_C, represents the converter at 'A'. When the load at 'A' is unbalanced, I_L has positive, negative, and zero sequence current components.

As shown in Fig. 2.2, when the converter at 'A' is disconnected, all sequence currents flow through V_{grid} and Z_L. This results in positive, negative, and zero sequence voltage drops across Z_L, causing an unbalanced voltage at 'A'.

Fig. 2.3 illustrates that if the converter at 'A' and V_{grid} share the positive sequence current required by the load, the positive sequence voltage drop across Z_L reduces.

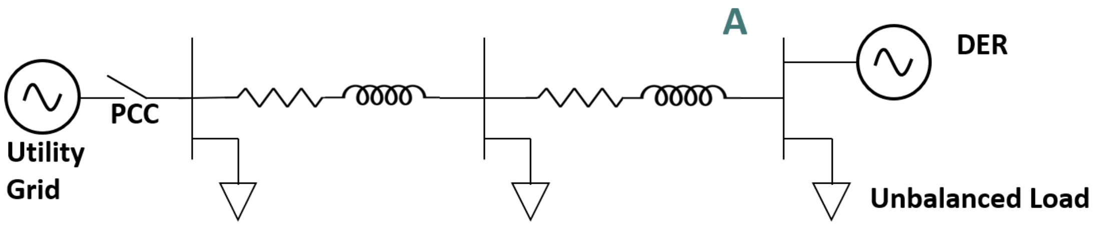

Fig. 2.1 Single line diagram of a microgrid

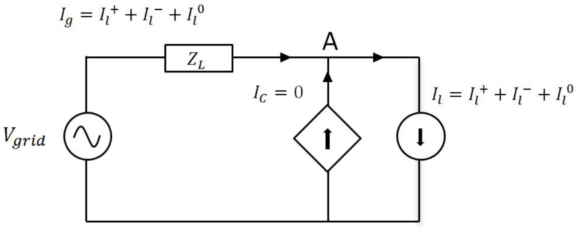

Fig. 2.2 Equivalent circuit of a microgrid with converter disabled

However, the negative and zero sequence currents still flow through V_{grid} and Z_L, causing the voltage unbalance at ‘A’ to persist.

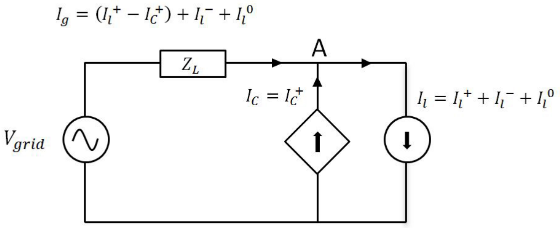

Fig. 2.3 Equivalent circuit of a microgrid with converter supplying only positive sequence current

If the converter at ‘A’, in addition to sharing the positive sequence current, also shares the load’s negative and zero sequence current requirements, the voltage drop across Z_L due to negative and zero sequence currents will decrease, reducing the voltage unbalance at ‘A’. This is illustrated in Fig. 2.4.

The equivalent circuit diagram for positive sequence components is shown in Fig. 2.5, and the equivalent circuit diagram for negative sequence components is shown in Fig. 2.6. A similar circuit can be drawn for the zero sequence.

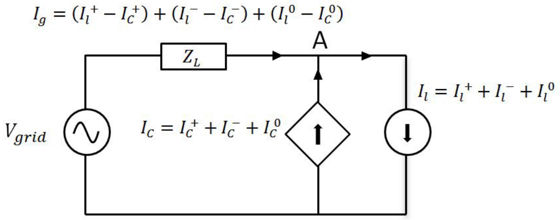

Fig. 2.4 Equivalent circuit of a microgrid with converter supplying positive, negative, and zero sequence currents

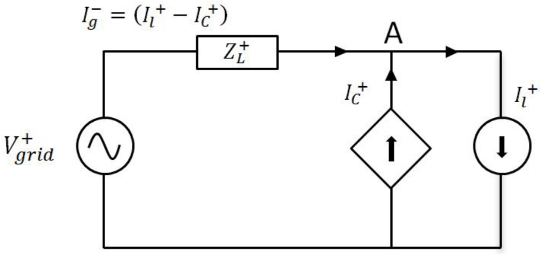

Fig. 2.5 Positive sequence equivalent circuit

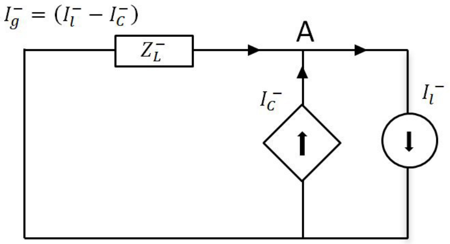

Fig. 2.6 Negative sequence equivalent circuit

Thus, from Fig. 2.6,

$$I_l^- = I_g^- + I_c^- \tag{2.3}$$

$$\implies I_g^- = I_l^- - I_c^- \tag{2.4}$$

$$V_A^- = I_g^- Z_L^- \tag{2.5}$$

From eqn. (2.4), it is evident that when the magnitude and phase of the negative sequence converter current I_c^- is equal to that of the negative sequence load current I_l^-, I_g^- becomes zero, causing the negative sequence voltage V_A^- to also become zero. However, for any other value of I_c^-, I_g^- can either decrease, resulting in a reduction of voltage unbalance, or increase, leading to an increase in voltage unbalance. Fig. 2.7a illustrates the phasor diagram when the converter does not supply negative sequence current, resulting in $I_g^- = I_l^-$. On the other hand, Fig. 2.7b displays the phasor diagram when the converter supplies negative sequence current at a magnitude and phase such that I_g^- decreases. Similarly, Fig. 2.7c shows the phasor diagram when the converter supplies negative sequence current with a magnitude and phase such that I_g^- increases. In both cases, the impact on negative sequence voltage at ‘A’ is depicted. Furthermore, Fig. 2.7d demonstrates the phasor diagram when the converter supplies negative sequence current at a magnitude and phase such that $I_c^- = I_l^-$. In this scenario, the negative sequence voltage at ‘A’ will be zero.

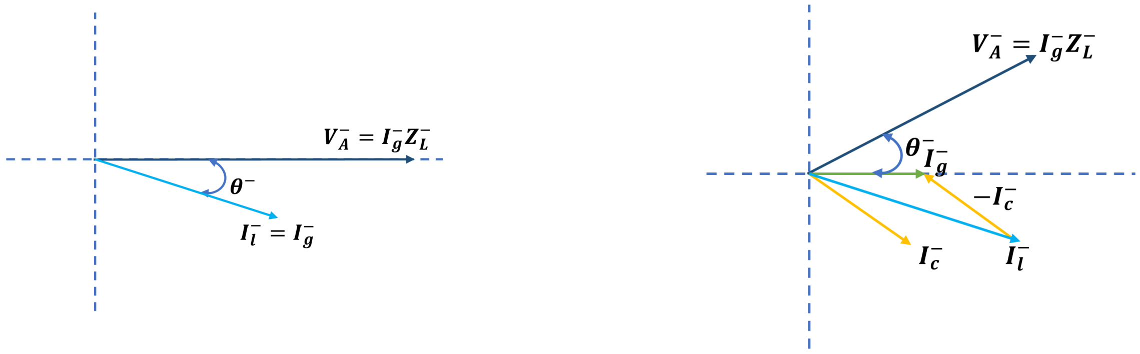

(a) Phasor diagram for the case when $I_g^- = I_l^-$

(b) Phasor diagram for the case when I_g^- decreases

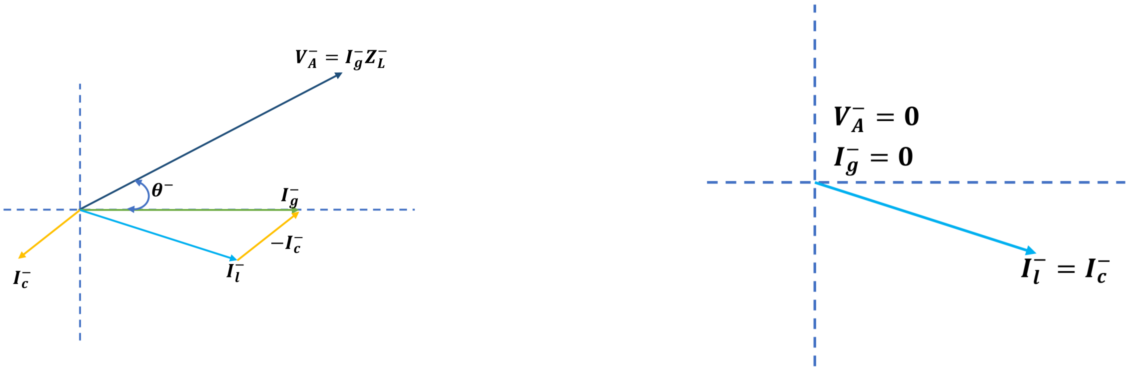

(c) Phasor diagram for the case when I_g^- increases

(d) Phasor diagram for the case when $I_g^- = 0$

Fig. 2.7 Phasor diagrams for different values converter negative sequence current

Therefore, if the converters that interface the DERs to the microgrid have the capability of operating in an unbalanced manner and participate in mitigating unbalanced voltage, the voltage unbalance problem in a low-voltage microgrid can be significantly reduced.

2.1.1 Converters suitable for unbalanced current injection

As discussed previously, the injection of negative and zero sequence currents by the converters is necessary to mitigate voltage unbalance in the microgrid. However, this requirement can only be met if the three phases are controlled independently. The most commonly used converter topology for balanced current injection is the three-leg three-wire topology, as shown in Fig. 2.8. However, this topology does not have a neutral connection point, and as a result, the three phases cannot be controlled independently. Therefore, this basic three-phase converter topology is not suitable for unbalanced voltage mitigation. Some of the converter topologies suitable for low-voltage microgrids, that can provide independent control of the three phases are presented below.

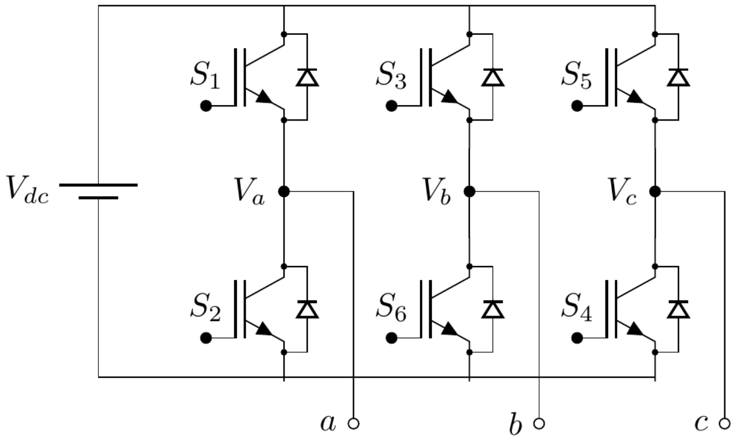

Fig. 2.8 Schematic of a three-phase three-wire converter

Three-leg converters with split capacitors

One topology that can provide independent control of the three phases is the three-leg converter with a split DC link capacitor [? ?]. This topology provides a neutral point for connecting the neutral wire and allows for independent control of the three phases. However, in order to achieve equal voltage sharing between the split capacitors, expensive and large capacitors are required. Furthermore, capacitor voltage balancing can be a challenge with this topology. Fig. 2.9 depicts a three-leg four wire converter that uses this topology.

Neutral-point clamped converters

The three-level neutral point clamped configuration is a widely used topology for medium and high voltage applications, especially in motor drive systems. This is because it has a low dv/dt, a low total harmonic distortion (THD), and can handle high voltage demands [?]. While this converter can also be used in lower power

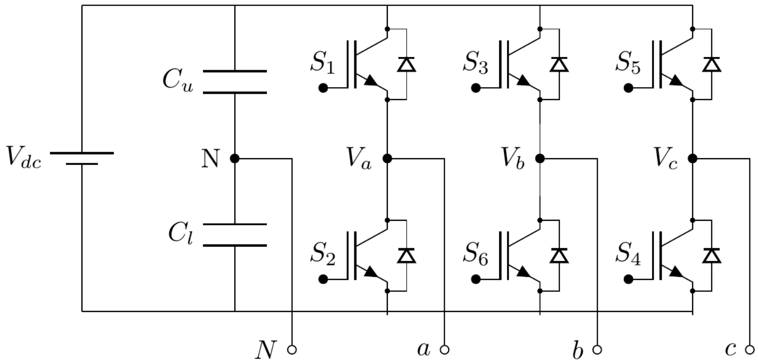

Fig. 2.9 Schematic of a three-phase three-leg split capacitor converter

applications, it is not commonly used in low voltage systems due to the high number of power electronic switches and complex control circuitry required. Fig. 2.10 shows a neutral point clamped converter.

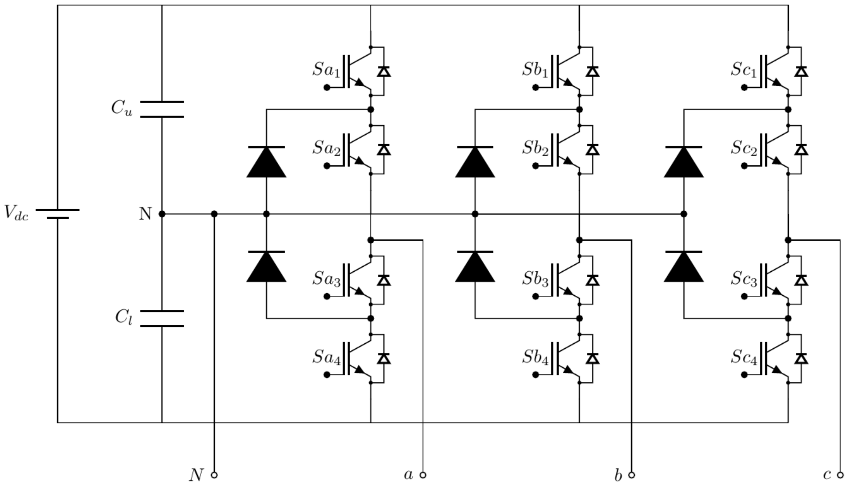

Fig. 2.10 Schematic of a three-phase neutral point clamped converter

Three-phase four-leg converters

The four-leg converter topology shown in Fig. 2.11 is increasingly finding its way into applications such as distributed generators [? ?], active power filters [? ? ?], three-phase PWM rectifiers [? ?], and common mode noise reduction [?] etc. They are also employed in industrial applications, such as motor drives, to deliver efficient and precise power output control. It consists of four legs, with three legs dedicated to phase connection and the fourth leg used for neutral connection. Each of the three phases can be controlled independently, enabling the converter to adjust the voltage and current for each phase individually. This makes it well-suited for use in microgrids that suffer from voltage unbalances. When compared to other three-phase four-wire converters, the three-phase four-leg converter is often more cost-effective, simpler in control, making it a suitable choice for low-voltage microgrids [? ?]. Additionally, the problems associated with split capacitors are also absent in this converter. Because of all of these benefits, the three-phase four-leg converter is chosen for unbalance voltage correction in this work.

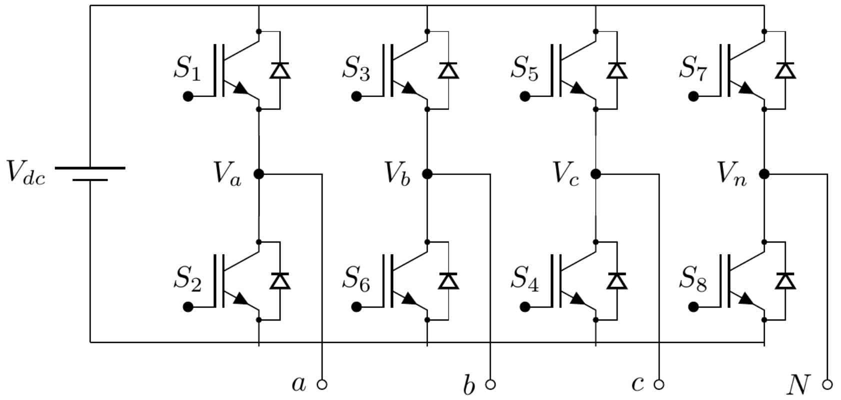

Fig. 2.11 Schematic of a three-phase four-leg converter.

Control of the four-leg converter for unbalanced operation involves operating the eight-switches as per the desired output. Many techniques have been developed for the generation of gate pulses for the four-leg converter, such as sinusoidal pulse width modulation (SPWM)[?], three-dimensional space vector modulation (3-D SVM), selective harmonic elimination [?], hysteresis control [?], sliding mode control [?], and model predictive control [?], among others. However, the most widely used control schemes for this converter are the sinusoidal pulse width modulation and the three-dimensional space vector modulation techniques. The 3-D SVM is preferred over the SPWM due to its ability to utilize a higher DC bus voltage, reduce overall harmonic distortion, and minimize switching and conduction losses [?]. Since the phase voltages in a four-leg converter are independent of each other, the use of 3-D SVM is necessary for this configuration [? ?]. The space vectors in 3-D SVM can be represented in either *abc* i.e. natural coordinates or $\alpha\beta\gamma$ coordinates [? ? ?].

2.2 Control of four-leg inverters using 3-D SVM

In the four-leg converter, each leg has an upper switch and a lower switch, and only one switch in each leg is allowed to be switched on at a time. Therefore, there are only 16 possible switching combinations available for its control. Depending on the state of the switches, the instantaneous AC output terminal voltages v_{aN}, v_{bN}, and

v_{cN} can be either 0, V_{dc}, or $-V_{dc}$, where V_{dc} is the DC link voltage. In the space vector modulation technique, each switching state of the converter corresponds to a switching space vector. Thus, the 16 possible switching combinations each represent a corresponding switching space vector. The methods are designed to select switching vectors that, when applied sequentially for a predetermined amount of time during the switching period, produce an average voltage equal to the required reference voltage. Two of these switching vectors are zero vectors, while the remaining 14 are non-zero vectors. Table. 2.1 displays the switching states along with their corresponding terminal voltages and switching vectors.

Table 2.1 Switching states with the associated terminal voltages and switching vectors.

State	Vector	S_a	S_b	S_c	S_N	v_{aN}	v_{bN}	v_{cN}
1	V_1	0	0	0	0	0	0	0
2	V_2	0	0	1	0	0	0	V_{dc}
3	V_3	0	1	0	0	0	V_{dc}	0
4	V_4	0	1	1	0	0	V_{dc}	V_{dc}
5	V_5	1	0	0	0	V_{dc}	0	0
6	V_6	1	0	1	0	V_{dc}	0	V_{dc}
7	V_7	1	1	0	0	V_{dc}	V_{dc}	0
8	V_8	1	1	1	0	V_{dc}	V_{dc}	V_{dc}
9	V_9	0	0	0	1	V_{dc}	0	$-V_{dc}$
10	V_{10}	0	0	1	1	$-V_{dc}$	0	0
11	V_{11}	0	1	0	1	$-V_{dc}$	$-V_{dc}$	$-V_{dc}$
12	V_{12}	0	1	1	1	$-V_{dc}$	V_{dc}	0
13	V_{13}	1	0	0	1	0	0	$-V_{dc}$
14	V_{14}	1	0	1	1	0	0	0
15	V_{15}	1	1	0	1	0	V_{dc}	$-V_{dc}$
16	V_{16}	1	1	1	1	0	0	0

2.2.1 3-D SVM in *abc* coordinates

The 3-D SVM technique described in [**?**], utilizing *abc* coordinates, is applied in this study. The phase voltages v_{aN}, v_{bN}, and v_{cN} is selected as the reference frame. When viewed in three-dimensional space, the sixteen switching vectors can be found at the vertices of two interconnected cubes. Joining the corresponding vertices of the cubes forms a dodecahedron, as illustrated in Fig. 2.12. The dodecahedron consists of 24 tetrahedrons, each comprising three non-zero switching vectors and the zero vectors. The synthesis of the reference voltage vector is discussed next.

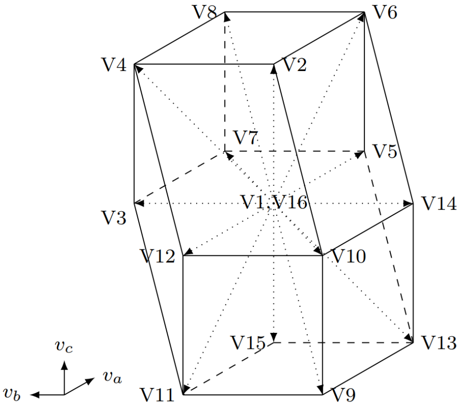

Fig. 2.12 Dodecahedron containing the switching vectors in *abc* coordinates

Selection of the switching vectors:

The non-zero switching vectors are selected by identifying the tetrahedron that contains the reference voltage vector. The selection process involves the following steps:

Step 1: First, six indices are calculated using eqn. (2.6).

$$\left.\begin{aligned}
C_1 &= Sign\left(INT\left(\frac{V_{aref}}{V_{dc}}+1\right)\right)\\
C_2 &= Sign\left(INT\left(\frac{V_{bref}}{V_{dc}}+1\right)\right)\\
C_3 &= Sign\left(INT\left(\frac{V_{cref}}{V_{dc}}+1\right)\right)\\
C_4 &= Sign\left(INT\left(\frac{V_{aref}}{V_{dc}}-\frac{V_{bref}}{V_{dc}}+1\right)\right)\\
C_5 &= Sign\left(INT\left(\frac{V_{bref}}{V_{dc}}-\frac{V_{cref}}{V_{dc}}+1\right)\right)\\
C_6 &= Sign\left(INT\left(\frac{V_{aref}}{V_{dc}}-\frac{V_{cref}}{V_{dc}}+1\right)\right)
\end{aligned}\right\} \tag{2.6}$$

Where, $v_{aref}, v_{bref}, v_{cref}$ are the instantaneous values of the reference voltage to be generated. The functions $INT(x)$ extract the integer portions of x and $Sign(x)$ extract the sign of x using eqn. (2.7).

$$Sign(x) = \begin{cases} 1, & x > 0 \\ -1, & x < 0 \\ 0, & x = 0 \end{cases} \tag{2.7}$$

Step 2: Next, a region pointer (RP) is determined by using eqn. (2.8).

$$RP = 1 + C_1 + 2C_2 + 4C_3 + 8C_4 + 16C_5 + 32C_6 \tag{2.8}$$

The value of RP can be anywhere between 1 and 64. However, only twenty-four of them match the twenty-four tetrahedrons.

Step 3: From the RP calculated, the three non-zero switching vectors (V_{d1}, V_{d2}, V_{d3}) are identified using Table. 2.2

Table 2.2 RP and the corresponding switching vectors.

RP	(V_{d1}, V_{d2}, V_{d3})	RP	(V_{d1}, V_{d2}, V_{d3})
1	V_{12}, V_{10}, V_9	41	V_{14}, V_{13}, V_9
5	V_{12}, V_{10}, V_2	42	V_{14}, V_{13}, V_5
7	V_{12}, V_4, V_2	46	V_{14}, V_6, V_5
8	V_8, V_4, V_2	48	V_8, V_6, V_5
9	V_{14}, V_{10}, V_9	49	V_{15}, V_{11}, V_9
13	V_{14}, V_{10}, V_2	51	V_{15}, V_{11}, V_3
14	V_{14}, V_6, V_2	52	V_{15}, V_7, V_3
16	V_8, V_6, V_2	56	V_8, V_7, V_3
17	V_{12}, V_{11}, V_9	57	V_{15}, V_{13}, V_9
19	V_{12}, V_{11}, V_3	58	V_{15}, V_{13}, V_5
23	V_{12}, V_4, V_3	60	V_{15}, V_7, V_5
24	V_8, V_4, V_3	64	V_8, V_7, V_5

Calculation of duty cycles and switching duration:

Step 1: In order to determine the duty cycles, d_i, for each non-zero switching vector, the converter's average large signal model is employed, as stated in eqn. (2.9).

$$\mathbf{v}_{ref} = \mathbf{M} \cdot \mathbf{d} \implies \mathbf{d} = \mathbf{M}^{-1} \cdot \mathbf{v}_{ref} \tag{2.9}$$

Where,

$$\mathbf{v}_{ref} = \left[v_{aref}\ v_{bref}\ v_{cref}\right]^T, \quad \mathbf{d} = \left[d_1\ d_2\ d_3\right]^T$$

$$\mathbf{M} = \begin{bmatrix} V_{d1_{aN}} & V_{d2_{aN}} & V_{d3_{aN}} \\ V_{d1_{bN}} & V_{d2_{bN}} & V_{d3_{bN}} \\ V_{d1_{cN}} & V_{d2_{cN}} & V_{d3_{cN}} \end{bmatrix}$$

Table. 2.1 can be used to determine the elements of $\mathbf{M}$, which are the terminal voltages corresponding to non-zero switching vectors.

Step 2: For a switching period T_s, the switching intervals T_1, T_2, T_3 and T_0 for the switching vectors V_{d1}, V_{d2}, V_{d3} and V_{d0} respectively, can be obtained using eqn. (2.10).

$$\begin{aligned} T_1 &= d_1 \cdot T_s \\ T_2 &= d_2 \cdot T_s \\ T_3 &= d_3 \cdot T_s \\ T_0 &= T_s - (T_1 + T_2 + T_3) \end{aligned} \tag{2.10}$$

Sequencing of the switching vectors

The switching vectors V_{d0}, V_{d1}, V_{d2}, and V_{d3} can be arranged according to whether the optimization desired is a reduction in switching losses or a reduction in total harmonic distortion. The symmetrically aligned sequencing shown in Fig. 2.13 is preferable for low output voltage and current distortion. In this scheme, the switching vector V_1 is chosen as the zero-switching vector (V_{d0}).

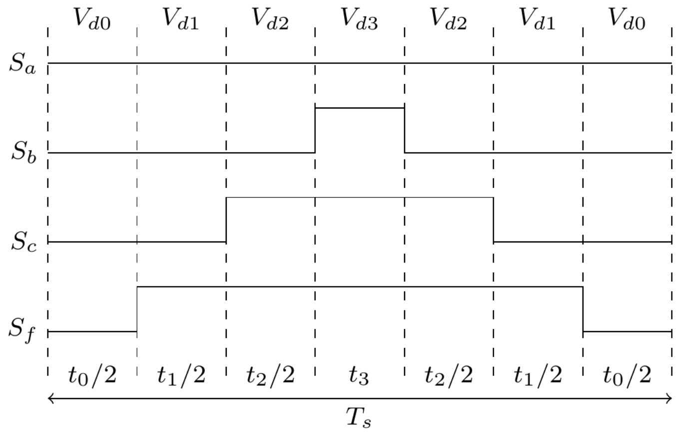

Fig. 2.13 Sequencing of the switching vectors

2.2.2 3-D SVM in $\alpha\beta\gamma$ coordinates

The 3D-SVM with $\alpha\beta\gamma$ coordinates proposed in [?] has been employed in this work. A 3-D $\alpha\beta\gamma$ orthogonal reference frame has been used to represent the switching vectors and the reference space vector as given in eqn. (2.11). The transformation from *abc* coordinate to $\alpha\beta\gamma$ coordinate can be performed using eqn. (2.12).

$$v_{\alpha\beta\gamma ref} = v_{\alpha ref} + jv_{\beta ref} + kv_{\gamma ref} \tag{2.11}$$

$$\begin{bmatrix} v_\alpha \\ v_\beta \\ v_\gamma \end{bmatrix} = \frac{2}{3} \begin{bmatrix} 1 & -\frac{1}{2} & -\frac{1}{2} \\ 0 & \frac{\sqrt{3}}{2} & -\frac{\sqrt{3}}{2} \\ \frac{1}{2} & \frac{1}{2} & \frac{1}{2} \end{bmatrix} \begin{bmatrix} v_a \\ v_b \\ v_c \end{bmatrix} \tag{2.12}$$

By using eqn. (2.12), the ac terminal voltage (v_{aN}, v_{bN}, v_{cN}) from Table. 2.1 is transformed into $(v_\alpha, v_\beta, v_\gamma)$ in $\alpha\beta\gamma$ coordinates. The transformed values can be found in Table. 2.3. Fig. 2.14 shows the 3-D control space consisting of sixteen switching vectors. The synthesis of the reference vector is discussed next.

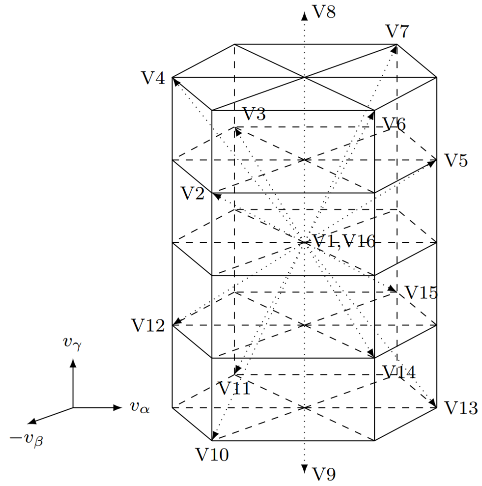

Fig. 2.14 Switching vectors in $\alpha\beta\gamma$ coordinates

Selection of the switching vectors:

The control space shown in Fig. 2.14 can be divided into six prisms, each of which can be further divided into four tetrahedrons. The switching vector can be identified by first identifying the prism that contains the reference vector, followed by identifying the specific tetrahedron within that prism. The selection of the switching vectors involves the following steps:

Step 1: The instantaneous values of the reference voltage v_{aref}, v_{bref}, and v_{cref} in *abc* coordinate are first converted into $v_{\alpha ref}$, $v_{\beta ref}$, and $v_{\gamma ref}$ in $\alpha\beta\gamma$ coordinate using eqn. (2.12).

Step 2: To identify the prism, the reference vector $v_{ref} + jv_{ref} + kv_{ref}$ is projected onto the $\alpha - \beta$ plane. The identification of the prism is carried out using eqns. (2.13) and (2.14).

$$\theta = tan^{-1}\left(\frac{v_{\beta ref}}{v_{\alpha ref}}\right) \tag{2.13}$$

Table 2.3 Switching states with the associated terminal voltages and switching vectors for $\alpha\beta\gamma$ coordinate.

State	Vector	S_a	S_b	S_c	S_N	v_α	v_β	v_γ
1	V_1	0	0	0	0	0	0	0
2	V_2	0	0	1	0	$-\frac{1}{3}V_{dc}$	$-\frac{1}{\sqrt{3}}V_{dc}$	$\frac{1}{3}V_{dc}$
3	V_3	0	1	0	0	$-\frac{1}{3}V_{dc}$	$\frac{1}{\sqrt{3}}V_{dc}$	$\frac{1}{3}V_{dc}$
4	V_4	0	1	1	0	$-\frac{2}{3}V_{dc}$	0	$\frac{2}{3}V_{dc}$
5	V_5	1	0	0	0	$\frac{2}{3}V_{dc}$	0	$\frac{1}{3}V_{dc}$
6	V_6	1	0	1	0	$\frac{1}{3}V_{dc}$	$-\frac{1}{\sqrt{3}}V_{dc}$	$\frac{2}{3}V_{dc}$
7	V_7	1	1	0	0	$\frac{1}{3}V_{dc}$	$\frac{1}{\sqrt{3}}V_{dc}$	$\frac{2}{3}V_{dc}$
8	V_8	1	1	1	0	0	0	V_{dc}
9	V_9	0	0	0	1	0	0	$-V_{dc}$
10	V_{10}	0	0	1	1	$-\frac{1}{3}V_{dc}$	$-\frac{1}{\sqrt{3}}V_{dc}$	$-\frac{2}{3}V_{dc}$
11	V_{11}	0	1	0	1	$-\frac{1}{3}V_{dc}$	$\frac{1}{\sqrt{3}}V_{dc}$	$-\frac{2}{3}V_{dc}$
12	V_{12}	0	1	1	1	$-\frac{2}{3}V_{dc}$	0	$-\frac{1}{3}V_{dc}$
13	V_{13}	1	0	0	1	$\frac{2}{3}V_{dc}$	0	$-\frac{2}{3}V_{dc}$
14	V_{14}	1	0	1	1	$\frac{1}{3}V_{dc}$	$-\frac{1}{\sqrt{3}}V_{dc}$	$-\frac{1}{3}V_{dc}$
15	V_{15}	1	1	0	1	$\frac{1}{3}V_{dc}$	$\frac{1}{\sqrt{3}}V_{dc}$	$-\frac{1}{3}V_{dc}$
16	V_{16}	1	1	1	1	0	0	0

$$Prism = \begin{cases} I, & 0 \le \theta < \frac{\pi}{3} \\ II, & \frac{\pi}{3} \le \theta < \frac{2\pi}{3} \\ III, & \frac{2\pi}{3} \le \theta < \pi \\ IV, & \pi \le \theta < \frac{4\pi}{3} \\ V, & \frac{4\pi}{3} \le \theta < \frac{5\pi}{3} \\ VI, & \frac{5\pi}{3} \le \theta < 2\pi \end{cases} \tag{2.14}$$

Step 3: Positive, negative, or zero polarity voltage can be generated at the line-to-neutral terminals by each non-zero switching vector. A non-conflicting line-to-neutral terminal voltage is produced by the non-zero space vectors in each tetrahedron. To identify the tetrahedrons in a prism, the voltage polarities of the reference voltages v_{aref}, v_{bref}, and v_{cref} are compared with the polarities of the non-zero switching vectors of each tetrahedron. The tetrahedron with the same non-conflicting voltage polarities as the reference voltage is selected. Table 2.4 can be used to select a tetrahedron and non-zero switching vector based on a comparison of voltage polarity.

Table 2.4 Selection of tetrahedron and switching vectors based on voltage polarities.

Prism	Tetrahedron	$(V_{d1},\ V_{d2},\ V_{d3})$	Polarity
I	I	V_5, V_{13}, V_{15}	$v_{aref} \geq 0$; $v_{bref} \leq 0$; $v_{cref} \leq 0$
	II	V_5, V_7, V_{15}	$v_{aref} \geq 0$; $v_{bref} \geq 0$; $v_{cref} \leq 0$
	III	V_5, V_7, V_8	$v_{aref} > 0$; $v_{bref} \geq 0$; $v_{cref} \geq 0$
	IV	V_{13}, V_{15}, V_9	$v_{aref} \leq 0$; $v_{bref} \leq 0$; $v_{cref} < 0$
II	I	V_7, V_{15}, V_3	$v_{aref} \geq 0$; $v_{bref} \geq 0$; $v_{cref} \leq 0$
	II	V_{15}, V_3, V_{11}	$v_{aref} \leq 0$; $v_{bref} \geq 0$; $v_{cref} \leq 0$
	III	V_7, V_3, V_8	$v_{aref} \geq 0$; $v_{bref} > 0$; $v_{cref} \geq 0$
	IV	V_{15}, V_{11}, V_9	$v_{aref} \leq 0$; $v_{bref} \leq 0$; $v_{cref} < 0$
III	I	V_3, V_{11}, V_{12}	$v_{aref} \leq 0$; $v_{bref} \geq 0$; $v_{cref} \leq 0$
	II	V_3, V_4, V_{12}	$v_{aref} \leq 0$; $v_{bref} \geq 0$; $v_{cref} \geq 0$
	III	V_3, V_4, V_8	$v_{aref} \geq 0$; $v_{bref} > 0$; $v_{cref} \geq 0$
	IV	V_{11}, V_{12}, V_9	$v_{aref} < 0$; $v_{bref} \leq 0$; $v_{cref} \leq 0$
IV	I	V_4, V_{12}, V_2	$v_{aref} \leq 0$; $v_{bref} \geq 0$; $v_{cref} \geq 0$
	II	V_{12}, V_2, V_{10}	$v_{aref} \leq 0$; $v_{bref} \leq 0$; $v_{cref} \geq 0$
	III	V_4, V_2, V_8	$v_{aref} \geq 0$; $v_{bref} \geq 0$; $v_{cref} > 0$
	IV	V_{12}, V_{10}, V_9	$v_{aref} < 0$; $v_{bref} \leq 0$; $v_{cref} \leq 0$
V	I	V_2, V_{10}, V_{14}	$v_{aref} \leq 0$; $v_{bref} \leq 0$; $v_{cref} \geq 0$
	II	V_2, V_6, V_{14}	$v_{aref} \geq 0$; $v_{bref} \leq 0$; $v_{cref} \geq 0$
	III	V_2, V_6, V_8	$v_{aref} \geq 0$; $v_{bref} \geq 0$; $v_{cref} > 0$
	IV	V_{10}, V_{14}, V_9	$v_{aref} \leq 0$; $v_{bref} < 0$; $v_{cref} \leq 0$
VI	I	V_6, V_{14}, V_5	$v_{aref} \geq 0$; $v_{bref} \leq 0$; $v_{cref} \geq 0$
	II	V_{14}, V_5, V_{13}	$v_{aref} \geq 0$; $v_{bref} \leq 0$; $v_{cref} \leq 0$
	III	V_6, V_5, V_8	$v_{aref} > 0$; $v_{bref} \geq 0$; $v_{cref} \geq 0$
	IV	V_{14}, V_{13}, V_9	$v_{aref} \leq 0$; $v_{bref} < 0$; $v_{cref} \leq 0$

Calculation of duty cycles and switching duration:

Step 1: The duty cycles, d_i, for each non-zero switching vector is then determined using eqn. (2.15).

$$\mathbf{v}_{\alpha\beta\gamma ref} = \mathbf{M}_{\alpha\beta\gamma} \cdot \mathbf{d} \implies \mathbf{d} = \mathbf{M}_{\alpha\beta\gamma}^{-1} \cdot \mathbf{v}_{\alpha\beta\gamma ref} \tag{2.15}$$

Where,

$$\mathbf{v}_{\alpha\beta\gamma ref} = \left[v_{\alpha ref}\ v_{\beta ref}\ v_{\gamma ref}\right]^T, \quad \mathbf{d} = \left[d_1\ d_2\ d_3\right]^T$$

$$\mathbf{M}_{\alpha\beta\gamma} = \begin{bmatrix} V_{d1_\alpha} & V_{d2_\alpha} & V_{d3_\alpha} \\ V_{d1_\beta} & V_{d2_\beta} & V_{d3_\beta} \\ V_{d1_\gamma} & V_{d2_\gamma} & V_{d3_\gamma} \end{bmatrix}$$

Table. 2.3 can be used to determine the elements of $\mathbf{M}_{\alpha\beta\gamma}$.

Step 2: For a switching period T_s, the switching intervals T_1, T_2, T_3 and T_0 for the switching vectors V_{d1}, V_{d2}, V_{d3} and V_{d0} respectively, can be obtained using eqn. (2.16).

$$\begin{aligned} T_1 &= d_1 \cdot T_s \\ T_2 &= d_2 \cdot T_s \\ T_3 &= d_3 \cdot T_s \\ T_0 &= T_s - (T_1 + T_2 + T_3) \end{aligned} \tag{2.16}$$

2.3 MATLAB/Simulink modelling of 3-D SVM

MATLAB/Simulink is a widely used and powerful simulation software package for the development and simulation of power systems and power electronic systems. While MATLAB/Simulink modelling of 2-D SVM for three-leg converters is available [**? ?**], there have been no reported works for 3-D SVM of the four-leg converter. This section presents a step-by-step procedure for modelling the 3-D SVM in both *abc* and $\alpha\beta\gamma$ coordinate systems for the four-leg converter. The resulting models can be utilized for power system studies involving the four-leg inverter.

This section focuses on the development of a 3-D SVM MATLAB/Simulink model. The model consists of multiple sub-systems, each serving a specific purpose. The developed Simulink model is shown in Fig. 2.15. The various sub-systems employed in the development of the model are as follows:

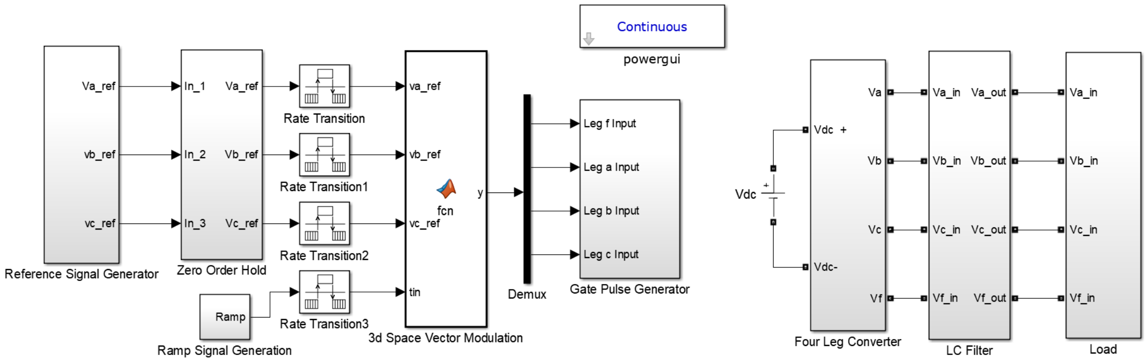

Fig. 2.15 3-D SVM MATLAB/Simulink developed model

Reference signal generation

The three-phase reference signal is generated using three sine wave generators, with the current simulation time provided by a clock. The ‘Clock’ block and the ‘Sine Wave’ blocks are included in the sub-system from the ‘Sources’ library. In order to observe the generated reference signal, the sub-system incorporates a ‘Mux’ from the

'Signal Routing' library and a 'Scope' from the 'Sinks' library. The sub-system itself is displayed in Fig. 2.16.

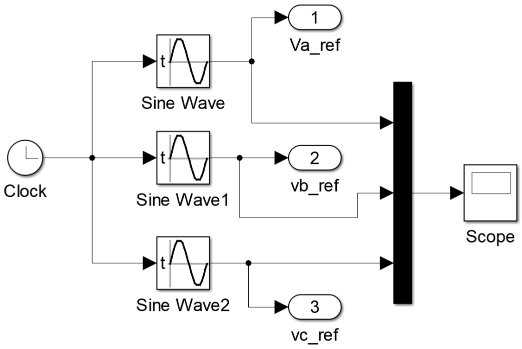

Fig. 2.16 Reference signal generation sub-system

Zero order hold

To ensure the algorithm operates correctly, it is necessary to maintain the reference voltage constant for one switching period, T_s. To accomplish this, a sub-system containing 'Zero-Order Hold' blocks from the 'Discrete' library is incorporated after the reference signal generator sub-system. The sub-system is illustrated in Fig. 2.17. The Zero-Order Holders sample the reference signal at the predetermined switching frequency, thereby altering the output of the block only after each switching period. Additionally, a Mux and a Scope are included to monitor the output signal.

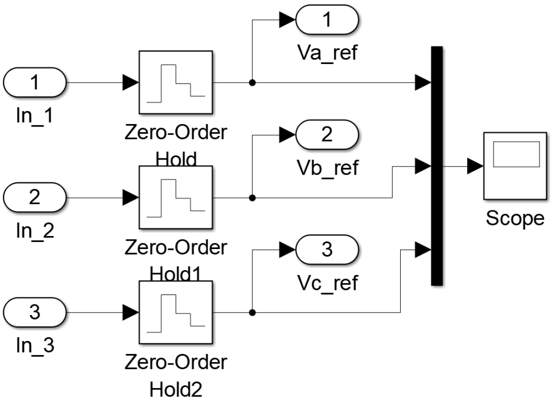

Fig. 2.17 Zero-order hold subsystem

Ramp signal generation

As previously explained, the 3-D SVM employs four switching vectors that are applied in a specific sequence throughout the switching period. This process is depicted in

Fig. 2.13. The algorithm determines the duration for which each switching vector is applied. To enable the sequencing of switching vectors, a reference time signal is generated using a ramp signal generator sub-system. This sub-system creates a ramp signal that transitions from 0 to T_s over one switching period. The 3-D SVM MATLAB function block then utilizes this signal to sequence the switching vectors. The sub-system responsible for generating the ramp signal is developed using a 'Sawtooth Generator' from the 'Simscape Power Systems > Specialized Technology > Control and Measurements > Pulse and Signal Generators' library, and the frequency is set to the switching frequency. By default, the sawtooth wave varies from -1 to 1, so to produce a sawtooth wave that varies from 0 to T_s, the 'Add' and 'Product' block from the 'Math Operations' library, along with the 'Constant' blocks from the 'Sources' library are employed. Finally, a 'Scope' is included to observe the output ramp signal. The resulting sub-system is illustrated in Fig. 2.18.

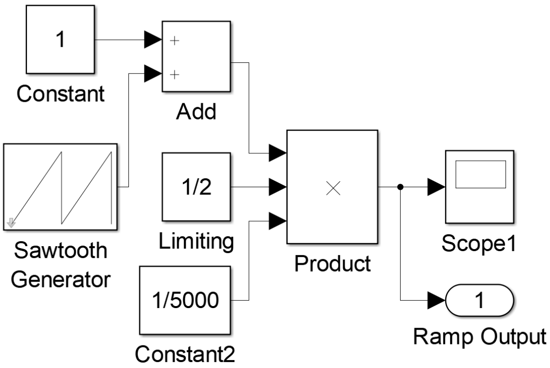

Fig. 2.18 Ramp signal generator subsystem

Rate transition block

Due to the fact that the output of the Zero-Order Holders changes only after each switching period, but the output of the ramp signal generator is a ramp that continuously transitions from 0 to T_s in one switching period, 'Rate Transition' blocks from the 'Signal Attributes' library are inserted. These blocks are utilized to transmit the reference voltage and reference time to the 3-D SVM MATLAB function block.

3-D SVM MATLAB function block

In this block, the three-phase reference voltages and the reference time are taken as inputs, and the corresponding gate signals for the upper switches of the converter are produced as outputs. To accomplish this, the 'MATLAB Function' block from the 'User Defined Functions' library is employed. The MATLAB code for generating the gate signals for the four-leg inverter is developed by following the steps described in Sec. (2.2) for implementing the 3-D SVM. For a given instantaneous value of the reference voltage, both the 3-D SVM in *abc* coordinates and the 3-D SVM in $\alpha\beta\gamma$

coordinates use the same inputs. The algorithms select three non-zero switching vectors and one zero switching vector to generate the reference space vector. Regardless of the chosen method, the switch states during a switching period remain similar, resulting in similar gate signals being generated. Therefore, the waveforms obtained from both techniques are identical. However, the 3-D SVM with $\alpha\beta\gamma$ coordinates incurs an additional processing overhead due to the transformation from *abc* to $\alpha\beta\gamma$ coordinates.

Gate pulse generator

The gate pulse generator sub-system is responsible for generating the gate signals for the four lower switches of the converter. It takes the gate signals for the converter's upper switches from the 3-D SVM MATLAB function block as input. The output of this sub-system is the gate signals for all eight switches of the four-leg inverter. To model this sub-system, 'Logical Operator' blocks from the 'Logic and Bit Operations' library are used, with the operator parameter set to 'NOT'. The sub-system, as shown in Fig. 2.19, directs the output signals to the gate terminals of the switches in the four-leg converter.

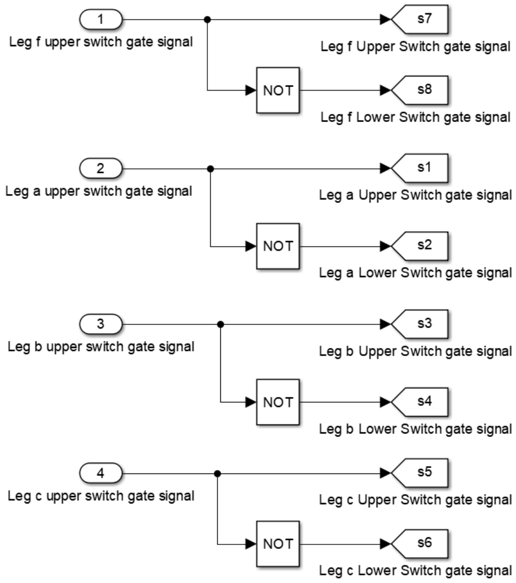

Fig. 2.19 Gate signal generator subsystem

Four-Leg inverter

The 'IGBT/Diode' block from the 'Simscape Power System > Power Electronics' library is used to implement the four-leg converter, as shown in Fig. 2.20. The converter is powered by a DC supply implemented using the 'DC Voltage Source' block from the 'Simscape Power System > Electrical Sources and Elements' library. 'Scopes' and a 'Three-Phase V-I Measurement' block from the 'Simscape Power System > Sensors and

Measurements' library are added to observe the output phase voltages and currents of the converter. An LC filter is used to connect the output terminals of the converter.

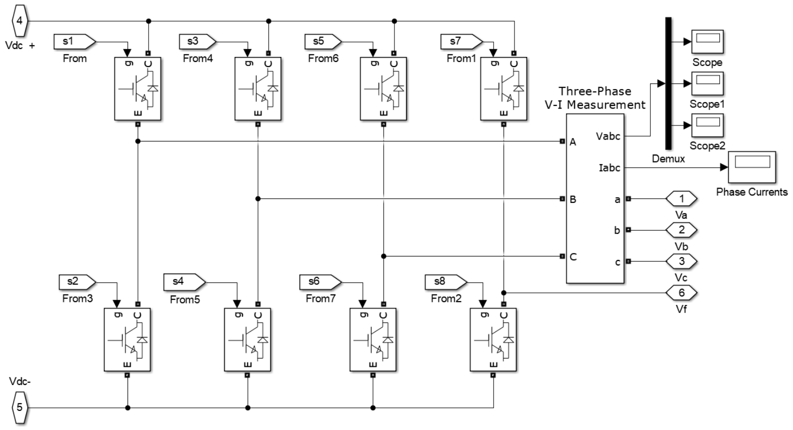

Fig. 2.20 Four-leg inverter subsystem

LC filter

To keep the total harmonic distortion of the output voltage and current below acceptable limits, a coupling LC filter is added to the inverter's output. Fig. 2.21 shows the implementation of the LC filter sub-system, which utilizes 'Series RLC branch' blocks from the 'Simscape Power System > Electrical Sources and Elements' library. The filter's output is then connected to a three-phase load.

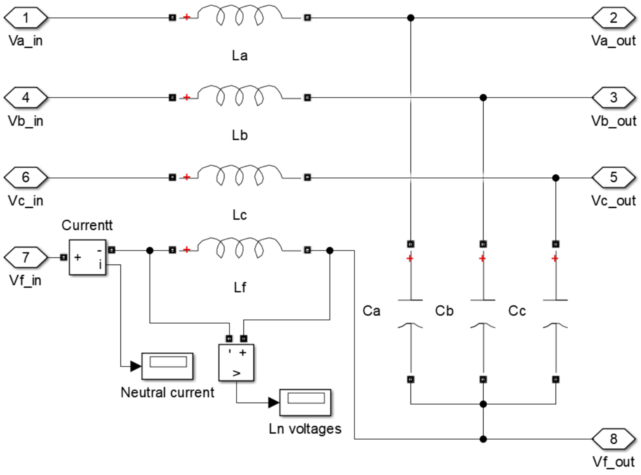

Fig. 2.21 LC filter subsystem

Three-phase load

The implementation of the three-phase load shown in Fig. 2.22 is carried out using the ‘Series RLC branch’ blocks from the ‘Simscape Power System > Electrical Sources and Elements’ library. The measurement of output phase voltage and line currents is performed using the ‘Three-Phase VI Measurement’ block, while the measurement of line voltages is performed using the ‘Voltage Measurement’ block, both of which are part of the ‘Simscape Power System > Electrical Sources and Elements’ library. The observed output waveforms are displayed on ‘Scopes’.

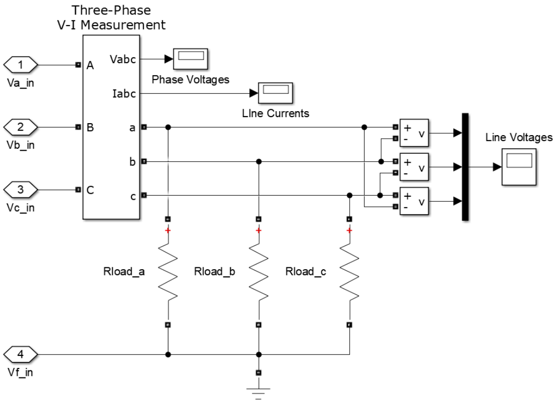

Fig. 2.22 Three-phase unbalanced load

2.4 Simulation results and analysis

To put the developed model to the test, an unbalanced three-phase reference signal is generated and fed into the system. Fig. 2.23 shows the reference signal.

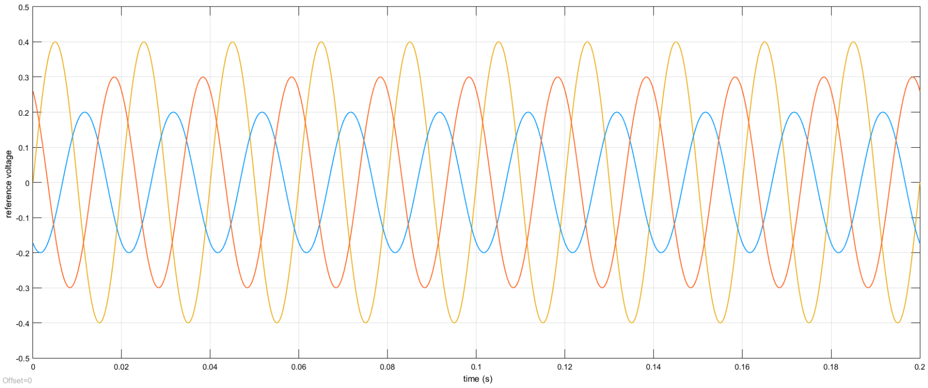

Fig. 2.23 Unbalanced three-phase reference signal

The zero-order hold subsystem receives the reference signal. Fig. 2.24 depicts the output of the zero-order hold subsystem. The switching frequency for this simulation is set to 5 kHz.

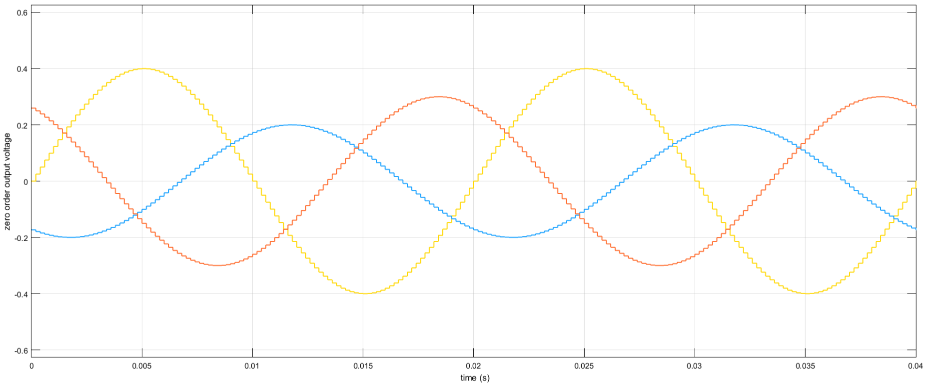

Fig. 2.24 Output waveform from the zero-order hold sub-system

The ramp signal generator sub-system is used to generate a ramp signal that changes from 0 to 0.0002 during the switching period of 0.2 ms. This ramp signal is utilized as the time reference for the 3D-SVM MATLAB function. Fig. 2.25 illustrates the output of the ramp signal generator.

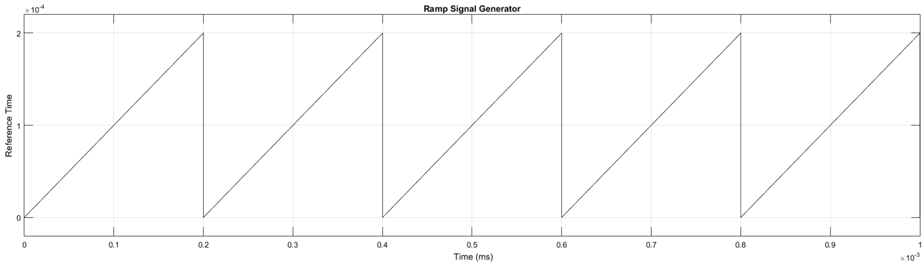

Fig. 2.25 Ramp signal generator output waveform

The input signals to the 3D-SVM MATLAB function block are the reference signal and reference time, which are used to generate the gate control signal for the converter's upper switches. The output of this block is then used as an input to the gate pulse generator sub-system, which produces the control signal for all eight switches. Fig. 2.26 shows the gate control signals for the converter's upper switches.

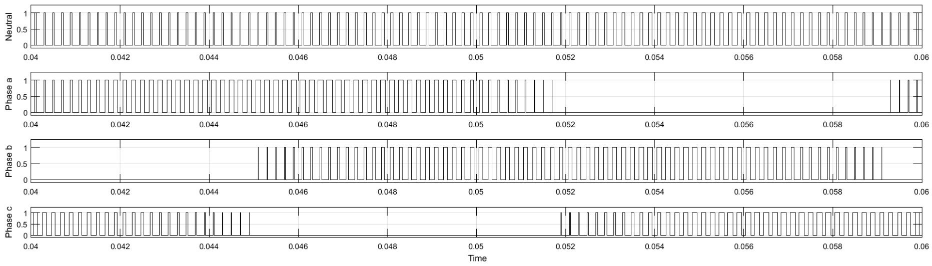

Fig. 2.26 Gate control signals for the upper switches of the four-leg converter

The output voltage of phase '*a*' of the four-leg converter is displayed in Fig. 2.27 without any filtering. The output exhibits a very high total harmonic distortion; hence, the output is passed through an LC filter. The output of the LC filter is then connected to a resistive load with three phases. The resulting output voltage after passing through the filter is shown in Fig. 2.28. Based on the results, it can be concluded that the developed model is capable of unbalanced operation.

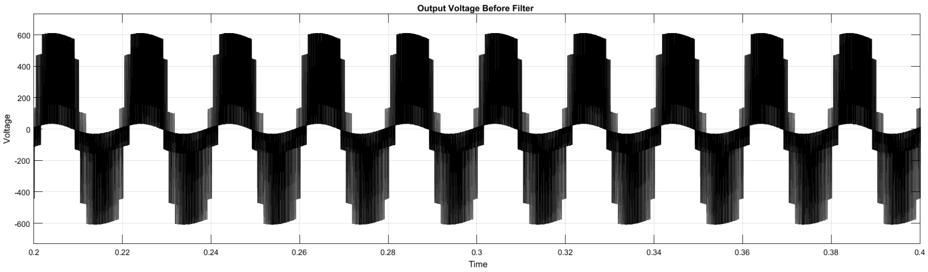

Fig. 2.27 Output voltage waveform of phase a before filter

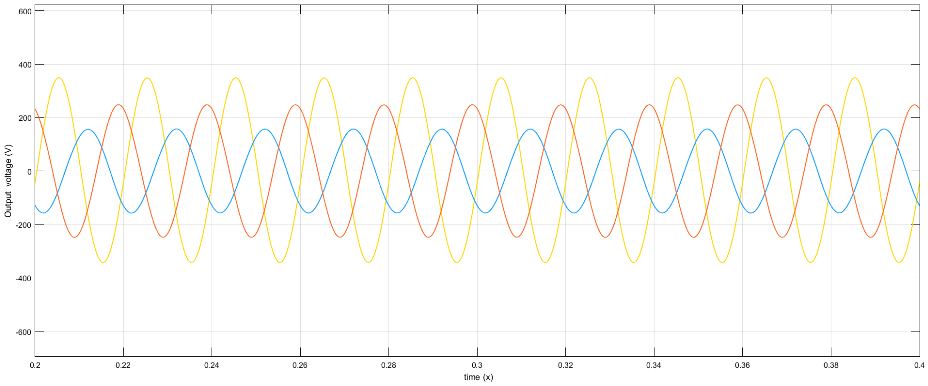

Fig. 2.28 Output voltage waveform of inverter after filter

2.5 Controller design for injection of negative sequence current using four-leg inverters

It has been established in Sec. (2.1) that injecting appropriate values of negative sequence current can reduce the voltage unbalance in a low voltage microgrid. With the help of converters, which facilitate independent control of the three-phases, negative sequence current can be injected into the microgrid, allowing unbalance voltage correction. By comparing various such converters, it has been found that the four-leg inverter is suitable for interfacing DERs to low-voltage microgrids with voltage unbalance problems.

As the primary function of any inverter interfacing a DER to a microgrid is to supply the microgrid with real and reactive power, therefore, the controller for the four-leg inverter must be capable of injecting both positive sequence current to supply the desired real and reactive power, as well as negative sequence current to correct unbalance voltage. A control scheme developed for injecting both positive and negative sequence current into the microgrid using the four-leg inverter is described in this section. Fig. 2.29 shows the block diagram of the proposed controller.

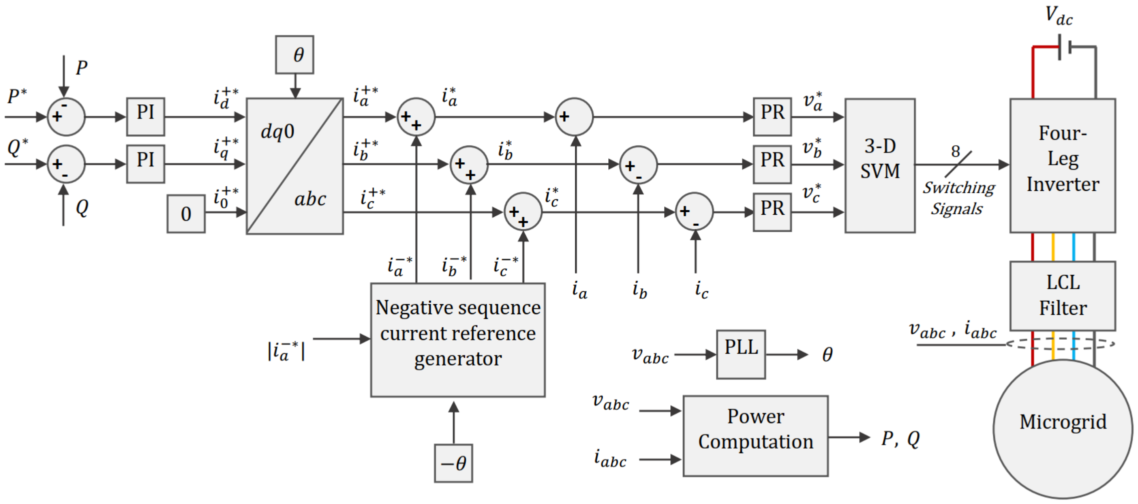

Fig. 2.29 Control scheme for injecting positive and negative sequence current into the microgrid using the four-leg inverter

The DER is integrated into the microgrid through a four-leg inverter and a LCL filter. The switching signals for the inverter are generated using the 3-D SVM technique discussed in the previous section. The three-phase reference signal for 3-D SVM is generated by three proportional-resonant (PR) controllers. The inputs to PR controllers are the error signal of the actual inverter current and the reference three-phase currents. PR controllers are best suited for this application due to their superior performance in handling sinusoidal references [?]. The reference current for the three phases is calculated by summing the positive and negative sequence reference currents. The positive sequence reference currents are derived from the positive d and q components using reverse Park's transformation as given in eqn. (2.17) [?]. The positive d and q components are obtained from two PI controllers, where the d component regulates the dc-link voltage and is responsible for the active power of the inverter, and the q component adjusts the reactive power injection [?]. The phase information required for reverse Park's transformation is obtained from a PLL unit. The negative sequence current is generated by the negative sequence generator block using eqn. (2.18)

$$\begin{bmatrix} I_a^+ \\ I_b^+ \\ I_c^+ \end{bmatrix} = \begin{bmatrix} cos(\theta) & sin(\theta) & 1 \\ cos(\theta - \frac{2\pi}{3}) & sin(\theta - \frac{2\pi}{3}) & 1 \\ cos(\theta + \frac{2\pi}{3}) & sin(\theta + \frac{2\pi}{3}) & 1 \end{bmatrix} \begin{bmatrix} i_d^+ \\ i_q^+ \\ i_0^+ \end{bmatrix} \tag{2.17}$$

$$\begin{bmatrix} I_a^{-*} \\ I_b^{-*} \\ I_c^{-*} \end{bmatrix} = \begin{bmatrix} |I_a^{-*}|sin(-\theta) \\ |I_a^{-*}|sin(-\theta + \frac{2\pi}{3}) \\ |I_a^{-*}|sin(-\theta - \frac{2\pi}{3}) \end{bmatrix} \tag{2.18}$$

2.6 Simulation results for negative sequence current injection using four-leg inverters

A Simulink model, shown in Fig.2.30, is developed to implement the controller. The system comprises a simple network containing a four-leg inverter that is controlled using the control scheme discussed in the previous section. A circuit breaker, which acts as the PCC, connects the inverter to a microgrid. The microgrid consists of a balanced three-phase source and a distribution network. An unbalanced three-phase load is connected at the PCC. The objective of the study is to investigate the effect of negative sequence current injection on voltage unbalance at the point of inverter connection. Table. 2.5 shows the parameters used for the simulation.

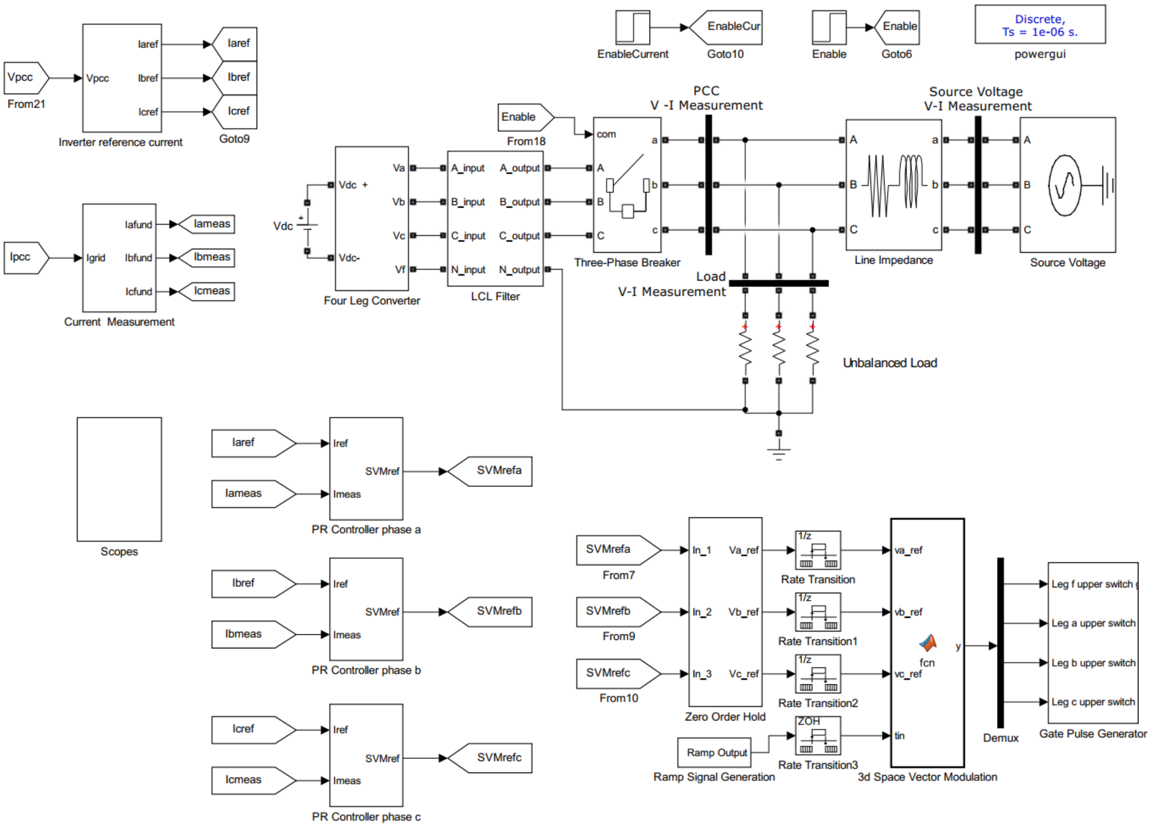

Fig. 2.30 Simulink model for positive and negative sequence current injection using four-leg inverter

Table 2.5 Parameter settings for simulation of negative sequence current injection

Parameter	Value
P^*	0 kW
Q^*	0 KVAR
PI gain	0.1 & 10
V_{L-G}	230 V
PR gain	0.1 & 100
Switching frequency	5 kHz
DC link voltage	700 V
Grid side inductor	1 mH
Inverter side inductor	0.5 mH
Inverter capacitor	45 μF
Inductor resistance	0.04 Ω
Phase a load	9 kW
Phase b load	4 kW
Phase c load	1 kW

The inverter is initially disconnected from the microgrid. As a result, the positive and negative sequence current demands of the unbalanced load are met by the three-phase source. Two case studies are performed. In the first case, the magnitude of the negative sequence current is held constant while the phase angle is changed. At $t = 0.2$ sec, the inverter is connected to the microgrid, and a negative sequence current of $5\angle 0°$ is injected into the grid. A negative sequence current of $5\angle 90°$ is then injected into the grid at $t = 0.4$ sec, followed by injections of $5\angle 180°$ at $t = 0.6$ sec and $5\angle -90°$ at $t = 0.8$ sec. Fig. 2.31 depicts the negative sequence current reference for phase a. Fig. 2.32 depicts the resulting positive and negative sequence component of voltage at PCC for the five time intervals. As seen in Fig. 2.32, the negative sequence voltage at the PCC when no negative sequence current is injected is 10 V. When a negative sequence current of $5\angle 0°$ is injected, the negative sequence voltage at PCC is found to be 13.7 V. For $5\angle 90°$, $5\angle 180°$ and $5\angle -90°$ the negative sequence voltage is found to be 9.3 V, 6.8 V, and 12.3 V, respectively. The results show that depending on the phase angle, the voltage unbalance can improve, as seen for the negative sequence current injections of $5\angle 90°$ and $5\angle 180°$, or worsen, as seen for the cases of $5\angle 0°$ and $5\angle -90°$. Further, it can be seen that higher unbalance correction is obtained at $5\angle 180°$ during the time interval 0.6 sec to 0.8 sec. The change in voltage unbalance for all of the negative sequence current test values at different time intervals can also be observed in the voltage waveform at the PCC, as shown in Fig. 2.33.

In the second case, the magnitude and phase angle of the negative sequence current are both changed. At $t = 0.2$ sec, the inverter connects to the microgrid and injects a negative sequence current of $3\angle 0°$ into the grid. At $t = 0.4$ sec, a negative sequence current of $7\angle 0°$ is injected into the grid, followed by negative sequence currents of

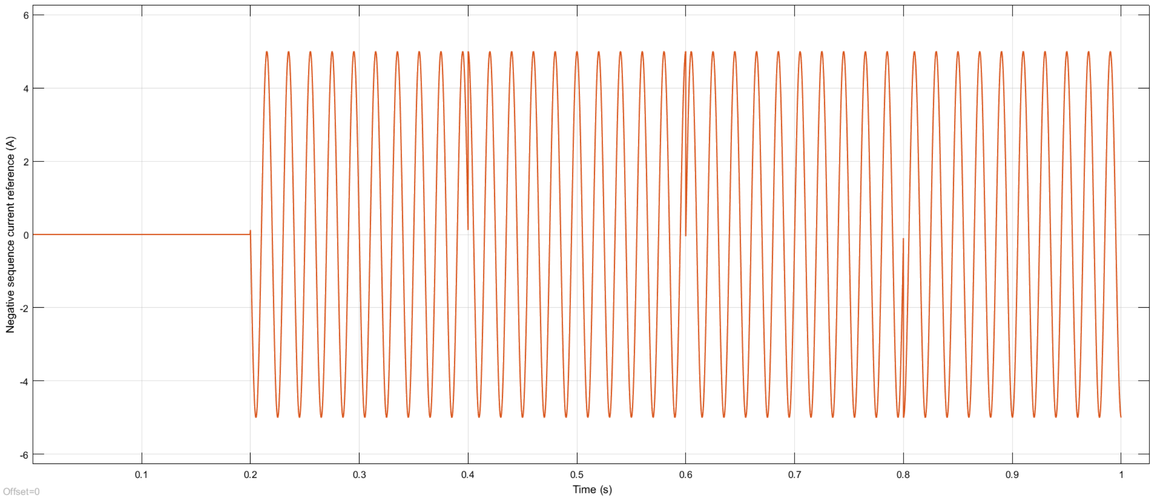

Fig. 2.31 The negative sequence current reference for phase *a* for case study 1

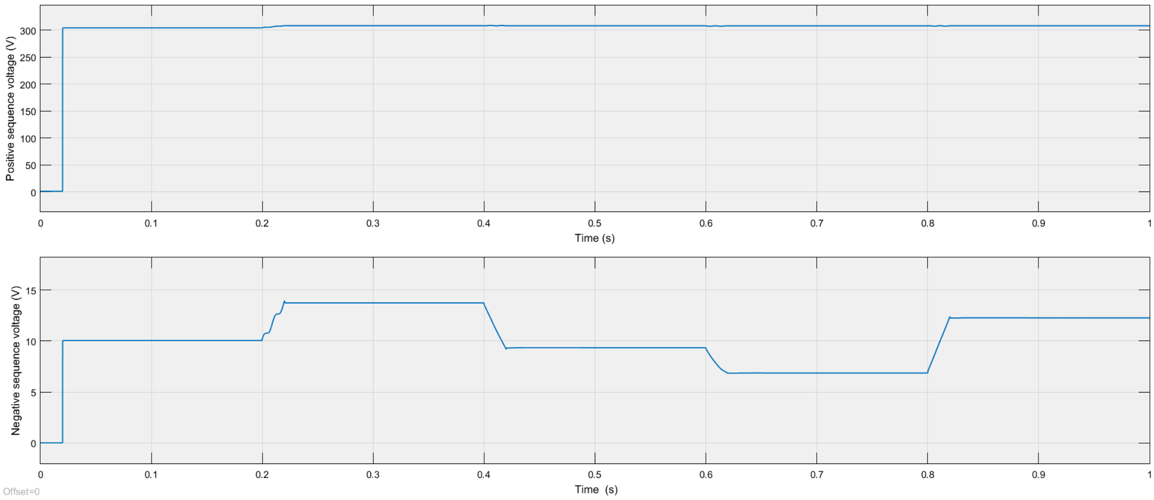

Fig. 2.32 Positive and negative sequence component of voltage at PCC for case study 1

3∠180° at $t = 0.6$ sec and 7∠180° at $t = 0.8$ sec. The negative sequence current reference for phase *a* is shown in Fig. 2.34. The resulting positive and negative sequence component of voltage at PCC for the five time intervals is shown in Fig. 2.35. In this case, when a negative sequence current of 3∠0° is injected, the negative sequence voltage at PCC is found to be 12.3 V. For negative sequence currents of 7∠0°, 3∠180°, and 7∠180°, the negative sequence voltage at PCC is found to be 15.2 V, 8.1 V, and 5.7 V respectively. Therefore, in this case, it is observed that the voltage unbalance is improved by the negative sequence current injections of 3∠180° and 7∠180° and is worsened by the negative sequence current injections of 3∠0° and 7∠0°. Therefore, it is indicated that the voltage unbalance can be improved or worsened depending on the magnitude and phase angle of the negative sequence current. The change in voltage

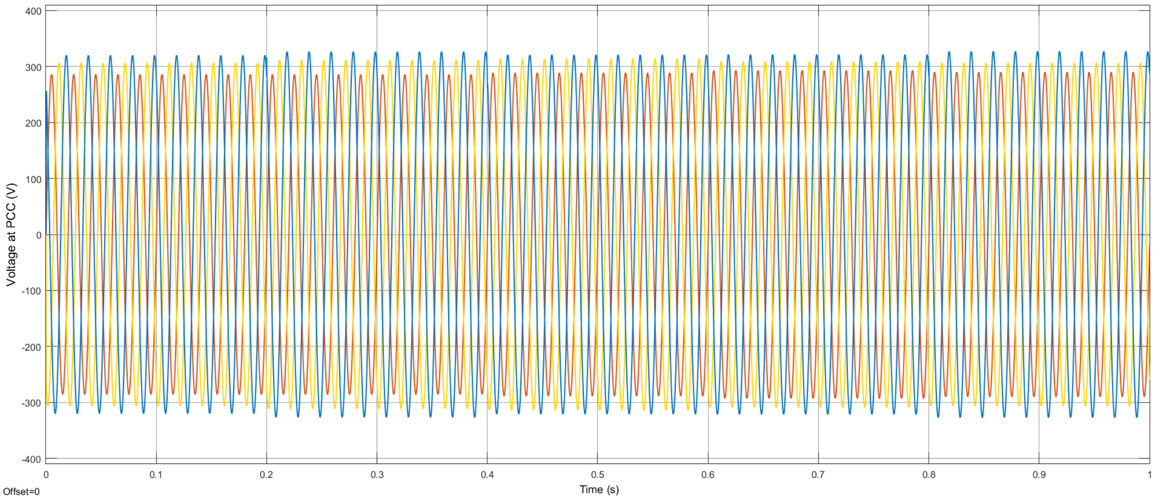

Fig. 2.33 Voltage at PCC for case study 1

unbalance at the PCC can also be seen from the voltage waveform at the PCC, as shown in Fig. 2.36.

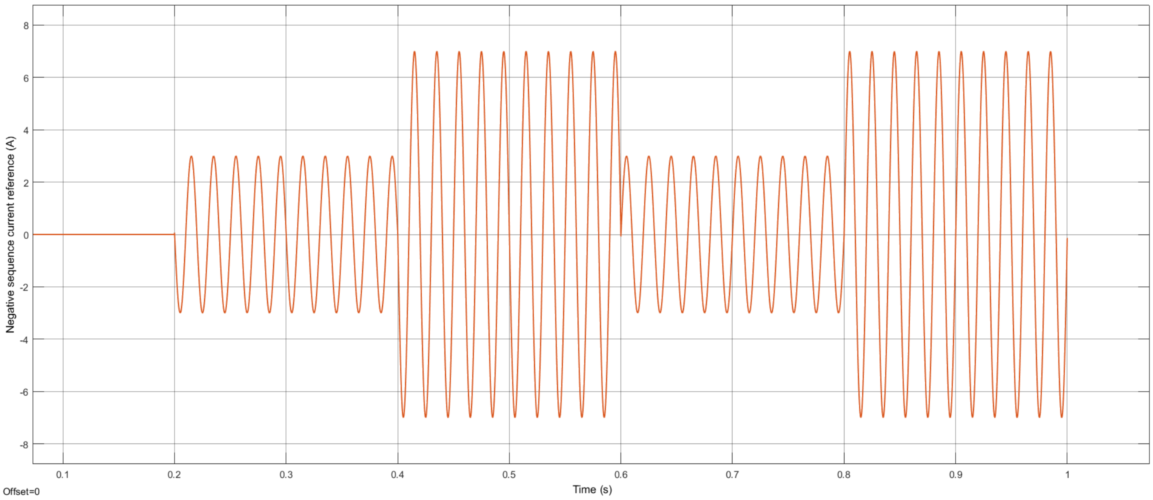

Fig. 2.34 The negative sequence current reference for phase a for case study 2

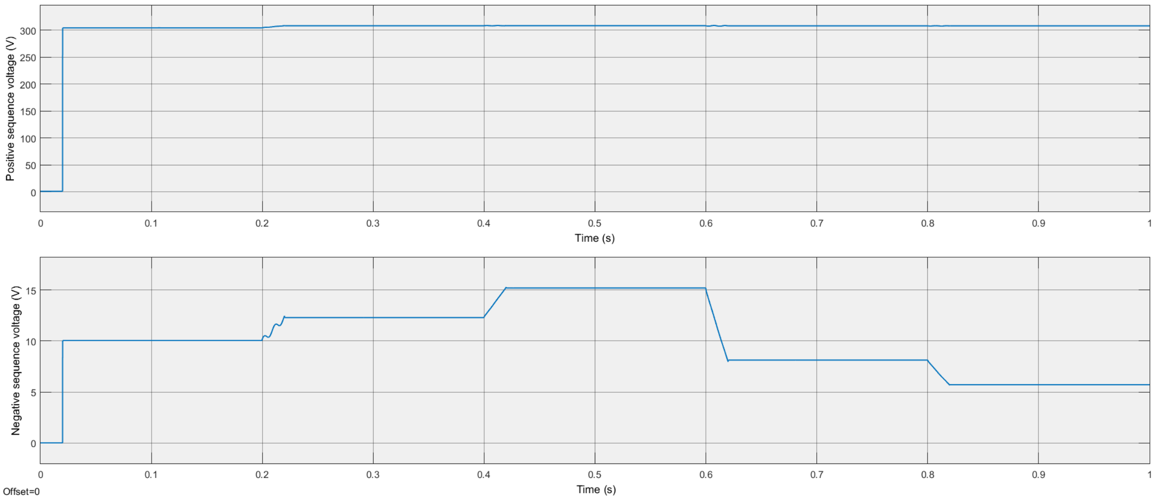

Fig. 2.35 Positive and negative sequence component of voltage at PCC for case study 2

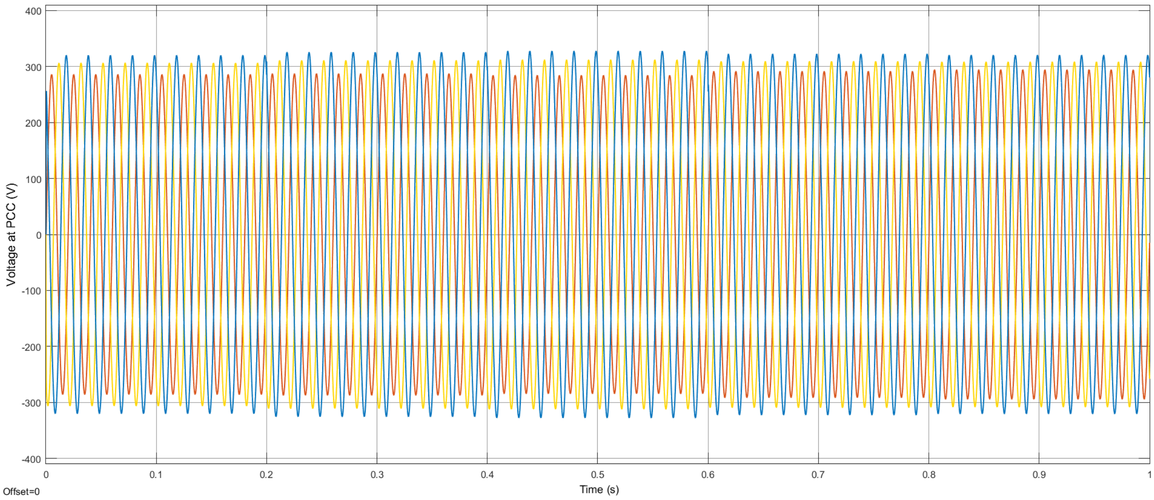

Fig. 2.36 Voltage at PCC for case study 2

The simulation results confirm that voltage unbalance in a microgrid can be reduced by injecting negative sequence currents into the microgrid using a four-leg inverter interfacing the DERs to the microgrid. However, as seen in both the case studies, certain values of negative sequence current can aggravate the voltage unbalance problem while others can improve it. As a result, search techniques for determining the optimal value of negative sequence current at which the voltage unbalance for a given state of the microgrid is minimal must be developed. In the following chapter, a perturb and observe-based unbalance voltage correction method will be proposed to determine the value of the negative sequence current for which the voltage unbalance is minimum.

2.7 Conclusion

Voltage unbalance is an important issue in low voltage microgrids. Voltage unbalance can be reduced if the converters used to connect the DERs into the microgrids are capable of injecting negative sequence current into the grid. This chapter investigates the significance of negative sequence current in unbalance voltage mitigation. Converters suitable for unbalanced operation are investigated, and the four-leg inverter due to its lower cost and complexity is selected for unbalance voltage correction. A comprehensive guide for developing a MATLAB/Simulink model to implement 3-D SVM in both the *abc* and $\alpha\beta\gamma$ coordinate systems is presented and tested. The chapter explains the necessary theory and steps for implementing 3-D SVM control techniques for the four-leg converter. It then goes on to discuss the different sub-systems used to develop the Simulink model. The developed model is tested through simulation with an unbalanced voltage reference, and the results confirm the model's functionality. It is important to note that implementing the model in the $\alpha\beta\gamma$ coordinate system requires additional processing overhead due to the transformation from *abc* to $\alpha\beta\gamma$ coordinates. Nevertheless, both methods produce similar results. The controller for injecting negative sequence current using a four-leg inverter is also developed. Simulations results indicate that certain values of negative sequence current can mitigate the voltage unbalance problem while others can worsen it. Therefore, there is a need for developing control techniques to find negative sequence current values for which voltage unbalance will be minimal. Thus, it is established in this chapter that the four-leg inverter with 3-D SVM can be used for unbalance voltage mitigation as it is capable of injecting negative sequence current by independently adjusting the three phases.

3

Perturb & observe based control of three-phase four-leg inverters to mitigate voltage unbalances in low voltage microgrids

The previous chapter demonstrated that supplying the negative sequence current demand of the load by the converters can mitigate voltage unbalance. However, estimating the negative sequence current demand is the main challenge in these types of correction methods. This chapter presents a novel perturb and observe (P&O) based control strategy for the Four-Leg Inverter interfaced distributed Generators (FLIGs) to reduce voltage unbalances in low voltage microgrids. The control strategy relies on calculating the voltage unbalance factor at the inverter connection point and injecting controlled amount of negative sequence current into the microgrid. The proposed method differs from existing methods involving negative sequence current injection using inverters in that it does not involve determining negative sequence line impedance magnitude or phase angle or measuring load or line currents. The proposed method presents a promising approach to mitigating voltage unbalances in low-voltage microgrids without requiring significant hardware modifications or communication between distributed generators.

3.1 Computation of voltage unbalance factor

The degree of voltage unbalance in a three phase system can be measured with the help of voltage unbalance factor. Voltage Unbalance Factor (VUF) is a measurement of the deviation of the voltage levels in a three-phase electrical system from their nominal or average values. Various definitions of the VUF have been proposed by various agencies. Eqns. (3.1), (3.2) and (3.3) represent three such definitions of voltage unbalance developed by National Electrical Manufacturers Association (NEMA), The Institute of Electrical and Electronics Engineers (IEEE), and the power community, respectively [?].

$$VUF = \frac{maximum\ deviation\ from\ \ the\ average\ line\ voltage}{average\ line\ voltage} \tag{3.1}$$

$$VUF = \frac{maximum\ deviation\ from\ \ the\ average\ phase\ voltage}{average\ phase\ voltage} \tag{3.2}$$

$$VUF = \frac{negative\ sequence\ voltage\ component}{positive\ sequence\ voltage\ component} \tag{3.3}$$

Eqns. (3.1) and (3.2) consider only the magnitude and ignore the phase angle information, whereas eqn. (3.3) considers both magnitude and phase angle and thus can more accurately measure the voltage unbalance of a system. Eqn. (3.3) is considered in this work for computation of VUFs at the distribution buses.

The specific limits and recommendations for voltage unbalance vary depending on the specific application, equipment, and region. For example, IEEE provides guidance on voltage unbalance in its standard IEEE 519-2014. This standard recommends a voltage unbalance limit of 2.5% for distribution systems [?]. The National Electrical Code (NEC), developed by the National Fire Protection Association (NFPA), sets requirements for voltage unbalance in Article 210.4(B) and 450.3(B). The NEC specifies a maximum voltage unbalance of 5% for individual branch circuits and recommends a maximum of 2% for three-phase systems [? ?]. Other organizations that provide guidance on voltage unbalance include the International Electrotechnical Commission (IEC) (2.5%) [?], the American National Standards Institute (ANSI) (provides guidance on voltage unbalance in electrical power systems, however, it does not specify a specific limit for voltage unbalance) [?], and the Canadian Standards Association (CSA) (5%) [?].

3.2 Perturb & observe based unbalanced voltage correction

In this proposed method the negative sequence current injected into the microgrid by an FLIG is generated by the superposition of two orthogonal negative sequence current components $i_{inphase}$ and $i_{quadphase}$. This is given in eqn. (3.4).

$$i_{FLIG}{}^{abc-} = \begin{bmatrix} i_{FLIG}{}^{a-} \\ i_{FLIG}{}^{b-} \\ i_{FLIG}{}^{c-} \end{bmatrix} = \begin{bmatrix} i_{inphase}{}^{a-}\angle(\theta^-) \\ i_{inphase}{}^{b-}\angle(\theta^- + 2\pi/3) \\ i_{inphase}{}^{c-}\angle(\theta^- - 2\pi/3) \end{bmatrix} + \begin{bmatrix} i_{quadphase}{}^{a-}\angle(\theta^- - \pi/2) \\ i_{quadphase}{}^{b-}\angle(\theta^- + 2\pi/3 - \pi/2) \\ i_{quadphase}{}^{c-}\angle(\theta^- - 2\pi/3 - \pi/2) \end{bmatrix} \tag{3.4}$$

The objective is to vary $i_{inphase}$ and $i_{quadphase}$ such that the FLIG's negative sequence current, $I_{FLIG}{}^-$ becomes equal to the negative sequence load current, I_l^-. From the negative sequence equivalent network shown in Fig. 2.6 it can be seen that this will result in $I_g^- = 0$ and consequently $V_A^- = 0$. The phasor diagram for the proposed method is shown in Fig. 3.1. As voltage unbalance factor computation does not take the zero-sequence component into consideration the zero-sequence current is not controlled and hence set to zero.

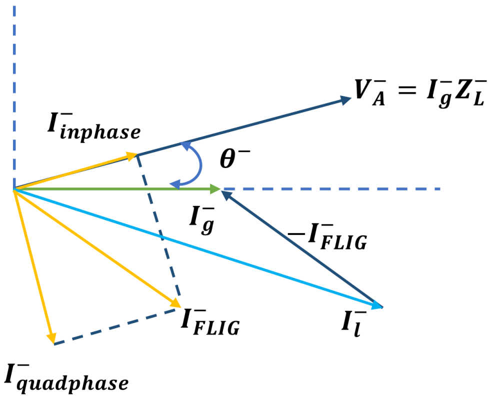

Fig. 3.1 Phasor diagram for the negative sequence network with $i_{inphase}$ and $i_{quadphase}$.

3.2.1 Algorithm for unbalanced voltage correction using Perturb & Observe method

The algorithm for the developed perturb and observe method for unbalanced voltage correction is as follows.

Step 1: To begin the correction, initially $i_{inphase}$ and $i_{quadphase}$ are set to zero and the corresponding VUF at the FLIG-connected bus is observed.

Step 2: The two orthogonal current components $i_{inphase}$ and $i_{quadphase}$ are then perturbed sequentially in four directions, ($i_{inphase} + inc$, $i_{quadphase}$), ($i_{inphase} - inc$, $i_{quadphase}$), ($i_{inphase}$, $i_{quadphase} + inc$), ($i_{inphase}$, $i_{quadphase} - inc$) with, ($i_{inphase}$, $i_{quadphase}$) as the origin and the resulting VUF observed after each perturbation.

Here *inc* is the perturbation given in each direction. This is depicted in Fig. 3.2.

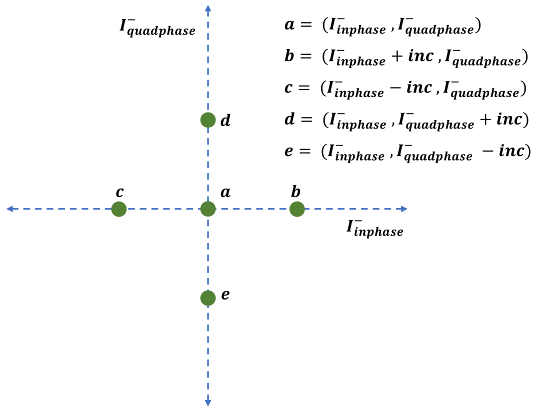

Fig. 3.2 Perturbations given to $i_{inphase}$ and $i_{quadphase}$

Step 3: Out of the five pairs, the one which yields the minimum VUF is now considered the new origin. In Fig. 3.2 let c be the coordinate at which minimum VUF is obtained after the first perturbation. Therefore, c is now considered as the new origin.

Step 4: Now from this new origin, $i_{inphase}$ and $i_{quadphase}$ are perturbed again in four orthogonal directions and the resulting VUFs are observed. This second perturbation and observation is depicted in Fig. 3.3.

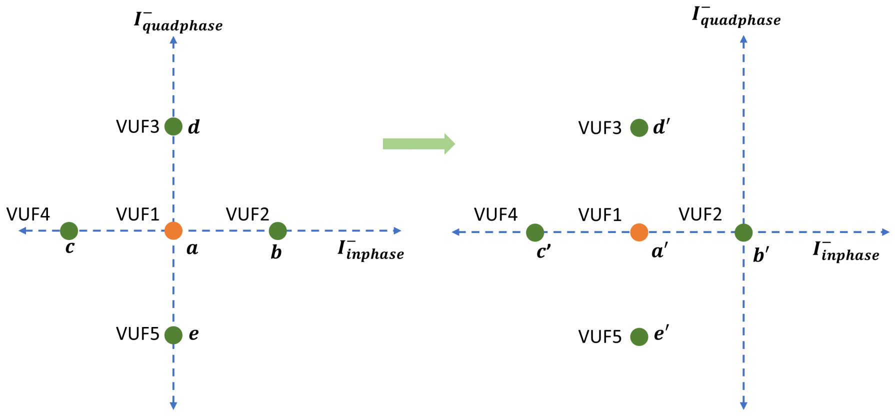

Fig. 3.3 Shift of origin after first iteration of perturbation and observation

Step 5: The perturbation and observation (Step 2 to 4) are repeated until minimum VUF is observed at the FLIG-connected bus. For a given state of the microgrid minimum VUF at the FLIG-connected bus is observed for a certain value of $i_{inphase}$ and $i_{quadphase}$.

The flowchart for the developed method is shown in Fig. 3.4

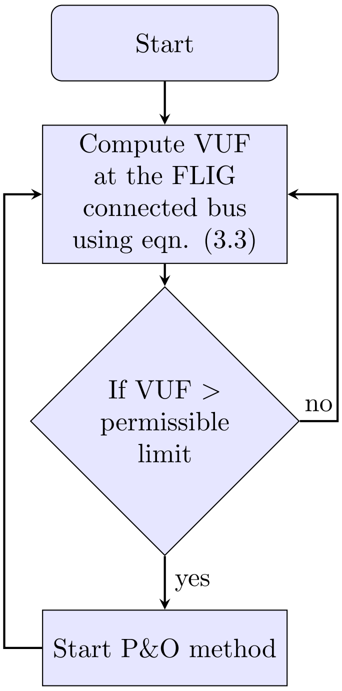

(a) Flowchart for enabling voltage unbalance correction

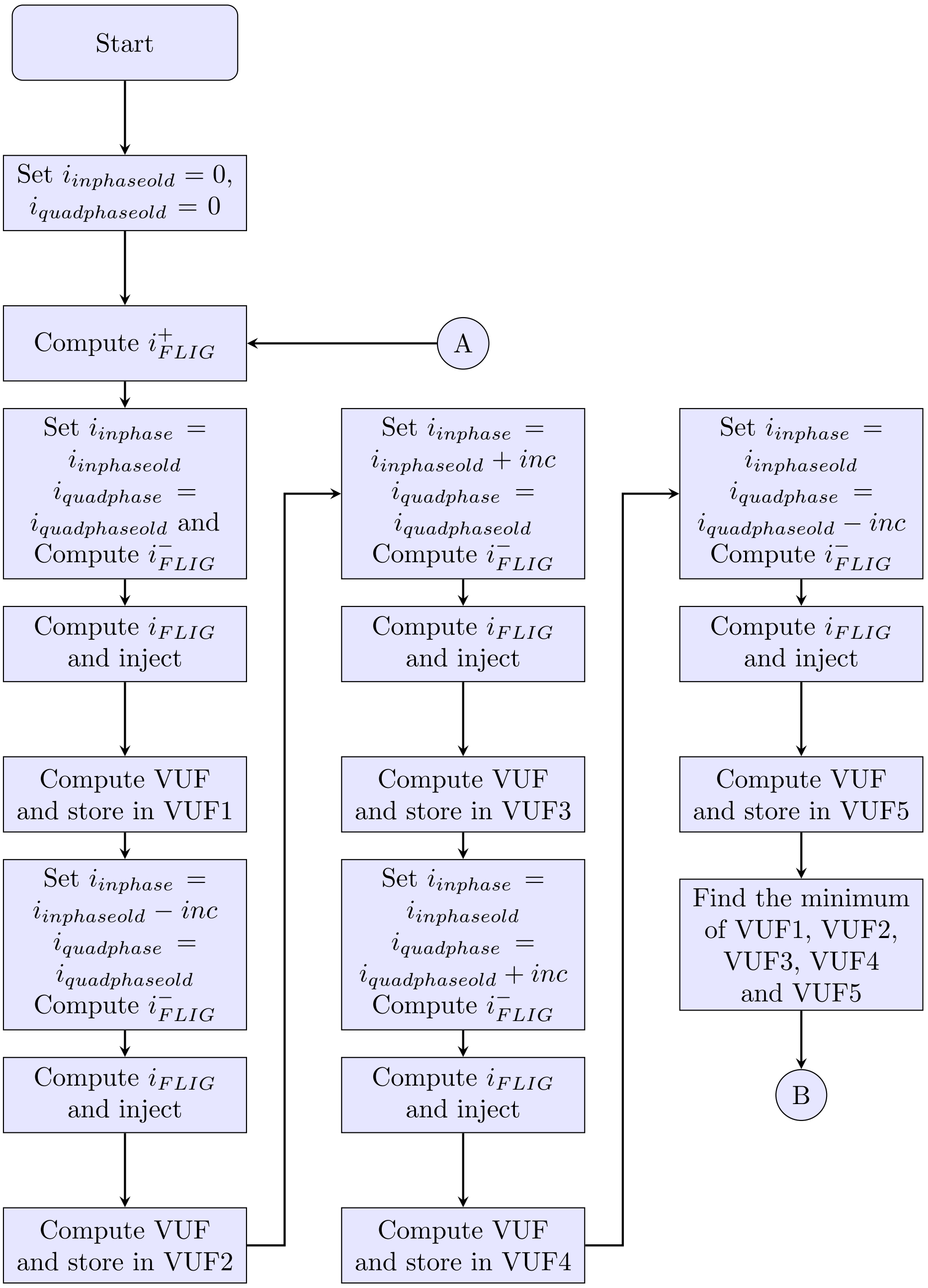

(b) Flowchart for determining VUFs for all five pairs of $i_{inphase}$ and $i_{quadphase}$

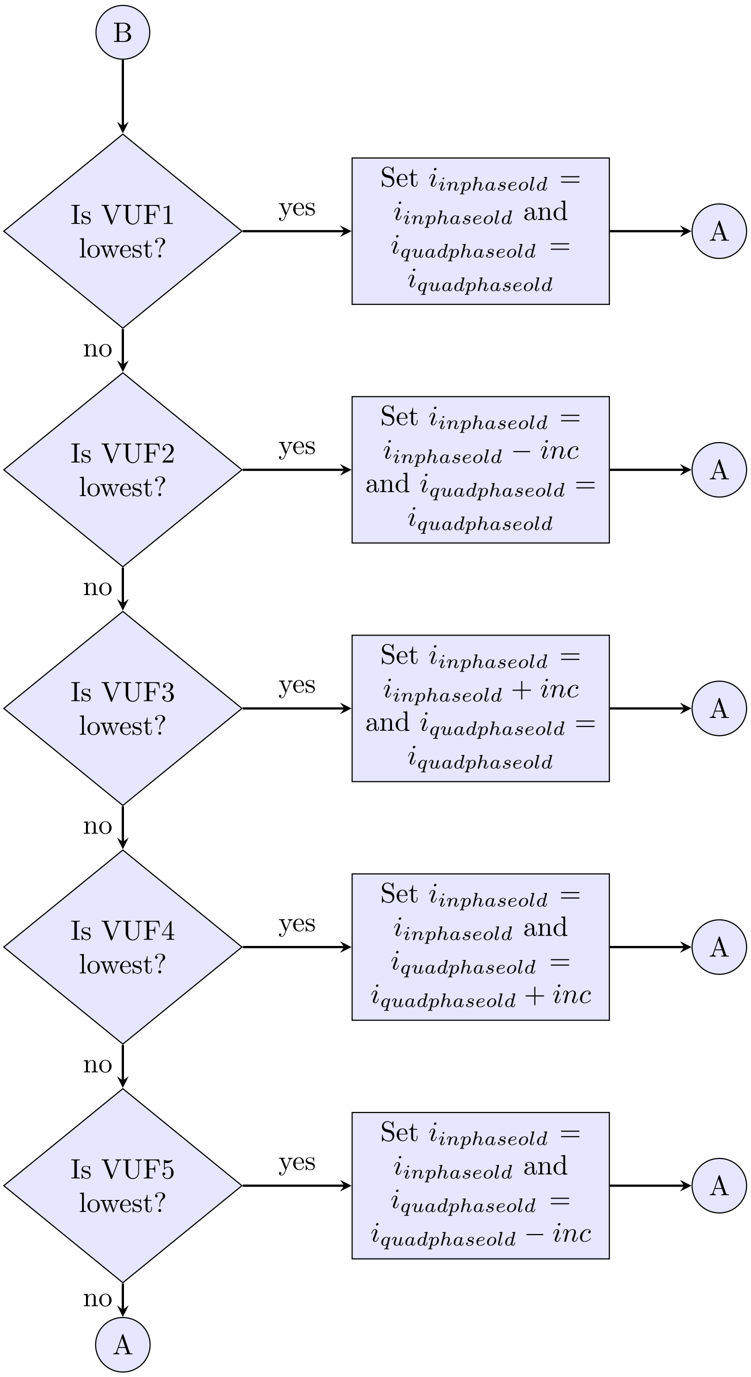

(c) Flowchart for determining the minimum VUFs of all five of $i_{inphase}$ and $i_{quadphase}$ pairs

Fig. 3.4 Flowchart of the proposed P&O method

3.3 Modified backward-forward sweep based unbalanced load flow algorithm

In order to investigate and validate the working of the proposed P&O method for unbalance voltage mitigation in microgrids with unbalanced loading, an unbalanced load flow method based on the backward-forward sweep technique proposed in [**?**] is employed in this work. The basic backward-forward sweep based algorithm is explained in Sec. (A.2). However, the method is modified to include the injection of negative sequence current and calculation of voltage unbalance factor. Fig. 3.5 displays a section of an unbalanced radial four-wire microgrid with n buses, where the FLIG is connected to bus-q. The algorithm for implementing the modified backward-forward sweep-based unbalanced load flow analysis with negative sequence current injection is as follows:

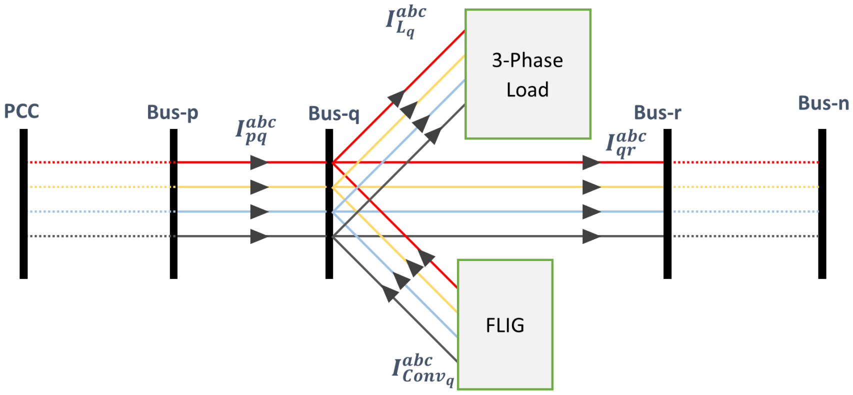

Fig. 3.5 Section of an unbalanced radial low-voltage microgrid with FLIG.

Step 1: Input line data (which includes line impedance and line charging) and load data.

Step 2: Initialize voltage at each bus to the nominal value.

Step 3: Set iteration count to zero and allowable maximum iteration.

Step 4: Calculate load current, ${\mathbf{I}_{L_q}}^{abc}$ at each bus using eqn. (3.5) for star-connected loads or eqn.(3.6) for delta connected loads.

$$\begin{bmatrix} I_{L_q}^a \\ I_{L_q}^b \\ I_{L_q}^c \end{bmatrix} = \begin{bmatrix} \left(\frac{S_{L_q}^a}{V_q^a}\right)^* \\ \left(\frac{S_{L_q}^b}{V_q^b}\right)^* \\ \left(\frac{S_{L_q}^c}{V_q^c}\right)^* \end{bmatrix} \tag{3.5}$$

$$\begin{bmatrix} I_{L_q}^a \\ I_{L_q}^b \\ I_{L_q}^c \end{bmatrix} = \begin{bmatrix} \left(\frac{S_{L_q}^{ab}}{V_q^{ab}}\right)^* - \left(\frac{S_{L_q}^{ca}}{V_q^{ca}}\right)^* \\ \left(\frac{S_{L_q}^{bc}}{V_q^{bc}}\right)^* - \left(\frac{S_{L_q}^{ab}}{V_q^{ab}}\right)^* \\ \left(\frac{S_{L_q}^{ca}}{V_q^{ca}}\right)^* - \left(\frac{S_{L_q}^{bc}}{V_q^{bc}}\right)^* \end{bmatrix} \tag{3.6}$$

Where $S_{L_q} = P_{L_q} + jQ_{L_q}$ is the complex power of load at bus q. Three different types of loads i.e. constant power, constant current, and constant impedance loads has been considered in this work. Detailed modelling for the three types of loads are explained in Sec. (A.1)

Step 5: Calculate the line charging current, $\mathbf{I}_{sh_{pq}}^{abc}$ at bus-q for the line between bus-p and bus-q using eqn. (3.7)

$$[\mathbf{I}_{sh_{pq}}^{abc}] = \frac{1}{2}[\mathbf{Y}_{sh_{pq}}][\mathbf{V}_q^{abc}] \tag{3.7}$$

Where, $\mathbf{Y}_{sh_{pq}}$ is the shunt admittance matrix of the line between bus-p and bus-q given by eqn. (3.8)

$$\mathbf{Y}_{sh_{pq}} = \begin{bmatrix} -\left(y_{pq}^{aa} + y_{pq}^{ab} + y_{pq}^{ac}\right) & y_{pq}^{ab} & y_{pq}^{ac} \\ y_{pq}^{ba} & -\left(y_{pq}^{ba} + y_{pq}^{bb} + y_{pq}^{bc}\right) & y_{pq}^{bc} \\ y_{pq}^{ca} & y_{pq}^{cb} & -\left(y_{pq}^{ca} + y_{pq}^{cb} + y_{pq}^{cc}\right) \end{bmatrix} \tag{3.8}$$

Step 6: Calculate the total line charging current, $\mathbf{I}_{sh_q}^{abc}$ at bus-q using eqn. (3.9)

$$\begin{bmatrix} {I_{sh_q}}^a \\ {I_{sh_q}}^b \\ {I_{sh_q}}^c \end{bmatrix} = \begin{bmatrix} \sum\limits_{qm=1}^{M} {I_{sh_{qm}}}^a \\ \sum\limits_{qm=1}^{M} {I_{sh_{qm}}}^b \\ \sum\limits_{qm=1}^{M} {I_{sh_{qm}}}^c \end{bmatrix} \tag{3.9}$$

Where, qm is a line directly connected to bus-q and M is the total number of such lines.

Step 7: Calculate the negative sequence current injected into the microgrid for unbalanced voltage correction by an FLIG at a bus q using eqn. (3.10).

$$\mathbf{i}_{FLIG}{}^{abc-} = \begin{bmatrix} i_{FLIG}{}^{a-} \\ i_{FLIG}{}^{b-} \\ i_{FLIG}{}^{c-} \end{bmatrix} = \begin{bmatrix} i_{inphase}{}^{a-}\angle(\theta^-) \\ i_{inphase}{}^{b-}\angle(\theta^- + 2\pi/3) \\ i_{inphase}{}^{c-}\angle(\theta^- - 2\pi/3) \end{bmatrix} + \begin{bmatrix} i_{quadphase}{}^{a-}\angle(\theta^- - \pi/2) \\ i_{quadphase}{}^{b-}\angle(\theta^- + 2\pi/3 - \pi/2) \\ i_{quadphase}{}^{c-}\angle(\theta^- - 2\pi/3 - \pi/2) \end{bmatrix} \tag{3.10}$$

Step 8: Calculate the positive sequence current injected into the microgrid by an FLIG at bus q using eqn. (3.11)

$$\begin{bmatrix} I_{FLIG_q}{}^{a+} \\ I_{FLIG_q}{}^{b+} \\ I_{FLIG_q}{}^{c+} \end{bmatrix} = \begin{bmatrix} \left(\frac{S_{DG_q}{}^{a}/3}{V_q^{a+}}\right)^* \\ \left(\frac{S_{DG_q}{}^{b}/3}{V_q^{b+}}\right)^* \\ \left(\frac{S_{DG_q}{}^{c}/3}{V_q^{c+}}\right)^* \end{bmatrix} \tag{3.11}$$

Where, $S_{DG_q} = P_{DG_q} + jQ_{DG_q}$ is the total positive sequence complex power injected by the FLIG into bus q.

Step 9: Calculate the total current injected by an FLIG into bus q using eqn. (3.12).

$$\begin{bmatrix} I_{FLIG_q}{}^{a} \\ I_{FLIG_q}{}^{b} \\ I_{FLIG_q}{}^{c} \end{bmatrix} = \begin{bmatrix} I_{FLIG_q}{}^{a+} \\ I_{FLIG_q}{}^{b+} \\ I_{FLIG_q}{}^{c+} \end{bmatrix} + \begin{bmatrix} I_{FLIG_q}{}^{a-} \\ I_{FLIG_q}{}^{b-} \\ I_{FLIG_q}{}^{c-} \end{bmatrix} + \begin{bmatrix} I_{FLIG_q}{}^{a0} \\ I_{FLIG_q}{}^{b0} \\ I_{FLIG_q}{}^{c0} \end{bmatrix} \tag{3.12}$$

In this work the zero sequence current are all set to zero.

Step 10: Calculate the total current at bus q using eqn. (3.13). If no FLIG is connected to a bus set the I_{FLIG} current to zero.

$$\begin{bmatrix} I_q^a \\ I_q^b \\ I_q^c \end{bmatrix} = \begin{bmatrix} I_{L_q}{}^{a} \\ I_{L_q}{}^{b} \\ I_{L_q}{}^{c} \end{bmatrix} + \begin{bmatrix} I_{sh_q}{}^{a} \\ I_{sh_q}{}^{b} \\ I_{sh_q}{}^{c} \end{bmatrix} - \begin{bmatrix} I_{FLIG_q}{}^{a} \\ I_{FLIG_q}{}^{b} \\ I_{FLIG_q}{}^{c} \end{bmatrix} \tag{3.13}$$

Step 11: (Backward Sweep) Starting from the radial network's last bus, calculate all the line currents upstream till slack bus using eqn. (3.14). The PCC bus serves as slack bus during grid connected mode and during islanded mode the grid-forming generator with highest capacity serves as the slack bus.

$$[\mathbf{I}_{pq}]^{abc} = [\mathbf{I}_q^{abc}] + \sum_{lm=1}^{M} [\mathbf{I}_{lm}^{abc}] \tag{3.14}$$

Where, lm is a line connected to bus q downstream and M is the total number of such lines.

Step 12: (Forward Sweep) Starting from the slack bus and moving towards the last bus of the radial network, update the voltages of all the buses downstream using eqn. (3.15)

$$[\mathbf{V}_q^{abc}] = [\mathbf{V}_p^{abc}] - [\mathbf{Z}][\mathbf{I}_{pq}^{abc}] \tag{3.15}$$

Where, Z is the impedance matrix of the line between bus-p and bus-q given by eqn. (3.16)

$$\mathbf{Z} = \begin{bmatrix} z_{pq}^{aa,n} & z_{pq}^{ab,n} & z_{pq}^{ac,n} \\ z_{pq}^{ba,n} & z_{pq}^{bb,n} & z_{pq}^{bc,n} \\ z_{pq}^{ca,n} & z_{pq}^{cb,n} & z_{pq}^{cc,n} \end{bmatrix} \tag{3.16}$$

Step 13: Compute the maximum error of voltage for all the buses during two successive iterations (i.e. the absolute value of voltage difference between the present and previous iteration for all buses). If the maximum error is greater than the set convergence criteria or if the number of iterations is less that the set maximum limit repeat steps 4 to 13. else goto step 14, provided that the load flow analysis converges. If the load flow iteration is terminated due to violation of maximum iteration limit terminate the load flow with warning message, "Load flow did not converge" and goto step 19.

Step 14: Calculate the VUFs at each bus using eqn. (3.3).

Step 15: Calculate the real power and reactive power loss in phases a, b and c in each line T_{pq} by using eqns. (3.17) through (3.22).

$$P_{L_{pq}}^{a} = \Re\Big\{V_p^a(I_{pq}^a)^* - V_q^a(I_{qp}^a)^*\Big\} \tag{3.17}$$

$$P_{L_{pq}}^{b} = \Re\Big\{V_p^b(I_{pq}^b)^* - V_q^b(I_{qp}^b)^*\Big\} \tag{3.18}$$

$$P_{L_{pq}}^{c} = \Re\Big\{V_p^c(I_{pq}^c)^* - V_q^c(I_{qp}^c)^*\Big\} \tag{3.19}$$

$$Q_{L_{pq}}^{a} = \Im\Big\{V_p^a(I_{pq}^a)^* - V_q^a(I_{qp}^a)^*\Big\} \tag{3.20}$$

$$Q_{L_{pq}}^{b} = \Im\Big\{V_p^b(I_{pq}^b)^* - V_q^b(I_{qp}^b)^*\Big\} \tag{3.21}$$

$$Q_{L_{pq}}^{c} = \Im\Big\{V_p^c(I_{pq}^c)^* - V_q^c(I_{qp}^c)^*\Big\} \tag{3.22}$$

Where, $\Re$ is the real part and $\Im$ is the imaginary part of the complex power.

Step 16: Calculate the total real power and reactive power loss in each line T_{pq} by eqns. (3.23) and (3.24), respectively.

$$P_{L_{pq}} = P_{L_{pq}}^{a} + P_{L_{pq}}^{b} + P_{L_{pq}}^{c} \tag{3.23}$$

$$Q_{L_{pq}} = Q_{L_{pq}}^{a} + Q_{L_{pq}}^{b} + Q_{L_{pq}}^{c} \tag{3.24}$$

Step 17: Calculate the total real power and reactive power loss of the system using eqns. (3.25) and (3.26), respectively.

$$P_{Loss} = \sum P_{L_{pq}} \tag{3.25}$$

$$Q_{Loss} = \sum Q_{L_{pq}} \tag{3.26}$$

Step 18: Report results.

Step 19: Stop.

3.4 Algorithm for finding the minimum VUF in radial distribution systems

The following steps outline the algorithm for determining the minimum VUF using the proposed P&O method in a radial distribution system, incorporating the modified backward-forward sweep-based unbalanced load flow analysis:

Step 1: Select the FLIG bus.

Step 2: Set the value of perturbation *inc*.

Step 3: Assign the value of distributed generation in the FLIG bus.

Step 4: Set $i_{inphaseold} = 0$ and $i_{quadphaseold} = 0$ for the FLIG bus.

Step 5: Set $i_{inphase1} = i_{inphaseold}$ and $i_{quadphase1} = i_{quadphaseold}$ for the FLIG bus.

Step 6: Run the modified load flow discussed in Sec. (3.3) and store the value of VUF at the FLIG connected bus in VUF1 and minVUForigin.

Step 7: Set $i_{inphase2} = i_{inphaseold} + inc$ and $i_{quadphase2} = i_{quadphaseold}$ for the FLIG bus.

Step 8: Run the modified load flow and store the value of VUF at the FLIG connected bus in VUF2.

Step 9: Set $i_{inphase3} = i_{inphaseold}$ and $i_{quadphase3} = i_{quadphaseold} + inc$ for the FLIG bus.

Step 10: Run the modified load flow and store the value of VUF at the FLIG connected bus in VUF3.

Step 11: Set $i_{inphase4} = i_{inphaseold} - inc$ and $i_{quadphase4} = i_{quadphaseold}$ for the FLIG bus.

Step 12: Run the modified load flow and store the value of VUF at the FLIG connected bus in VUF4.

Step 13: Set $i_{inphase5} = i_{inphaseold}$ and $i_{quadphase5} = i_{quadphaseold} - inc$ for the FLIG bus.

Step 14: Run the modified load flow and store the value of VUF at the FLIG connected bus in VUF5.

Step 15: Find the minimum of VUF1, VUF2, VUF3, VUF4 and VUF5 and store in minVUFcurrent.

Step 16: Shift the origin to the new minimum position.

- If VUF1 is lowest set $i_{inphaseold} = i_{inphase1}$ and $i_{inphaseold} = i_{quadphase1}$
- Else if VUF2 is lowest set $i_{inphaseold} = i_{inphase2}$ and $i_{quadphaseold} = i_{quadphase2}$
- Else if VUF3 is lowest set $i_{inphaseold} = i_{inphase3}$ and $i_{quadphaseold} = i_{quadphase3}$
- Else if VUF4 is lowest set $i_{inphaseold} = i_{inphase4}$ and $i_{quadphaseold} = i_{quadphase4}$
- Else if VUF5 is lowest set $i_{inphaseold} = i_{inphase5}$ and $i_{quadphaseold} = i_{quadphase5}$

Step 17: If minVUFcurrent is less that minVUForigin, set minVUForigin = minVUFcurrent and run steps 5 to 17 else goto step 18.

Step 18: Report the results.

Step 19: Stop.

3.5 Simulation Results and Analysis

Four unbalanced radial distribution systems (URDS) are used as microgrids to test the proposed method. Some common assumptions are made for the implementation of the proposed approach.

- Frequency is assumed to be constant.
- Bus 1 is considered as PCC and acts as the slack bus in grid connected mode of operation.
- Only three phase buses are considered for installation of FLIGs.
- Only one FLIG can be installed on one bus.
- No FLIG can be installed in the PCC bus.
- The FLIGs are modeled as negative PQ load.
- The FLIGs are capable of injecting negative sequence currents.

3.5.1 Case Study I: 25-bus system

The first test system is a 4.16 kV, 25-bus URDS, as depicted in Fig. A.2. The line and load data are given in Table. A.1 [**?**]. The base case load flow results is provided in Table. A.3. Although unbalanced, it has been observed that the system's VUF is insignificant for the base case load values given in Table. A.1. Therefore, the complex loads are increased three times in phase a and twice in phase b in all buses in order to increase the voltage unbalance of the system. The system's voltage profile is now significantly out of balance as a result of this. The VUFs in the following case studies are computed for the modified 25-bus URDS.

Test for convexity

According to the proposed P&O method, there should be a unique pair of ($i_{inphase}$, $i_{quadphase}$) for which the VUF is minimum; that is, if the values for ($i_{inphase}, i_{quadphase}$) are swept between an positive upper and a negative lower limit, the surface plot of VUF vs ($i_{inphase}$, $i_{quadphase}$) must be convex. To test for this convexity, the 25-bus URDS is used as a microgrid. Bus-1 serves as the slack bus. An FLIG is connected at bus 13 (randomly selected). The FLIG is initially set up to provide only negative sequence current and no positive or zero sequence current. The modified unbalanced load flow method discussed in Sec. (3.3) is performed on the modified 25-bus URDS, with the values of $i_{i_{inphase}}$ and $i_{quadphase}$ swept from -0.05 p.u. to 0.05 p.u. in 0.0005 p.u. increments, and the corresponding VUF computed for each pair of $i_{inphase}$ and $i_{quadphase}$. The surface plot of VUF vs ($i_{inphase}$, $i_{quadphase}$) obtained is shown in Fig. 3.6. It can be seen from the surface plot that the surface obtained is convex, which implies that there is a unique value of ($i_{inphase}, i_{quadphase}$) at which the VUF obtained is minimum.

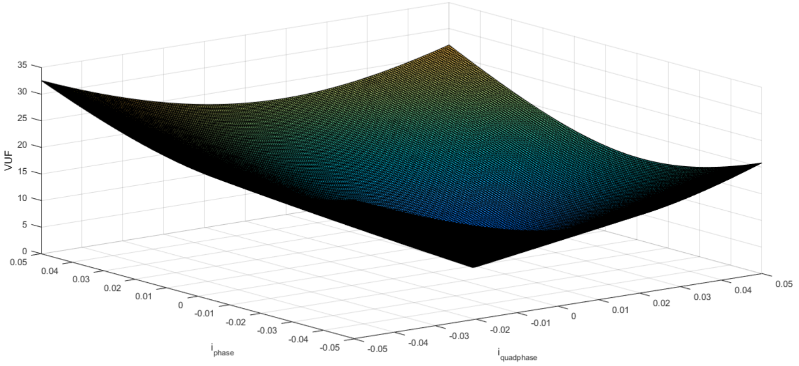

Fig. 3.6 Surface plot of VUF w.r.t $i_{inphase}$ and $i_{quadphase}$ with FLIG at bus-13

The FLIG is then connected at bus-16 (randomly selected) and the process is repeated. The results obtained is shown in Fig. 3.7. In this case too the surface obtained is convex, which implies that for this bus too there is a unique value of ($i_{inphase}$, $i_{quadphase}$) at which the VUF obtained is minimum.

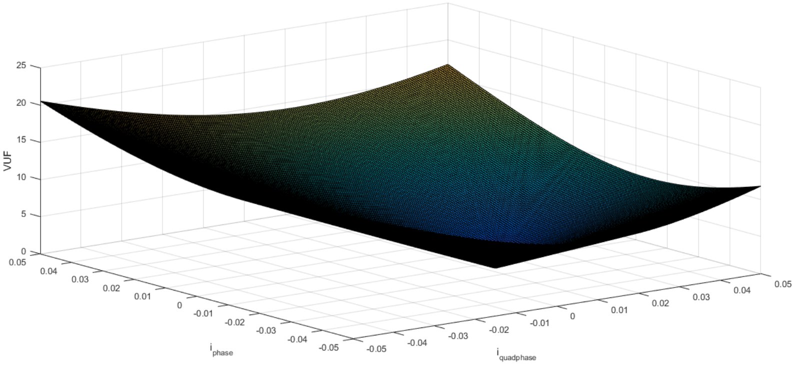

Fig. 3.7 Surface plot of VUF w.r.t $i_{inphase}$ and $i_{quadphase}$ with FLIG at bus-16.

It is thus possible to exploit the surface's convexity and generate negative sequence currents to trace the shortest trajectory to the surface's minima, thereby maintaining a minimum VUF. In the following case studies, the algorithm discussed in Sec. (3.4) is used to determine the minimum VUFs at FLIG connected buses.

Negative sequence current injection on a single bus

The Bus-1 acts as the slack bus in the system. Six studies are conducted: Case 1: no FLIG is attached, Case 2: one FLIG is connected at bus 25, Case 3: one FLIG is connected at bus 20, Case 4: one FLIG is connected at bus 15, Case 5: one FLIG is connected at bus 10, and Case 6: one FLIG is connected at bus 5. The buses used in the case studies are chosen at random. Positive and zero sequence current injection are both set to zero. The proposed algorithm is then used to inject and control negative sequence current. After the minimum VUF is reached, the VUF at all buses for each case is computed.

Fig. 3.8 shows the VUF computed for all the buses in the six cases. The outcomes reveal that the proposed approach has considerably decreased the VUF at all the buses in the system, with the greatest reduction being observed at the bus where the FLIG is connected. In comparison to case 1 where no FLIG is connected, in case 2 where a FLIG is connected to bus-25, VUF at this specific bus decreases from 3.75% to 0. The next most significant VUF reduction is observed at the bus closest to bus-25, i.e., bus-24, with a decrease of 73%. However, the VUF at bus-12, the farthest from the FLIG, decreases by only 14%. When a FLIG is connected to bus-20 in case 3, the VUF there falls from 3.69% to 0 when compared to case 1. The buses that are closest to bus 20 i.e., buses 18 and 19 have the next-largest VUF reductions of 75% and 97% respectively. The VUF at bus-13, the farthest from the FLIG, decreases by 21%. Therefore, the degree of VUF correction at a specific bus depends on its distance from the FLIG, with closer buses exhibiting higher levels of correction. Similar findings are noted when the FLIG is attached to buses 15, 10, and 5. It is also observed that a single FLIG cannot achieve sufficient VUF attenuation in all the buses, highlighting the need for the installation of multiple FLIGs in the system.

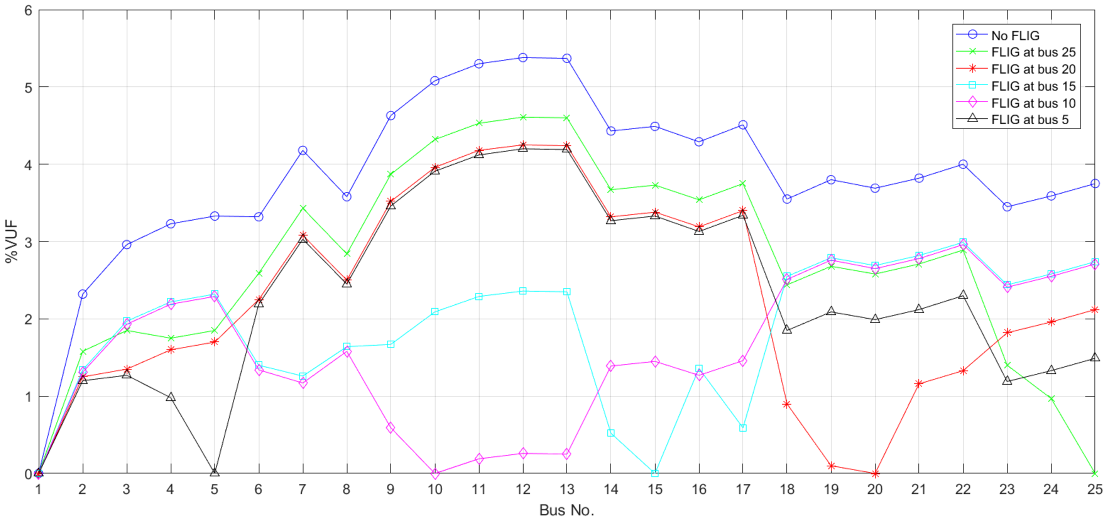

Fig. 3.8 Variation of VUF in a 25-bus URDS with a single FLIG connected under the injection of only negative sequence current.

Negative sequence current injection on two buses

The Bus-1 acts as the slack bus in the system. Six studies are conducted: Case 1: no FLIG is attached, Case 2: two FLIGs are placed at bus 25 and 20, Case 3: two FLIGs are placed at bus 21 and 13, Case 4: two FLIGs are placed at bus 17 and 11, Case 5: two FLIGs are placed at bus 12 and 6, and Case 6: two FLIGs are placed at bus 7 and 23. The buses used in the case studies are chosen at random. Both the positive and zero sequence current injection are set to zero, following which the proposed algorithm is utilized to inject and regulate the negative sequence current. Once the minimum VUFs at the FLIG connected buses is achieved, the VUFs are calculated for all buses in each case.

Fig. 3.9 illustrates the VUF results obtained for all buses in the six cases. When FLIGs are connected to buses 25 and 20 in case 2, the VUFs decrease to 0 from 3.75 and 3.69, respectively. Furthermore, the bus closest to bus-25, i.e. bus-24, experiences the next significant reduction of 84%. Similarly, the buses closest to bus-20, i.e. buses 18 and 19, experience reductions of 81% and 97%, respectively. Similarly, in case 3, when FLIGs are connected to buses 21 and 13, the VUF decreases to 0 from 3.82% and 5.37%, respectively. Furthermore, the buses closest to bus-21, i.e., buses 22 and 18, experience reductions of 96% and 75%, respectively, while the bus closest to bus-13, i.e., bus-11, experiences a reduction of 91%. From Fig. 3.8 and Fig. 3.9 it can be seen that compared to the scenarios where negative sequence current is injected in a single bus, the reduction in VUF in the buses is significantly higher in situations where negative sequence current is injected in two buses. The other cases also reveal similar results.

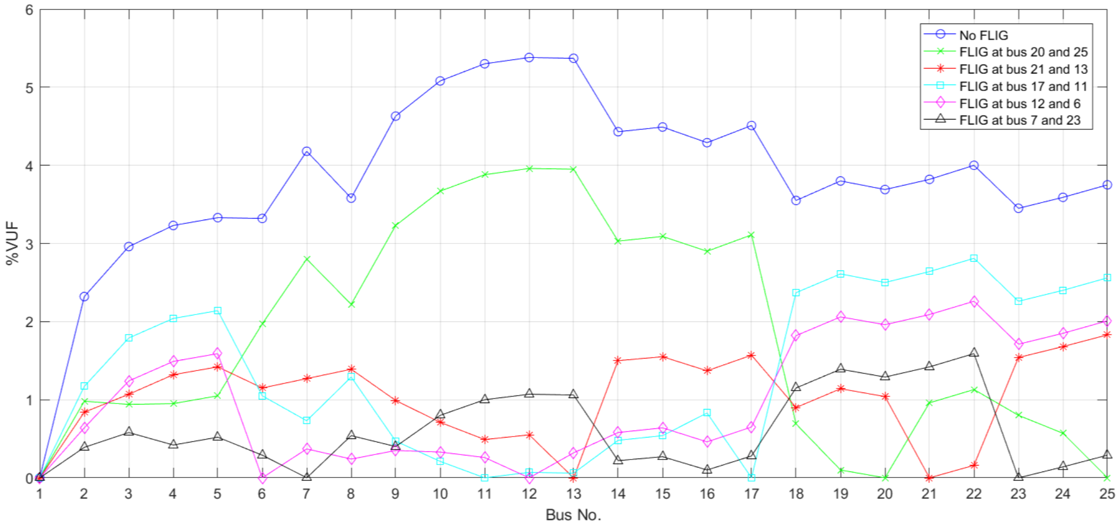

Fig. 3.9 Variation of VUF in a 25-bus URDS with a two FLIGs connected under the injection of only negative sequence current.

Positive sequence current injection on a single bus

Considering that the primary objective of a grid-connected inverter is to supply real power to the loads, injection of positive sequence current is of paramount significance. To investigate the impact of positive sequence current injection on VUF reduction, five separate case studies are conducted, each involving the installation of an FLIG at bus 25, 20, 15, 10, and 5, with bus-1 serving as the slack bus. The buses used in the case studies are chosen at random. Throughout the simulations, zero sequence and negative sequence current injection are maintained at zero, while eqn. (3.11) is employed to calculate the positive sequence current. To set the DG size in eqn. (3.11), unbalanced load flow is carried out iteratively, with incremental increases in DG size, to identify the optimal DG size at which real power loss is minimum. In eqn. (3.11) the DG sizes are then set to 80% of the determined values.

Fig. 3.10 illustrates the VUF results obtained. In Case 1, connecting an FLIG at bus-25 results in a decrease of VUF from 3.75% to 3.29%, which is only a 12% reduction. Similarly, in Case 2, when the FLIG is connected at bus-20, VUF decreases from 3.69% to 3.13%, which is only a 15% reduction. Similar results are obtained in the remaining cases. Therefore, the results indicate that injecting positive sequence current alone does not have a significant impact on correcting voltage unbalance.

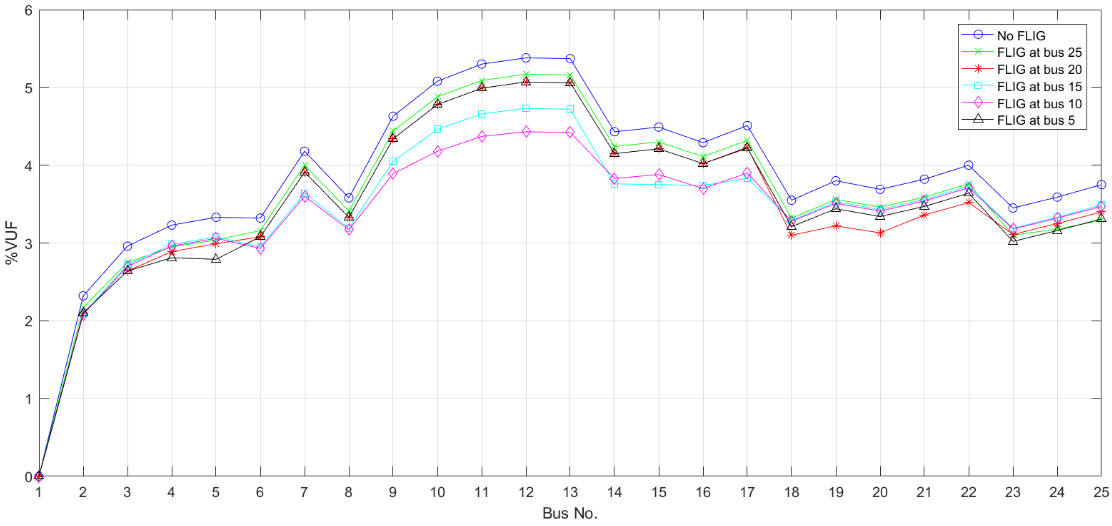

Fig. 3.10 Variation of VUF in a 25-bus URDS with a single FLIG connected under the injection of only positive sequence current.

Positive and negative sequence current injection on a single bus

The next phase of the study focuses on investigating the joint impact of positive and negative sequence current injection on reducing VUF. Five case studies are conducted, with an FLIG placed individually at bus 25, 20, 15, 10, and 5. The buses used in the case studies are chosen at random. The slack bus for all cases is bus-1. Zero sequence current injection is kept at zero. Eqn. (3.11) is utilized to compute the positive sequence current, whereas the proposed algorithm is utilized to control and inject negative sequence current.

Fig. 3.11 depicts the VUF values at all buses in the system, considering the injection of both positive and negative sequence currents. Fig. 3.12 presents a comparison of the results obtained by injecting only positive sequence current, only negative sequence current, and both positive and negative sequence currents at bus-25. The obtained results indicate that, for every bus, the reduction in VUF percentage is most significant when both positive and negative sequence currents are injected, as compared to when only positive or negative sequence currents are considered.

3.5.2 Case Study II: IEEE 13-bus system

The second test system is the standard 4.16 kV, IEEE 13-bus URDS, as depicted in Fig. A.3. The line and load data are given in Table. A.5 [?]. The base case load flow results is provided in Table. A.11. This test system comprises of single-phase and two-phase buses along with three-phase buses. Also there are constant power, constant current and constant impedance star and delta connected spot and distributed loads. Voltage regulators and capacitors are neglected when evaluating the performance under

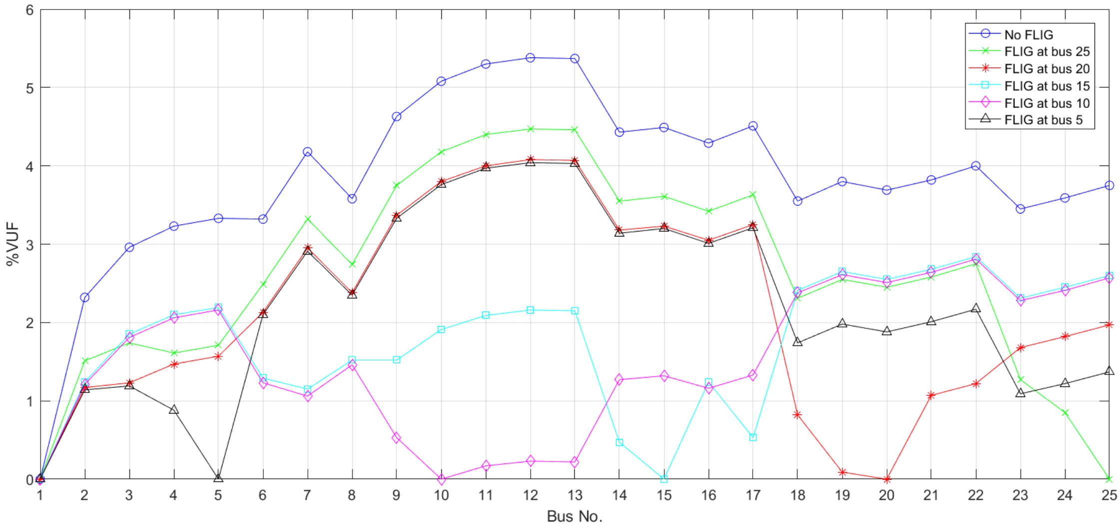

Fig. 3.11 Variation of VUF in a 25-bus URDS with a single FLIG connected under the injection of both positive and negative sequence current.

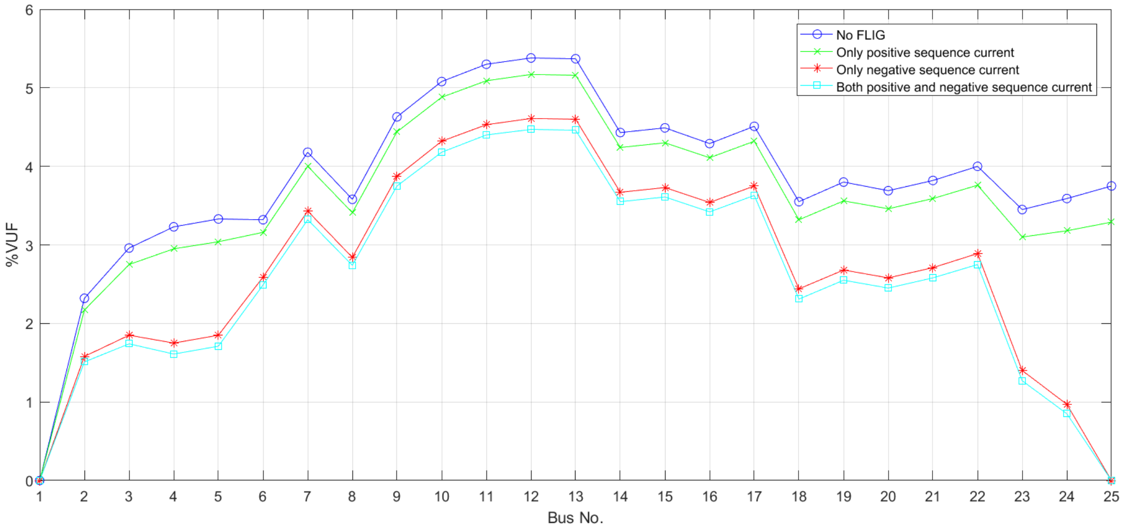

Fig. 3.12 Comparision of VUF in a 25-bus URDS with a single FLIG connected at bus-25.

unbalanced conditions. In this system, buses 1, 2, 5, 6, 7, 11, 12, and 13 are three-phase buses, while the remaining buses are either two-phase or single-phase. Buses 7 and 12 are connected by a switch, hence the results obtained for both of these buses with the switch closed are identical. As FLIGs can only be integrated into three-phase buses, their placements as well as VUF computations are also restricted to these buses.

Bus-1 serves as the slack bus. Three simulations are conducted: Case 1 with no FLIG attached, Case 2 with one FLIG connected at bus 13, and Case 3 with one FLIG connected at bus 7. The buses used in the case studies are chosen at random. Both positive and zero sequence current injections are set to zero, while the proposed algorithm is utilized to control and inject negative sequence current. The VUFs are computed for all three phase buses in each case after reaching the minimum VUF. Fig. 3.13 displays the VUFs for all three phase buses. The findings indicate that, compared to case 1 where no unbalance correction is implemented, in case 2 and case 3 when an FLIG is connected at bus 13 and bus 7, the proposed technique significantly reduces the VUF at all the buses, with the most substantial decrease observed at the buses where the FLIGs are attached.

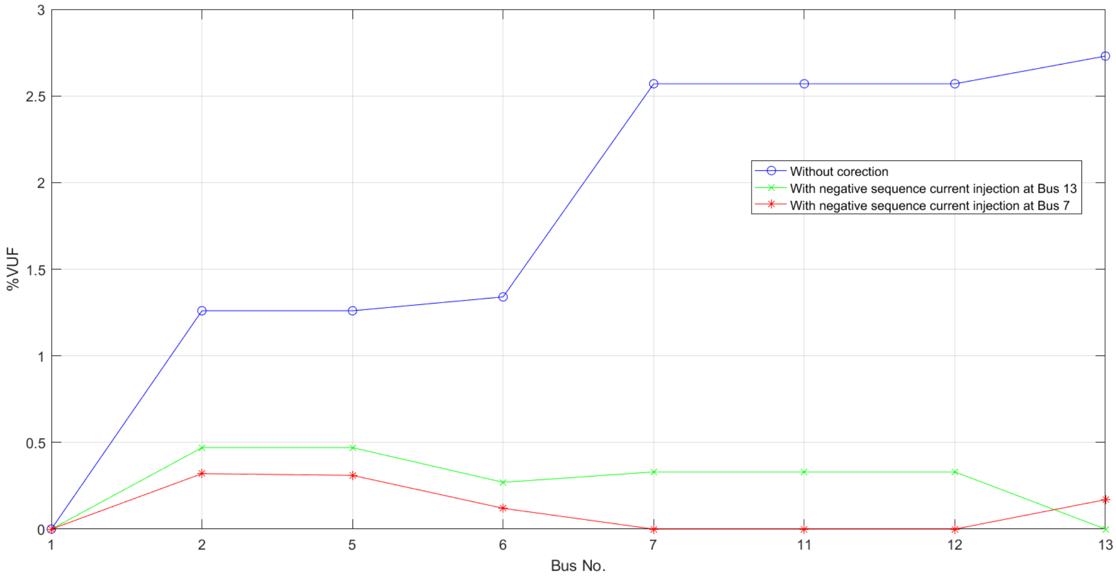

Fig. 3.13 Variation of VUF in a 13-bus URDS with a single FLIG connected under the injection of only negative sequence current.

3.5.3 Case Study III: 19-bus system

The third test system shown in Fig. A.4 is a practical 19-bus URDS starting from 132/11kV grid substation in Pathardhi, India. The line and load data are given in Table. A.13 [**?**]. The base case load flow results is provided in Table. A.15. The system's VUF has been observed to be insignificant for the base case load values shown in Table. A.13, despite the fact that it is unbalanced. In order to increase the voltage unbalance of the system, the complex loads are increased six times in phase a and three times in phase b in all buses. As a result, the voltage profile of the system is now considerably out of balance. The modified 19-bus URDS is used to compute the VUFs in the following case studies.

The first case involved no FLIG attachment, while the remaining five cases tested the effect of attaching one FLIG at bus 19, 17, 13, 10, and 5, respectively. The buses used in the case studies are chosen at random. The simulations involved setting both positive and zero sequence current injection to zero and using the proposed algorithm to control negative sequence current injection. Bus-1 serves as the slack bus in the system. The VUFs at all buses is computed after attaining the minimum VUFs for each case.

Fig. 3.14 illustrates the VUF values computed for all the buses in the six cases. The results show that applying unbalance voltage correction at bus 19, 17, 13, 10, and 5 resulted in a significant reduction in VUF at these buses from their original values of 2.90, 2.77, 2.71, 2.59, and 0.99, respectively, to 0, demonstrating the effectiveness of the proposed method. The bus closest to each of the aforementioned buses i.e. bus 15, 14, 11, 9, 12, and 4, experienced the next notable reduction in VUF.

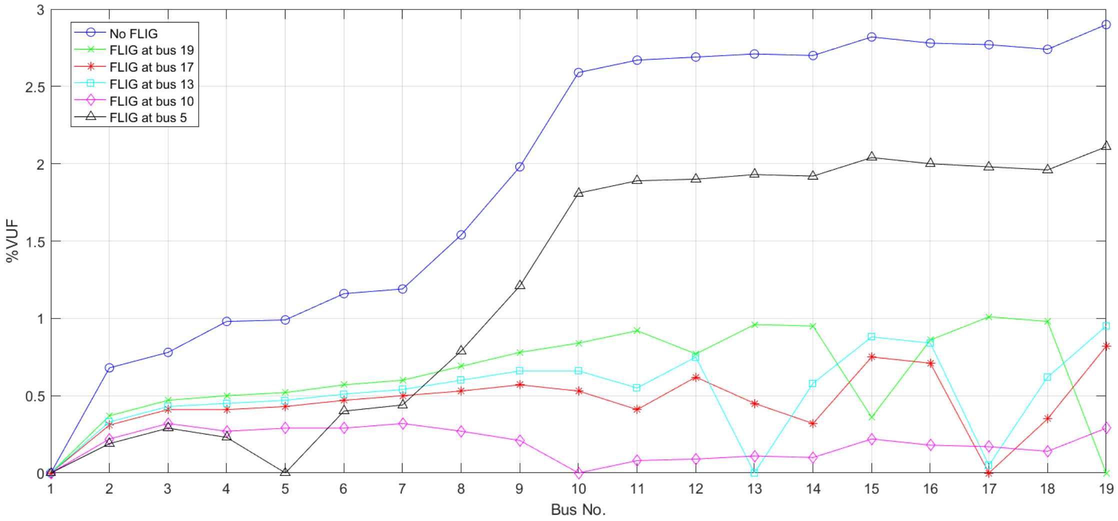

Fig. 3.14 Variation of VUF in a 19-bus URDS with a single FLIG connected under the injection of only negative sequence current.

3.5.4 Case Study IV: IEEE 34-bus system

The fourth test system is the standard 24.9 kV, IEEE 34-bus URDS, as depicted in Fig. A.5. The line and load data are given in Table. A.17 [**?**]. The base case load flow results is provided in Table. A.23. The network comprises both star and delta connections, with loads that maintain constant current, constant power, and constant impedance. The system includes both spot and distributed loads, and features both three-phase and single-phase buses. Voltage regulators and capacitors are neglected when evaluating the performance under unbalanced conditions. The integration of FLIGs is exclusive to three-phase buses, thus restricting their placement to such buses.

Correspondingly, VUFs are exclusively computed for these types of buses. Bus 2, 3, 4, 6, 7, 8, 9, 13, 15, 16, 17, 19, 20, 21, 22, 23, 25, 26, 27, 28, 29, 30, 31, 32, and 34 are three-phase buses, remaining buses are single-phase buses. FLIGs are first installed on bus 34, then on bus 22. The buses used in the case studies are chosen at random. Fig. 3.15 depicts the results for all the test scenarios. Similar to the investigation conducted on other unbalanced systems, it is seen that the proposed algorithm is capable of significantly reducing voltage unbalance in all buses, with the greatest reduction obtained in the bus to which the FLIG is connected.

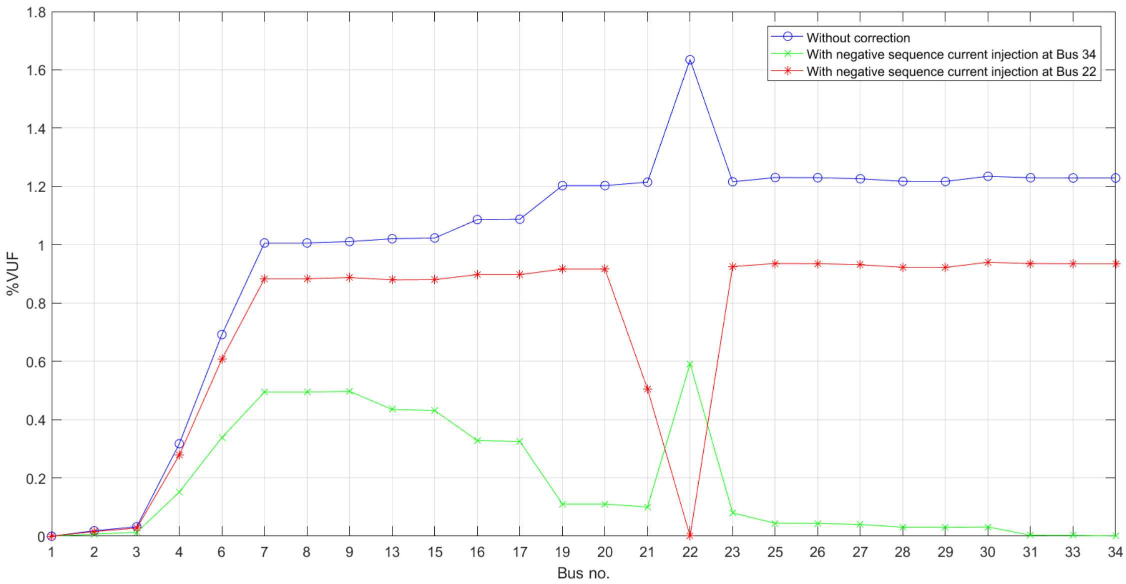

Fig. 3.15 Variation of VUF in a 34-bus URDS with a single FLIG connected under the injection of only negative sequence current.

3.6 Controller for implementation of P&O unbalanced voltage compensation

The grid-feeding inverters of a microgrid are current source inverters. Inner current control loops and outer dc-link voltage or power control loops are common features of these inverters. The controller's active and reactive power references are generated using either droop-based or communication-based control schemes. Renewable energy DGs do not typically operate at maximum power, so surplus capacity can be used for unbalanced voltage compensation. The perturb and observe method is proposed as a solution for unbalanced voltage compensation, and its effectiveness was demonstrated by applying it to four unbalanced radial distribution systems under various test conditions. The control scheme for implementation of the method using four-leg inverter is presented in this section. Fig. 3.16 shows the block-diagram of the proposed controller.

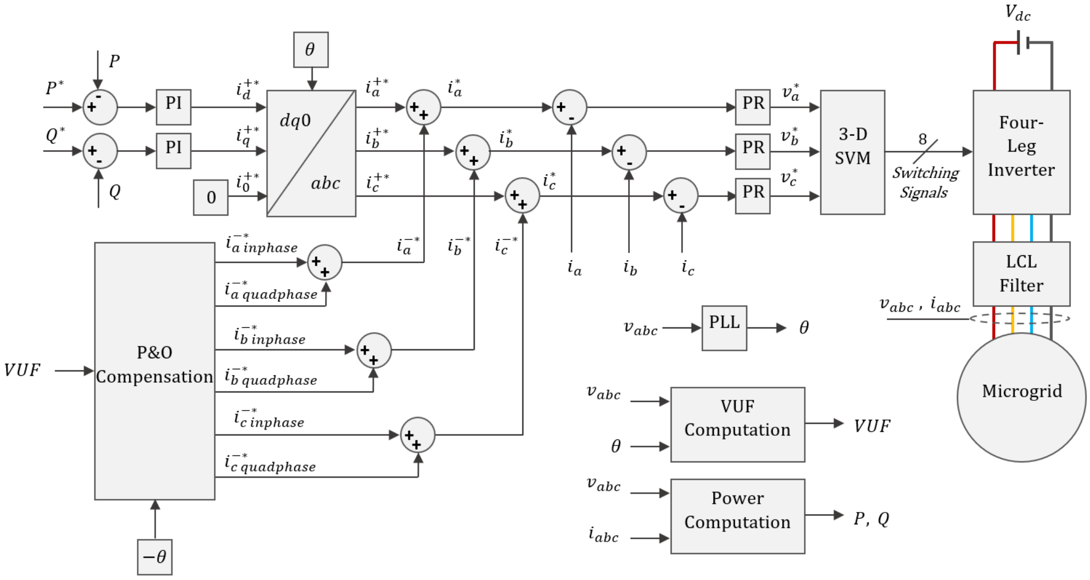

Fig. 3.16 Control scheme for implementation of P&O based unbalance voltage correction

The DER is integrated to the microgrid through a four-leg inverter and a LCL filter. 3-D SVM is used to generate the switching signals for the inverter, using the three-phase reference fed from three PR controllers as inputs. The inputs to PR controllers are the error signal of actual inverter current and the reference three-phase currents. The reference three-phase current is calculated by summing the positive and negative sequence current references. The positive sequence current reference controls the positive sequence real and reactive power injection. The P&O control unit generates the negative sequence current reference, which takes the VUF and phase information as input and produces the in-phase and quadrature-phase current components for each phase. Unbalanced voltage compensation is activated when the negative sequence voltage appears at the inverter terminals when connected to the grid.

3.7 Simulation validation

A Simulink model, as shown in Fig. 3.17 is developed to verify the performance of the proposed control scheme. The system comprises a simple network containing an FLIG that is controlled using the control scheme discussed in the previous section. A circuit breaker, which acts as the PCC, connects the FLIG to the microgrid. The microgrid consists of a balanced three-phase source and a distribution network. An unbalanced three-phase load is connected at the PCC. The objective of the study is to confirm the system's ability to mitigate voltage unbalance at the inverter's terminal, i.e., at PCC by using the proposed P&O method. Tab. 3.1 shows the parameters used for the simulation.

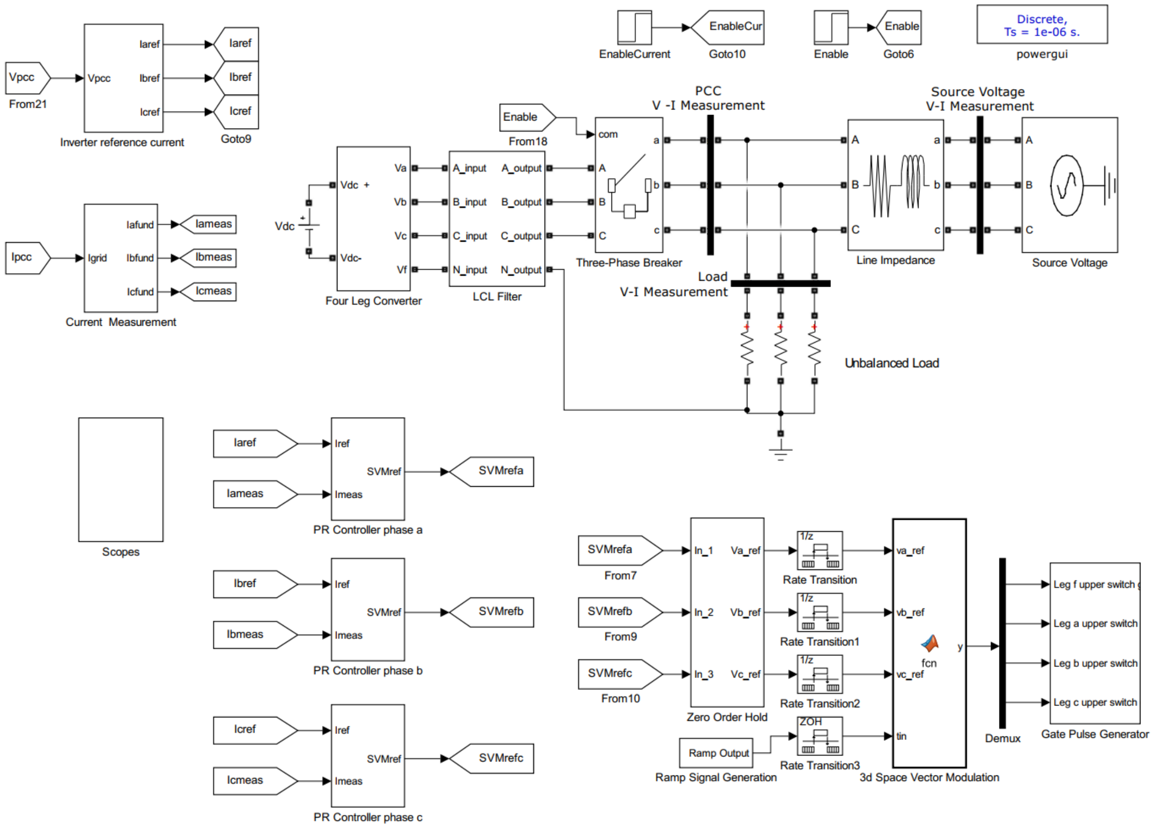

Fig. 3.17 Simulink model for implementation of P&O method

Initially the FLIG is disconnected from the microgrid. The positive sequence and negative sequence current demand of the unbalanced load is met by the three-phase source. The FLIG is connected to the microgrid at $t = 0.4$ sec and unbalance voltage correction is started at $t = 0.5$ sec. The reduction in VUF over time is shown in Fig. 3.18. As seen from the result the proposed method is able to reduce the VUF from 3.8 % to nearly 0%. However, since the method employs perturbation and observation, the VUF fluctuates around zero VUF instead of remaining precisely at zero. The positive and negative sequence component of voltage at PCC is shown in Fig. 3.19. As can be observed, the negative sequence voltage gradually decreases to zero after the activation of unbalanced voltage compensation at 0.5 sec. The voltage at PCC is displayed in Fig.3.20. A comparison between the voltage before and after correction is shown in Fig.3.21 and Fig.3.22. The outcomes indicate that the proposed control strategy for implementing the P&O method is effective in efficiently mitigating voltage unbalance.

Table 3.1 Parameter settings for simulation of P&O control scheme

Parameter	Value
P^*	2 kW
Q^*	0 KVAR
PI gain	0.1 & 10
V_{L-G}	230 V
PR gain	0.1 & 100
Switching frequency	5 kHz
DC link voltage	700 V
Grid side inductor	1 mH
Inverter side inductor	0.5 mH
Inverter capacitor	45 μF
Inductor resistance	0.04 Ω
Phase a load	9 kW
Phase b load	4 kW
Phase c load	1 kW

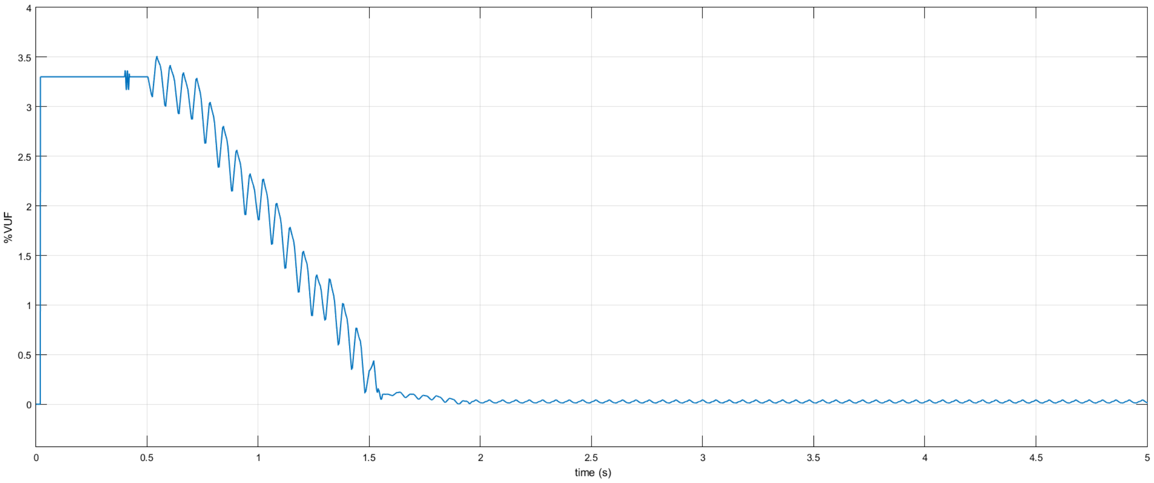

Fig. 3.18 VUF reduction with P&O based unbalance voltage correction

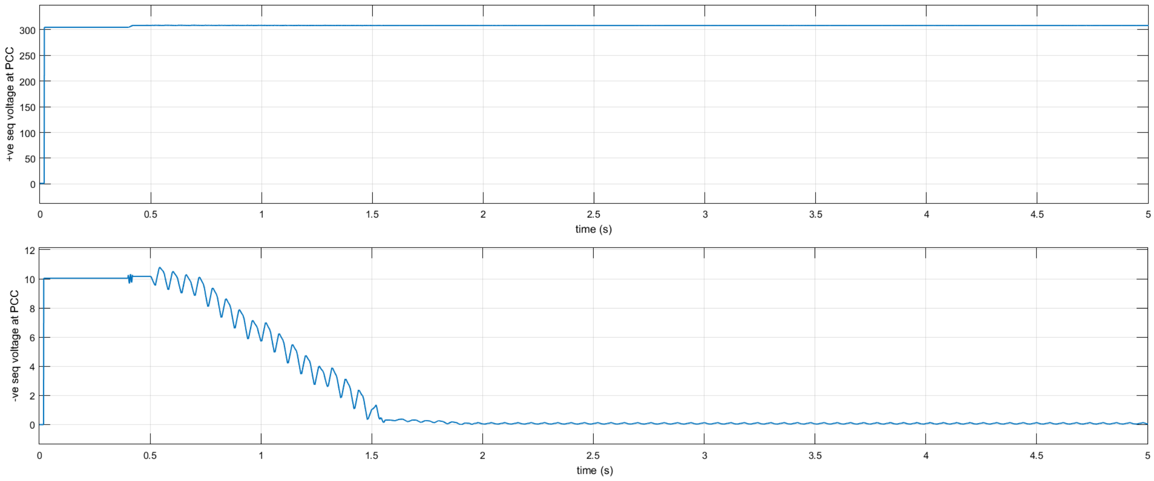

Fig. 3.19 Positive and negative sequence voltage at PCC

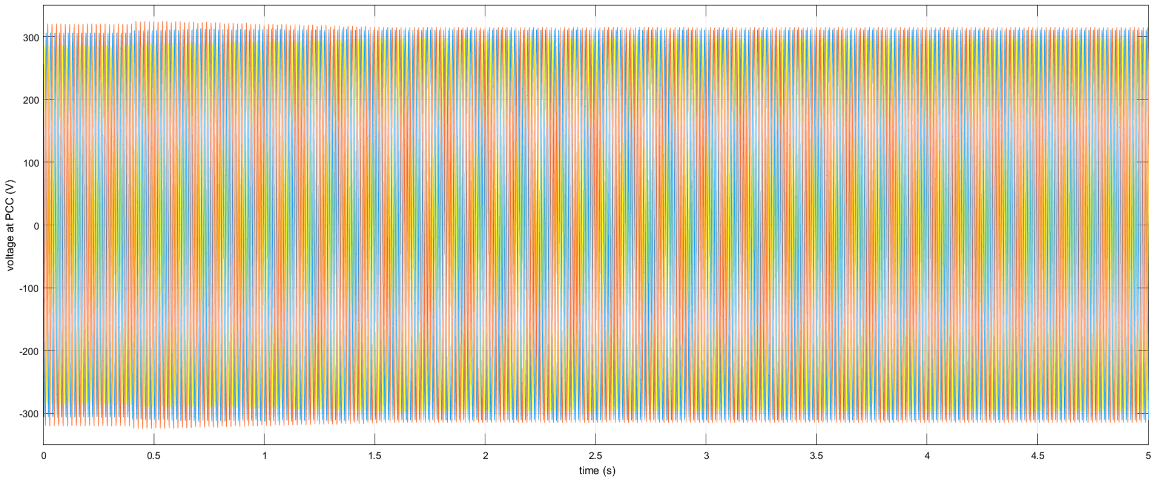

Fig. 3.20 Voltage at PCC

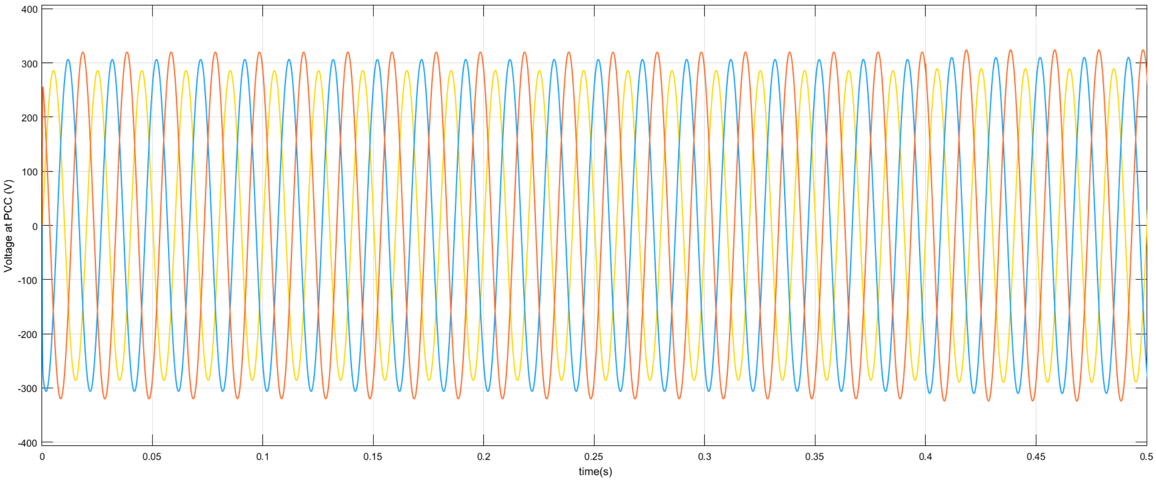

Fig. 3.21 Voltage at PCC before unbalance voltage correction

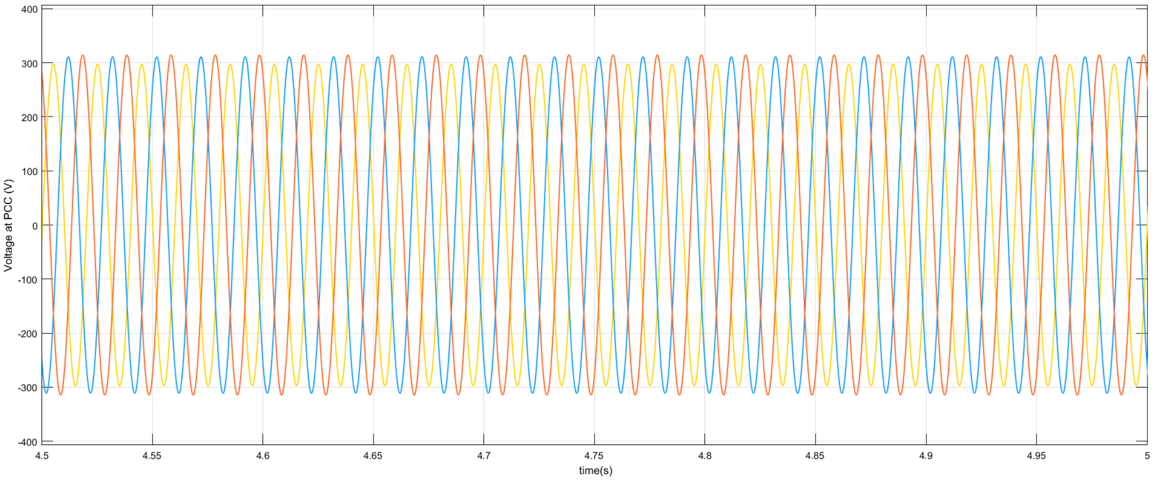

Fig. 3.22 Voltage at PCC after unbalance voltage correction

3.8 Discussion

The proposed algorithm's strength lies in how it generates negative sequence current. Unlike other methods, the proposed method does not require measuring negative sequence load current or negative sequence impedance angle eliminating the need for additional hardware. Therefore, the algorithm can be seamlessly integrated into the controller of the four-leg inverter. Based on the case studies conducted on the four unbalanced radial test systems, the following observations can be made:

- Installing FLIGs and using the proposed unbalanced voltage correction method can significantly reduce VUFs.
- The bus where the FLIGs are installed experiences the most significant correction, followed by the bus closest to it.
- While positive sequence current can provide some VUF correction, it is not substantial.
- When multiple FLIGs are installed, the VUF correction obtained is notably higher.
- The placement of FLIGs in the system determines the overall reduction in VUFs in three-phase buses. When FLIGs are installed in some buses, the correction obtained is significantly higher than in other cases where the correction is relatively low. As a result, there is an ideal location for FLIG installation where the total voltage unbalance of the microgrid is minimised. In the following chapter, algorithms for determining the ideal location for FLIG installation will be proposed.

3.9 Conclusion

In this chapter, a perturb and observe based method for correcting unbalanced voltages is proposed. The method involves injecting negative sequence current generated by combining two orthogonal components. The algorithm is evaluated using four test systems, and simulation results show that the proposed method can significantly reduce voltage unbalance. It is seen that the bus with the FLIG connection experiences the most substantial correction followed by the nearby buses. The controller for implementation of the proposed P&O method is developed and tested.

4

Optimal placement and sizing of distributed generators integrated to unbalanced low voltage microgrids by four-leg inverters

Using four-leg inverters for DG integration in microgrids has been shown to offer more benefits compared to using three-leg inverters. However, the extent of reduction in distribution losses and VUFs depends on the optimal sizing and placement of FLIGs. Installing FLIGs in sub-optimal locations can lead to insignificant reductions in distribution losses and overall VUF of the microgrid. Therefore, determining the ideal capacity and placement of FLIGs is crucial. Although the size and location can be determined iteratively using analytical methods, this method becomes complicated and time-consuming with an increase in the number of buses. Thus, optimization techniques are necessary to efficiently solve the problem of sizing and placing FLIGs for any number of buses in a microgrid.

In this chapter, a multi-objective particle swarm optimization (MOPSO)-based method and a Grey Wolf Optimization (GWO) based method is proposed for determining the ideal position and rating of DGs connected to a low-voltage unbalanced microgrid by four-leg inverters. There are two objectives: the first is to determine the positions and ratings of DGs for which the real power distribution loss is minimum, and the second is to determine the locations at which the total voltage unbalances in the microgrid are at their lowest. The optimization is obtained using two approaches: first, a weighted factor-based approach is used to obtain a unique solution based on the priorities assigned to each objective. Secondly, a Pareto-based approach is used to obtain all the non-dominated alternatives from which a specific solution may be chosen based on preference. The results obtained from both methods are compared with each other and also with an established method.

4.1 Computation of sum of voltage unbalance factors

The preceding chapter has shown that the decrease in VUFs across all buses is contingent on the positioning of FLIGs within the microgrid. Optimal placement of FLIGs can lead to the greatest reduction in overall VUFs. To assess the comprehensive impact of FLIG placement across various buses, the Summation of Voltage Unbalance Factors (SVUF), as defined by eqn. (4.1), is utilized.

$$SVUF = \sum_{i=1}^{N_{3\phi}} VUF_i \tag{4.1}$$

Where, $N_{3\phi}$ is the number of three-phase buses in the microgrid.

4.2 Problem definition

Let, M be a microgrid formed by N buses, G FLIGs, and L loads. Out of the N buses, let $N_{3\phi}$ be the three-phase buses of the microgrid. The problem consists of then assigning the G FLIGs to some of the $N_{3\phi}$ buses of the microgrid and finding their sizes S, so that the total real power loss in the distribution lines and the SVUF are minimized. The real power loss is given by eqn. (3.25) and the SVUF is given by eqn. (4.1), respectively.

4.2.1 Objective function formulation

The problem under consideration involves two primary objectives. The first objective aims to minimize the real power distribution loss by positioning FLIGs of the optimal size in optimal locations. The second objective is to minimize SVUF by locating FLIGs in the optimal positions and injecting negative sequence current at optimal values. Achieving both objectives simultaneously may not be possible. Therefore, two multi-objective methods have been employed:

1. A weighted factor-based method [?] has been utilized, which merges the objectives of real power loss reduction and SVUF reduction into a single objective

function, resulting in a single solution. The weights of the objective function can be assigned to favor one objective over the other. This is shown in eqn. (4.2).

$$Minimize\ f_1 = w_1 \frac{P_{Loss}}{P_{Loss_{base}}} + w_2 \frac{SVUF}{SVUF_{base}} \tag{4.2}$$

Where,

$w_1,\ w_2$ = weight assigned to the objectives, $0 \leq w_1, w_2 \leq 1,\ w_1 + w_2 = 1$
$P_{Loss_{base}}$ = Real power distribution loss before FLIG placement
$SVUF_{base}$ = SVUF before FLIG placement
P_{Loss} = Real power distribution loss after FLIG placement
$SVUF$ = SVUF after FLIG placement

2. A Pareto-based approach has been utilized as the second method. This method produces a set of all non-dominated alternatives (Pareto-front). Based on preference, one of the non-dominant solutions can be selected. The objective function is given in eqn. (4.3)

$$\begin{aligned} &Minimize\ f_2 = P_{Loss} \\ &Minimize\ f_3 = SVUF \end{aligned} \tag{4.3}$$

4.2.2 Constraints

The solutions obtained must satisfy the following constraints:

Equality constraints

- Power balance in the microgrid

$$P_{slack} + \sum_{i=1}^{G} P_{FLIG_i} = \sum_{i=1}^{N} P_{L_i} + P_{Loss} \tag{4.4}$$

$$Q_{scack} + \sum_{i=1}^{G} Q_{FLIG_i} = \sum_{i=1}^{N} Q_{L_i} + Q_{Loss} \tag{4.5}$$

Where,

$$
\begin{aligned}
P_{slack} &= \text{real power at slack bus} \\
Q_{slack} &= \text{reactive power at slack bus} \\
P_{FLIG_i} &= \text{real power delivered by the i}^{\text{th}} \text{ FLIG} \\
Q_{FLIG_i} &= \text{reactive power delivered by the i}^{\text{th}} \text{ FLIG} \\
P_{Loss} &= \text{real power distribution loss} \\
Q_{Loss} &= \text{reactive power distribution loss}
\end{aligned}
$$

Inequality constraints

- Maximum FLIG size at any bus

$$\forall i \in N_{3\phi} \quad P_{FLIG_i} \leq P_{FLIG_i}^{Max} \tag{4.6}$$

- After unbalanced voltage correction is applied to any bus, the VUFs of none of the buses should exceed their base VUFs.

$$\forall i \in N_{3\phi} \quad VUF_i \leq VUF_{base_i} \tag{4.7}$$

4.3 Particle Swarm Optimization

Particle Swarm Optimization (PSO) is a swarm meta-heuristic based optimization technique [**?**]. In a PSO algorithm, the population is comprised of particles. This is an iterative computational method where the particles explore and exploit the search area until the solution has converged within a predetermined tolerance level or until a fixed number of iterations has been attained. During each iteration i, the next co-ordinate of the j^{th} particle is computed based on its current position x_j^i, personal best position $pbest_j^i$ (position at which the particle j has obtained its best solution till the i^{th} iteration), and global best position $gbest^i$ (position at which the best solution has been obtained by all the particles till the i^{th} iteration). To determine the next position of the j^{th} particle, the current velocity is first modified by eqn. (4.8).

$$v_j^{i+1} = \omega v_j^i + K_1\alpha_1(pbest_j^i - x_j^i) + K_2\alpha_2(gbest_j - x_j^i) \tag{4.8}$$

The next position of the j^{th} particle is then modified by eqn. (4.9)

$$x_j^{i+1} = x_j^i + v_j^{i+1} \tag{4.9}$$

Where,

$$\begin{aligned} v_j^i &= \text{current velocity of the } j^{th} \text{ particle} \\ \omega &= \text{inertia co-efficient} \\ K_1 \text{ and } K_2 &= \text{acceleration co-efficients} \\ \alpha_1 \text{ and } \alpha_2 &= \text{random numbers in 0 to 1} \end{aligned}$$

4.4 Proposed algorithm for placement and sizing of FLIGs using PSO

Step 1: Perform modified unbalanced load flow analysis discussed in Sec. 3.3 with $(P_{DG_1} = 0, \cdots, P_{DG_G} = 0,\ i_{inphase_1} = 0,\ \cdots,\ i_{inphase_G} = 0,\ i_{quadphase_1} = 0, \cdots, i_{quadphase_G} = 0)$. Where, G is the number of FLIGs that must be placed in G of the $N_{3\phi}$ buses of the microgrid.

Step 2: Calculate $P_{Loss_{base}}$ and $SVUF_{base}$ of the microgrid.

Step 3: Generate all possible combinations of three-phase buses from the $N_{3\phi}$ buses, taking G three-phase buses at a time.

Step 4: Select the first combination of buses.

Step 5: Set iteration counter to zero.

Step 6: (Applying PSO) Generate an initial population of particles and randomly assign positions and velocities to each particle. The dimensions of the search space are $[P_{DG_1}, \cdots, P_{DG_G}, i_{inphase_1}, \cdots, i_{inphase_G}, i_{quadphase_1}, \cdots, i_{quadphase_G}]$

Step 7: Run the unbalanced load flow analysis for each particle, and then determine the values of the objective function, real power loss, and SVUF. Test the constraints and discard the infeasible solutions.

Step 8: Update the population's *gbest* value and the *pbest* values for each individual particle.

Step 9: Modify the velocity and position of the population.

Step 10: If the difference between the current iteration's gbest value and the previous iteration is within the tolerance set or if a maximum number of iterations has been reached, continue on to Step 11; else, increase the iteration counter by one and repeat steps 7 to 10.

Step 11: Store the *gbest* value for the current combination of buses along with the corresponding DG sizes, real power loss, SVUF and objective function value.

Step 12: If the current bus combination is not equal to the last combination of buses, select the next combination of buses and repeat steps 5 to 12 else continue to step 13.

Step 13: For weighted-based optimization, find the combination of buses for which the objective function given in eqn. (4.2) is minimum. For the Pareto-based approach find all the combinations of buses for which eqn. (4.3) has non-dominant solutions.

Step 14: Report.

4.5 PSO simulation results and analysis

The proposed method has been employed on four URDS. MATLAB codes are developed for the proposed algorithms. The parameter settings for MOPSO is given in Table. 4.1.

Table 4.1 Parameter settings for MOPSO

K_1	K_2	w	*population*	*max iteration*	w_1	w_2
2	2	0.5	50	1000	0.5	0.5

4.5.1 Case Study I: 25-bus system

The first test system is the 4.16 kV, 25-bus unbalanced radial distribution system depicted in Fig. A.2.

Optimal placement of one FLIG

Firstly, the impact of installing one FLIG is examined on the real power loss and SVUF. Initially, without any FLIG, the SVUF is 8.34, the reactive power loss is 167.28 KVAR, and the total real power loss is 150.12 kW. Using weighted factor-based MOPSO, the optimal position for placing one FLIG is determined to be bus 7 with a size of 1890 kW. Upon installation, the observed SVUF is 2.49, the reactive power loss is reduced to 76.22 KVAR, and the real power loss is lowered to 67.67 kW. The outcomes are compared with Bhimarasetti et al.'s method [**?**], which involved installing a DG of 1945 kW power at bus 7. The proposed method achieves a reduction of 54.43% in reactive power loss, 54.94% in real power loss, and 74.06% in SVUF, as compared to the existing method described in [**?**]. The reactive power loss reduced to 87.35 kVAR, the real power loss to 79.58 kW, and the SVUF is calculated to be 5.45. Fig. 4.1, Fig. 4.2, and Fig. 4.3 illustrate the comparison of voltage profiles for one FLIG placement. By using FLIGs with unbalanced voltage compensation enabled, the proposed approach has been shown to enhance voltage profiles, and considerably decrease SVUF, reactive, and real power loss compared to [**?**]. This demonstrates the advantages of the proposed approach. The convergence plot of PSO with weighted-factor based approach is shown in Fig.4.4

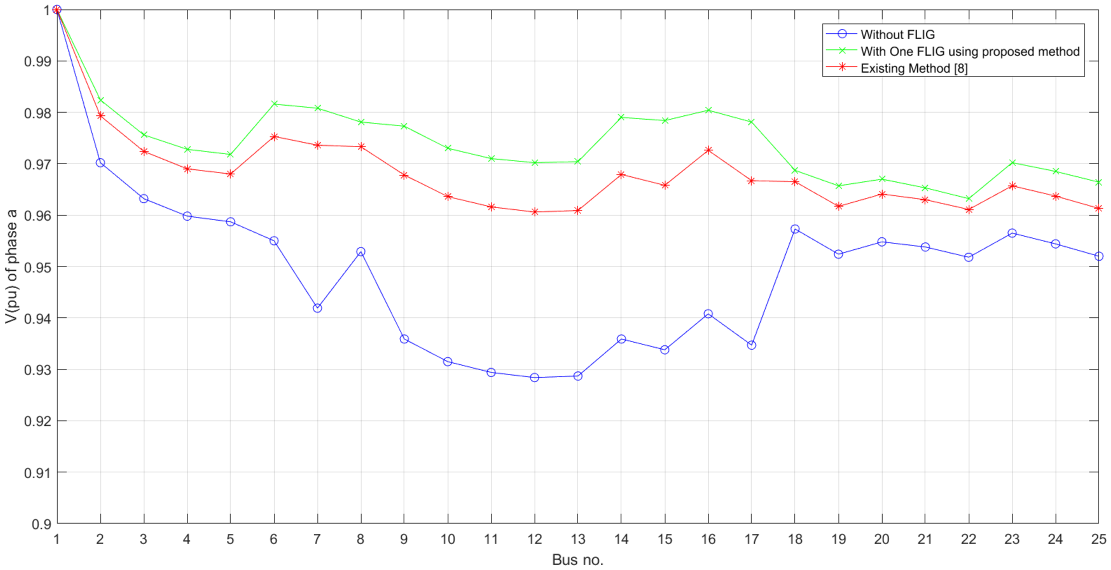

Fig. 4.1 Comparison of phase a voltage profiles before and after FLIG placement in the 25-bus system

Three non-dominant solutions are found when Pareto-based MOPSO is applied to one FLIG placement. The numerical findings are displayed in Table. 4.2 and the Pareto front of non-dominant solutions is depicted in Fig. 4.5. Placing a FLIG of 1890 kW at bus 7 results in the lowest real power loss, with observed SVUF, reactive power loss, and real power loss values of 2.49, 76.22 kVAR, and 67.77 kW, respectively. The maximum reduction in SVUF is achieved by placing a FLIG of 2830 kW at bus 3, with observed SVUF, reactive power loss, and real power loss values of 2.35, 72.78 kVAR, and 73.29 kW, respectively. The optimal-compromised solution is obtained by placing a FLIG of 2296 kW at bus 6, resulting in observed SVUF, reactive power

Table 4.2 Non-dominant solutions for placement of one FLIG in the 25-bus URDS

Location	FLIG Size (kW)	Reactive Power Loss (kVAR)	Real Power Loss (kW)	SVUF
3	2830	72.78	73.29	2.35
6	2296	76.41	71.57	2.37
7	1890	76.22	67.77	2.49

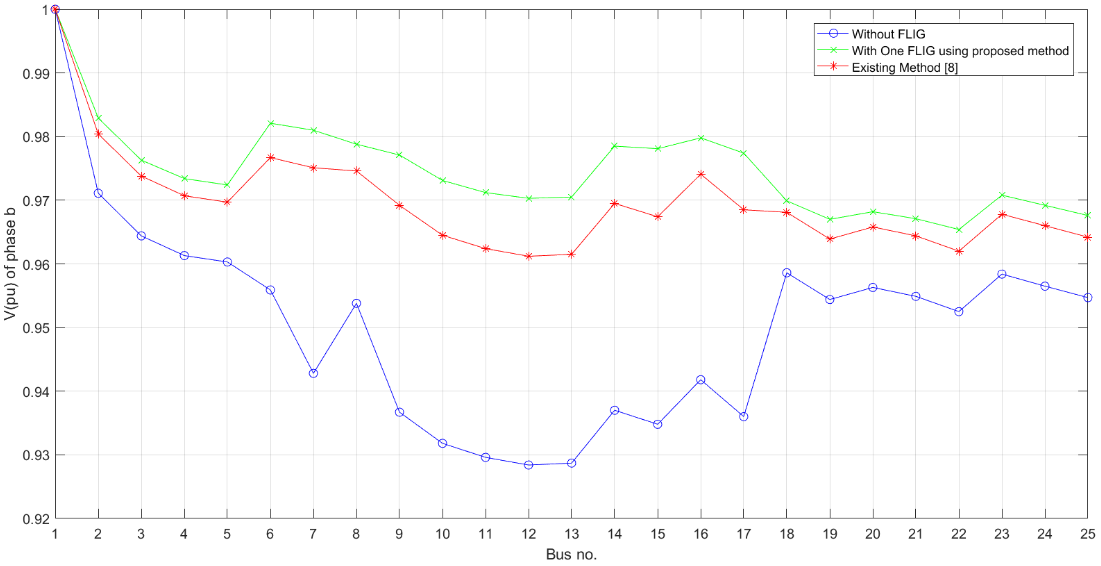

Fig. 4.2 Comparison of phase *b* voltage profiles before and after FLIG placement in the 25-bus system

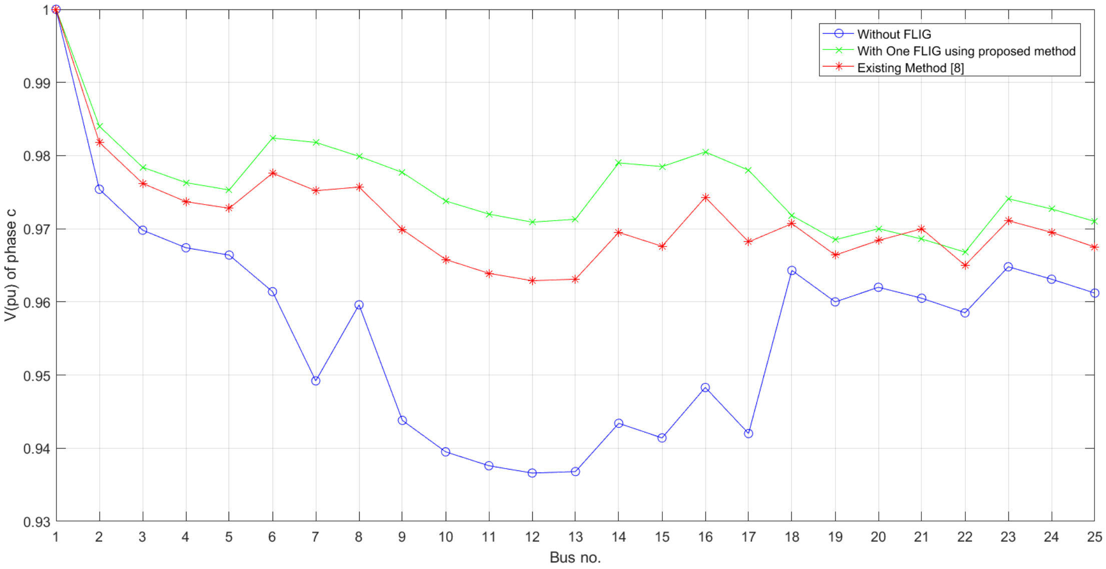

Fig. 4.3 Comparison of phase *c* voltage profiles before and after FLIG placement in the 25-bus system

loss, and real power loss values of 2.37, 76.41 kVAR, and 71.57 kW, respectively. The convergence plot of PSO with Pareto front approach for real power minimization and VUF minimization at bus 2 is shown in Fig.4.6 and Fig. 4.7, respectively.

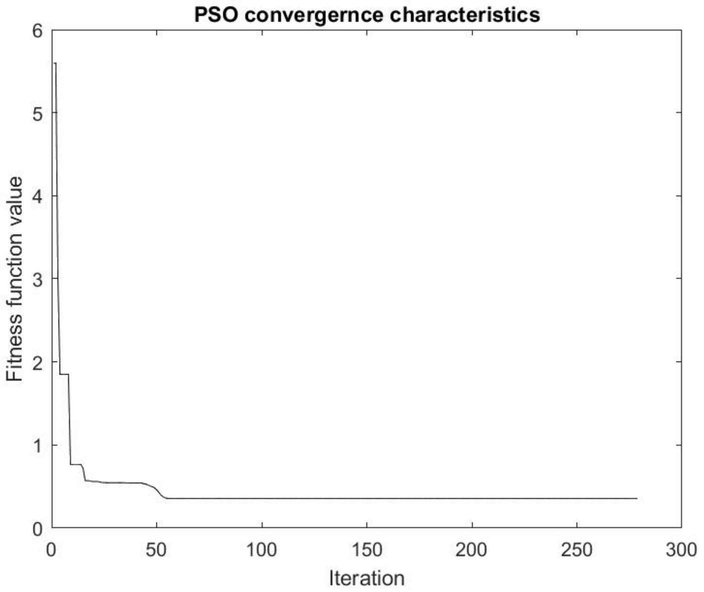

Fig. 4.4 Convergence plot of PSO with one FLIG in a 25-bus system

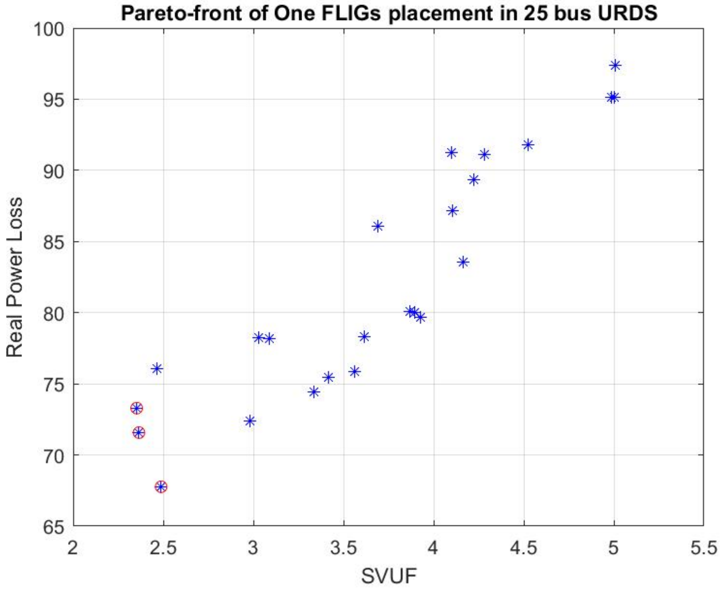

Fig. 4.5 Pareto front for one FLIG placement in the 25-bus URDS

Optimal placement of two FLIGs

The placement of two FLIGs using the weighted factor-based MOPSO approach resulted in the optimal locations of buses 7 and 18. Fig. 4.8 displays the objective function value for each bus combination. The total SVUF, reactive power loss, and real power loss obtained are 0.80, 54.67 kVAR, and 50.30 kW, respectively. When two FLIGs are used, there is a reduction of 90.4%, 67.31%, and 66.44% in SVUF, reactive power loss, and

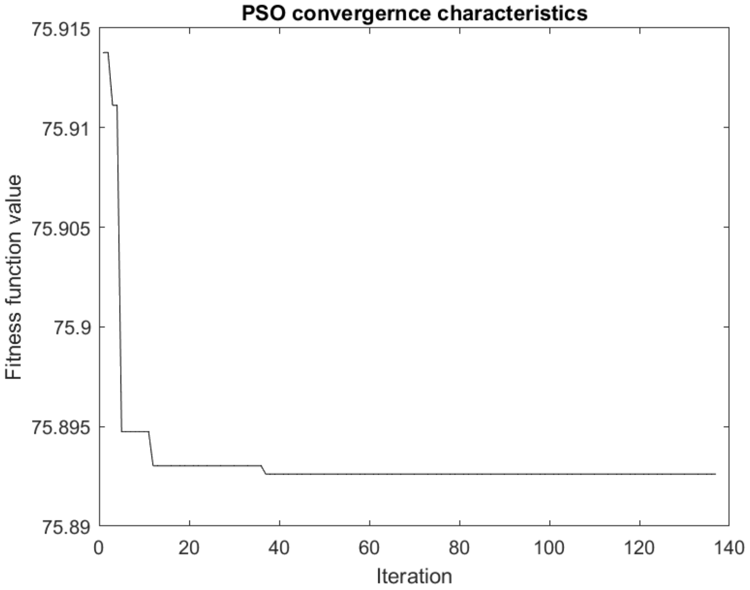

Fig. 4.6 PSO convergence plot with one FLIG in a 25-bus system for active power loss minimization

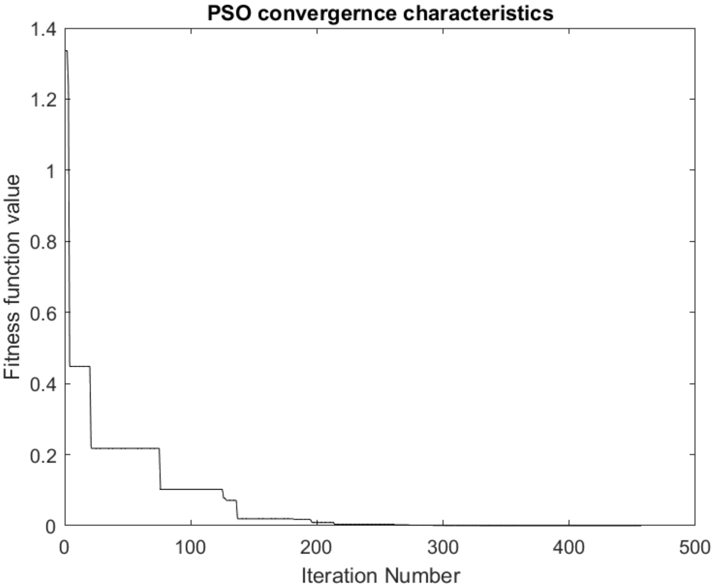

Fig. 4.7 PSO convergence plot with one FLIG in a 25-bus system for VUF minimization

real power loss, respectively. Table. 4.3 presents the comparison of results for all test scenarios. The reductions in SVUF, reactive power loss, and real power loss are found to be larger with two FLIGs than with one FLIG. The comparison of VUFs for each test scenario is illustrated in Fig. 4.9. When a FLIG is placed at bus 7, the negative sequence current demand of bus 7 and all buses connected downstream are shared by the PCC bus and the FLIG at bus 7. This results in the highest unbalance voltage correction observed at bus 7, and subsequently in all the downstream buses. Similarly, with two FLIGs placed at buses 7 and 18, the negative sequence current demand of bus 7 and its downstream buses are shared by the PCC bus and the FLIG at bus 7, and the negative sequence current demand of bus 18 and its downstream buses are shared by the PCC bus and the FLIG at bus 18. Therefore, the maximum unbalance voltage correction is observed at buses 7 and 18, followed by all other downstream buses. It can be observed from the Fig. 4.9 that the installation of two FLIGs results in the highest unbalance voltage correction. The convergence plot of PSO with weighted-factor based approach is presented in Fig. 4.10.

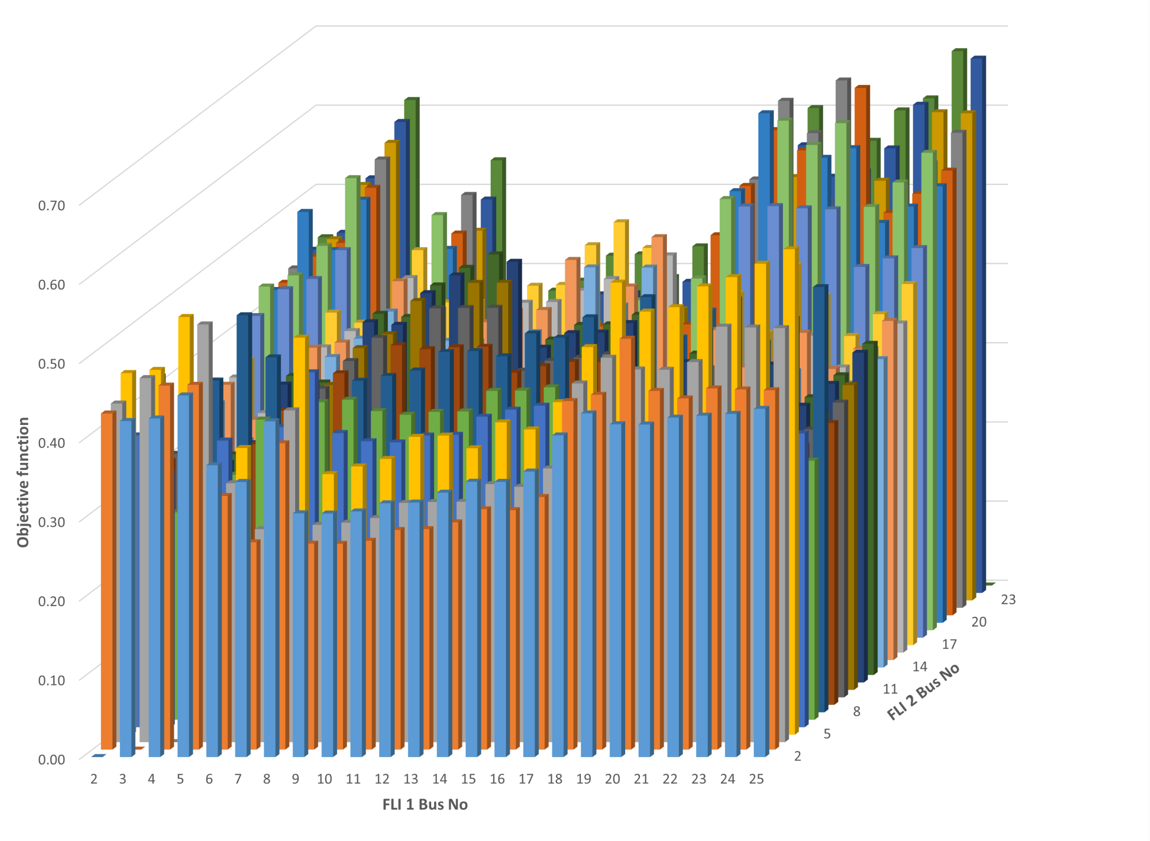

Fig. 4.8 Plotting the objective function for the installation of two FLIGs in a 25-bus system using the weighted factor-based MOPSO.

Using Pareto front based MOPSO, the placement of two FLIGs results in three non-dominant solutions, among which the optimal solution depends on the objective being optimized. Placing FLIGs of 1503 kW and 1388 kW at buses 7 and 18, respectively, yields the minimum real power loss, with SVUF, reactive power loss, and real power loss of 0.80, 54.67 kVAR, and 50.30 kW, respectively. Placing FLIGs of 2116 kW and 1027 kW at buses 3 and 10, respectively, provides the maximum reduction in SVUF, with SVUF, reactive power loss, and real power loss of 0.74, 55.23 kVAR, and 51.96

Table 4.3 Comparison of results for placement of FLIGs in 25-bus URDS

	Without FLIG	With One FLIG	With Two FLIGs	Existing Method [?]
Location	—	7	7 & 18	7
DG size (kW)	—	1890	1503 & 1388	1944
Real Power Loss (kW)	150.12	67.77	50.30	79.58
Reactive Power Loss (kVAR)	167.28	76.22	54.67	87.35
SVUF	8.34	2.49	0.80	5.45

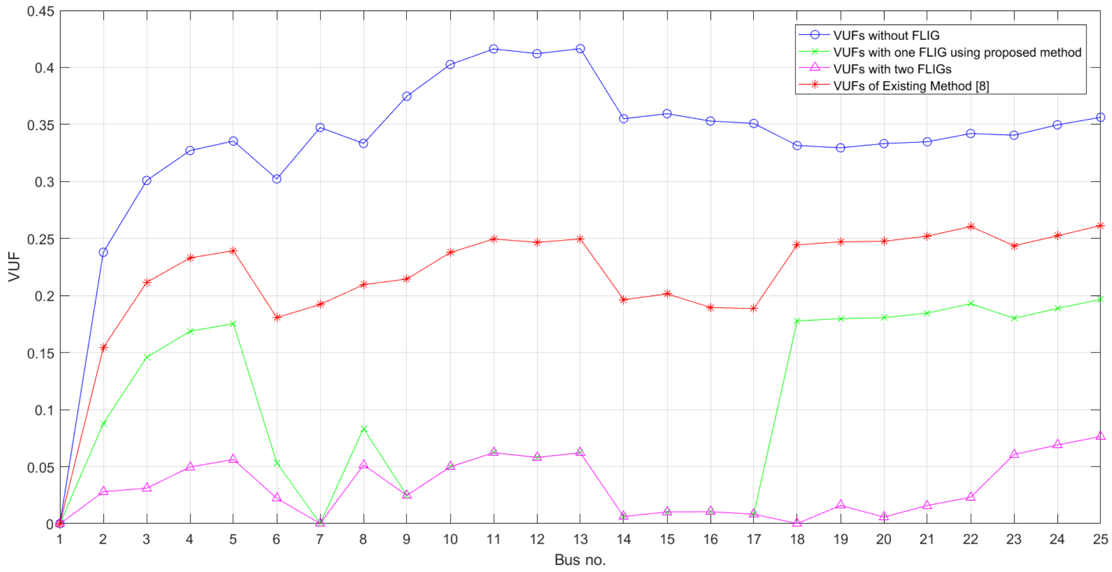

Fig. 4.9 Comparison of VUFs for all the test scenarios of the 25-bus system

kW, respectively. The optimal compromise solution, with FLIGs of 1855 kW and 1418 kW placed at buses 3 and 7, respectively, results in SVUF, reactive power loss, and real power loss of 0.76, 54.95 kVAR, and 51.82 kW, respectively. The numerical findings and Pareto front of non-dominant solutions can be found in Table. 4.4 and Fig. 4.11, respectively.

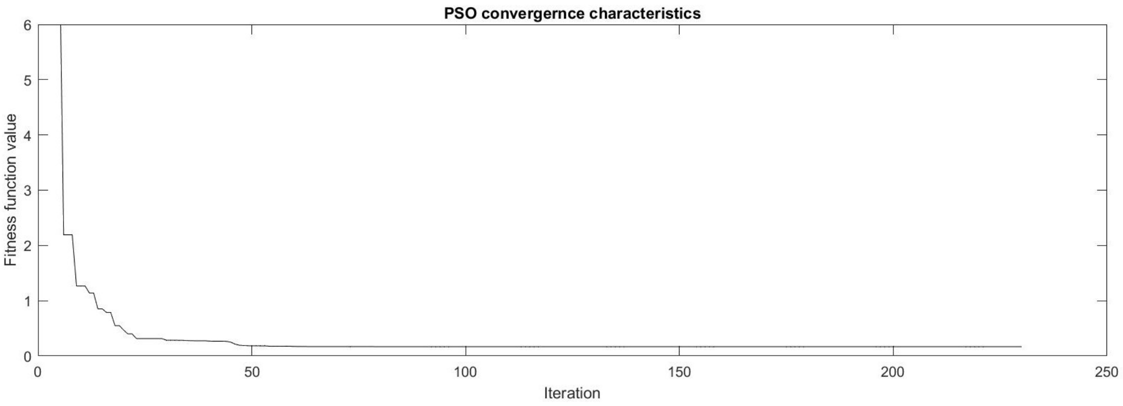

Fig. 4.10 PSO convergence plot for placement of two FLIG in 25-bus URDS

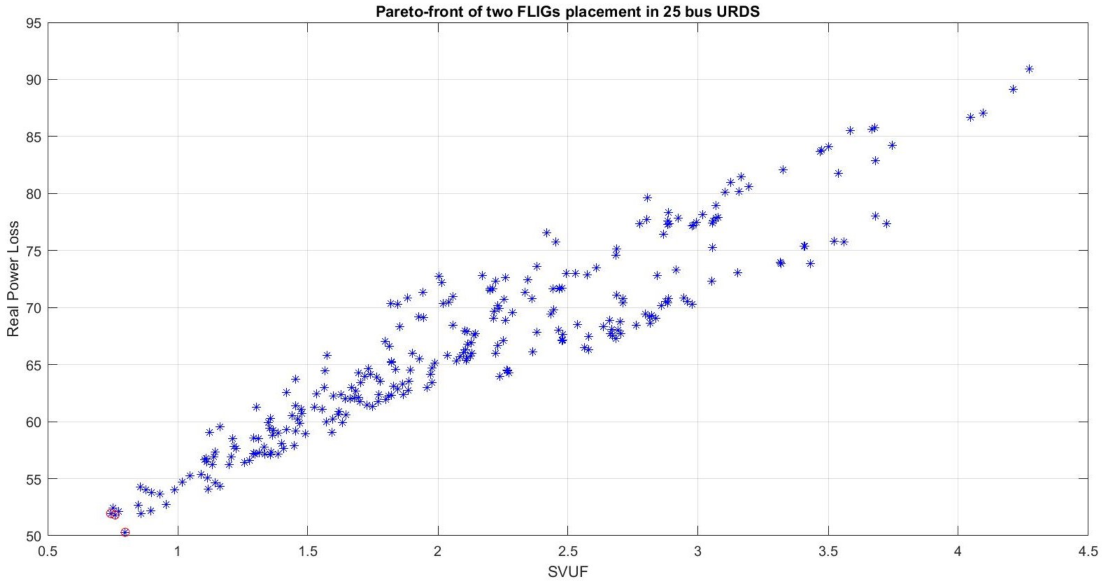

Fig. 4.11 Pareto front for placement of two FLIGs in the 25-bus URDS

Table 4.4 Non-dominant solutions for placement of two FLIGs in the 25-bus URDS

Location	FLIG Sizes (kW)	Reactive Power Loss (kVAR)	Real Power Loss (kW)	SVUF
3 & 7	1855 & 1418	54.95	51.82	0.76
3 & 10	2116 & 1027	55.23	51.96	0.74
7 & 18	1503 & 1388	54.67	50.30	0.80

4.5.2 Case Study II: IEEE 13-bus system

The second test system is the standard 4.16 kV IEEE 13-bus URDS illustrated in Fig. A.3. This system has three-phase, single-phase, and two-phase buses. As FLIGs can only be integrated into three-phase buses, their placements are also restricted to the three-phase buses. Single-phase and two-phase buses are excluded from SVUF computations. The total load of the system is 3466 kW and 2101.59 kVAR.

Optimal placement of one FLIG

Without any FLIG installed, the SVUF, reactive power loss, and real power loss for the IEEE 13-bus URDS are 14.32, 433.44 kVAR, and 147.39 kW, respectively. For the placement of one FLIG using the weighted factor-based MOPSO, the optimal location obtained is bus 7 (or 12 with the switch closed). Fig. 4.12 shows the objective function's plot at various buses. With one FLIG installed, the SVUF, reactive power loss, and real power loss are reduced to 8.54 (-40.36%), 154.44 KVAR (-64.37%), and 59.47 kW (-59.65%), respectively.

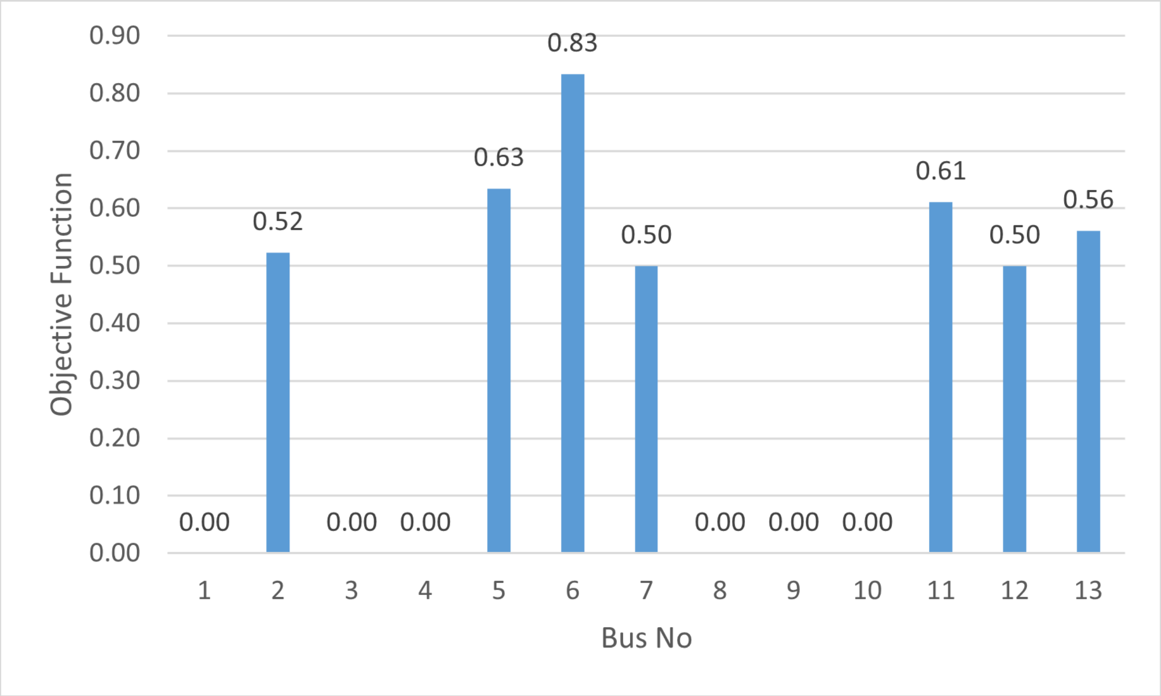

Fig. 4.12 Plotting of objective function for placement of one FLIG in the 13-bus URDS using weighted factor-based MOPSO

Using Pareto-based MOPSO to place one FLIG results in obtaining three non-dominant solutions. The numerical results are presented in Table. 4.5, while the Pareto front of these solutions is illustrated in Fig. 4.13. Placing the FLIG at bus 7 yields a minimum real power loss of 59.47 kW, while placing it at bus 2 yields a minimum SVUF of 6.2. The best-compromised solution is achieved by placing the FLIG on bus 11.

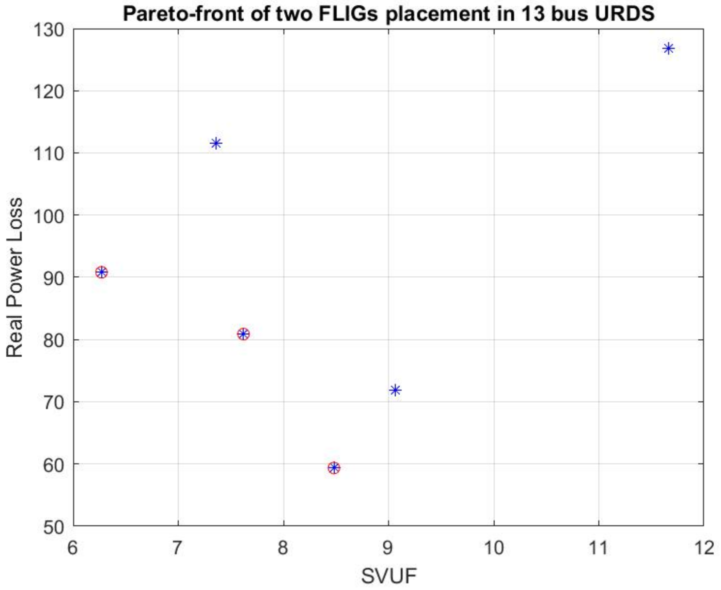

Fig. 4.13 Pareto front for placement of one FLIG in the 13-bus URDS

Table 4.5 Non-dominant solutions for placement of one FLIG in the 13-bus URDS

Location	FLIG Size (kW)	Reactive Power Loss (kVAR)	Real Power Loss (kW)	SVUF
2	3232	251.97	90.42	6.2
7	3232	154.44	59.47	8.54
11	2178	214.98	80.88	7.62

Optimal placement of two FLIGs

Using weighted factor-based MOPSO, buses 2 and 7 are found to be the optimal locations for two FLIGs placements. Fig. 4.14 displays the objective function values for the installation of these two FLIGs. The total SVUF observed are 1.03, with reactive power loss at 134.89 kVAR and real power loss at 55.12 kW. These values represent a significant reduction in SVUF, reactive power loss, and real power loss by 92.81%, 68.86%, and 62.5%, respectively. Table. 4.6 presents a comparison of the results for each test scenario.

Three alternatives for the placement of two FLIGs were identified using the Pareto method. The Pareto front of non-dominant solutions is shown in Fig. 4.15, and Table. 4.7 presents the corresponding numerical outcomes. The placement of two

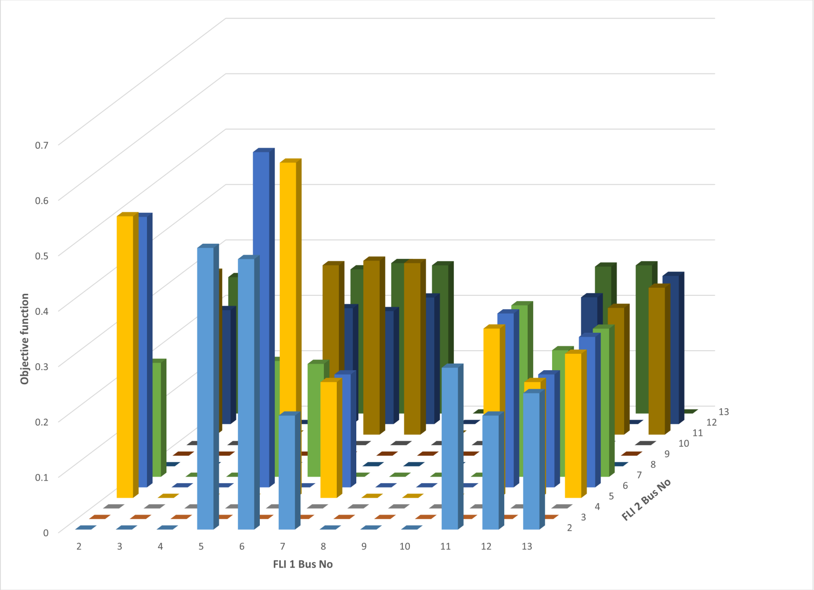

Fig. 4.14 Plotting the objective function for the installation of two FLIGs in the IEEE 13-bus system using the weighted factor-based MOPSO.

Table 4.6 Comparison of results for placement of FLIGs in the 13-bus URDS

	Without FLIG	With One FLIG	With Two FLIGs
Location	—	7	2 & 7
DG size (kW)	—	3232	934 & 2449
Real Power Loss (kW)	147.39	59.47	55.12
Reactive Power Loss (kVAR)	433.44	154.44	134.89
SVUF	14.32	8.54	1.03

FLIGs at buses 6 and 7, with capacities of 582 kW and 2518 kW respectively, yields the minimum real power loss. This solution results in an SVUF of 1.95, a reactive power loss of 131.44 kVAR, and a real power loss of 51.99 kW. Placing FLIGs at buses 2 and 7, with capacities of 934 kW and 2449 kW respectively, yields the maximum reduction in SVUF. In this solution, the observed SVUF is 1.03, with reactive power loss at 134.89 kVAR and real power loss at 55.12 kW. The best-compromised solution involves placing two FLIGs of 632 kW and 2825 kW at buses 5 and 7 respectively. This solution results in an observed SVUF of 1.27, a reactive power loss of 136.67 kVAR, and a real power loss of 55.08 kW.

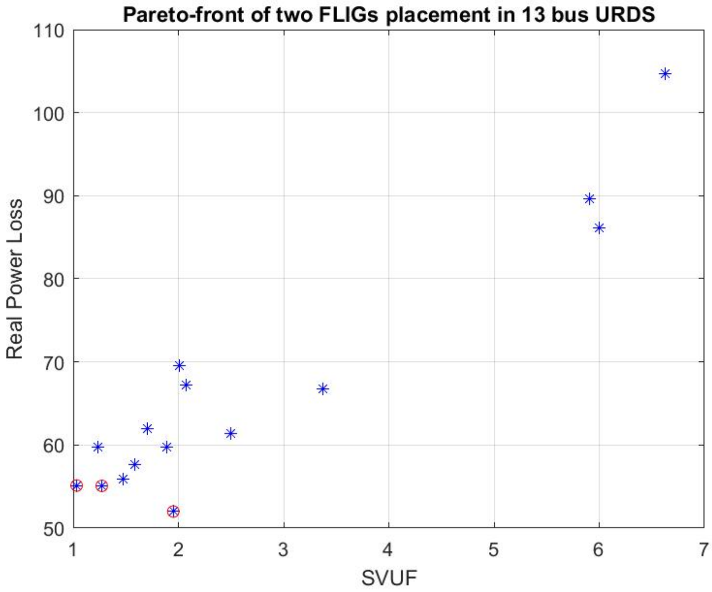

Fig. 4.15 Pareto front for placement of two FLIGs in the 13-bus URDS

Table 4.7 Non-dominant solutions for placement of two FLIGs in the 13-bus URDS

Location	FLIG Sizes (kW)	Reactive Power Loss (kVAr)	Real Power Loss (kW)	SVUF
2 & 7	934 & 2449	134.89	55.12	1.03
5 & 7	632 & 2825	136.37	55.08	1.27
6 & 7	582 & 2518	131.44	51.99	1.95

4.5.3 Case Study III: 19-bus system

The third test system is a 19-bus URDS, illustrated in Fig. A.4. The system's total load is 365.94 kW and 177.27 kVAR. The SVUF, reactive power loss, and real power loss in the base case are 0.1863, 1.83 kVAR, and 4.24 kW, respectively.

Optimal placement of one FLIG

The best location for one FLIG has been found using a weighted-factor approach to be bus-11. The optimal FLIG size is determined to be 242 kW. The real power loss is determined to be 1.23 kW, the reactive power loss is determined to be 0.53 kVAR, and the SVUF is determined to be 0.1176. The placement of one FLIG reduces real power loss by 71%, reactive power loss by 71%, and SVUF by 37%. Fig. 4.16 depicts the objective function plot at various buses for the weighted-factor-based approach.

The Pareto-based approach yields two non-dominant solutions. The Pareto front of non-dominant solutions is depicted in Fig. 4.17, and the numerical results are presented

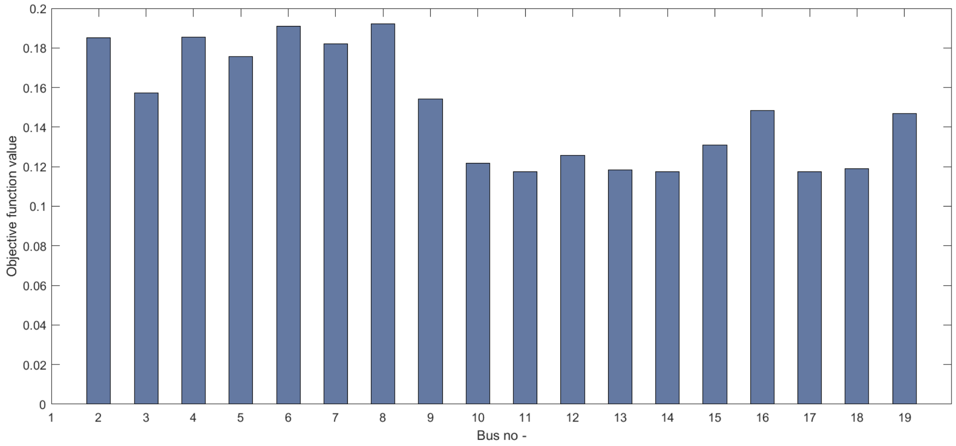

Fig. 4.16 Plotting of objective function for placement of one FLIG in the 19-bus URDS using weighted factor-based MOPSO

in Table. 4.8. When a 242 kW FLIG is installed in bus-11, a minimum SVUF of 0.1176 is obtained. The real power loss is 1.23 kW, and the reactive power loss is 0.53 kVAR. Bus-10 is determined to be the optimal location for minimising real power loss. The optimal FLIG size has been found to be 257 kW. The real power loss obtained is 1.14 kW, the reactive power loss obtained is 0.49 kVAR, and the SVUF obtained is 0.1218.

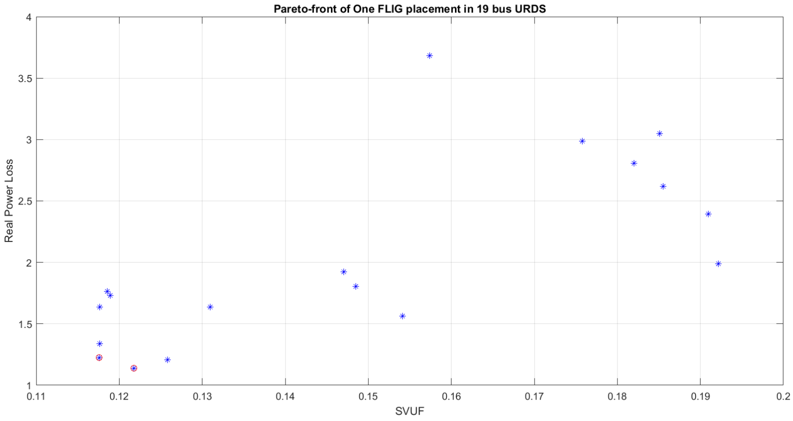

Fig. 4.17 Pareto front for placement of one FLIG in the 19-bus URDS

Optimal placement of two FLIGs

The best locations for the placement of two FLIGs have been identified using the weighted-factor approach to be bus- 4 and bus- 10. The optimal FLIG sizes obtained are 130 kW and 220 kW, respectively. The SVUF obtained is 0.0668, the reactive power loss is 0.42 kVAR, and the real power loss is 0.98 kW. Thus, the SVUF is reduced by

Table 4.8 Non-dominant solutions for placement of one FLIG in the 19-bus URDS

Location	FLIG Sizes (kW)	Reactive Power Loss (kVAR)	Real Power Loss (kW)	SVUF
10	257	0.4899	1.1386	0.1218
11	242	0.5271	1.2250	0.1176

64%, the reactive power loss is reduced by 77%, and the real power loss is reduced by 77%. The plot of the objective function at various buses for the weighted-factor-based approach is shown in Fig. 4.18. Table. 4.9 displays a comparison of results for all test scenarios.

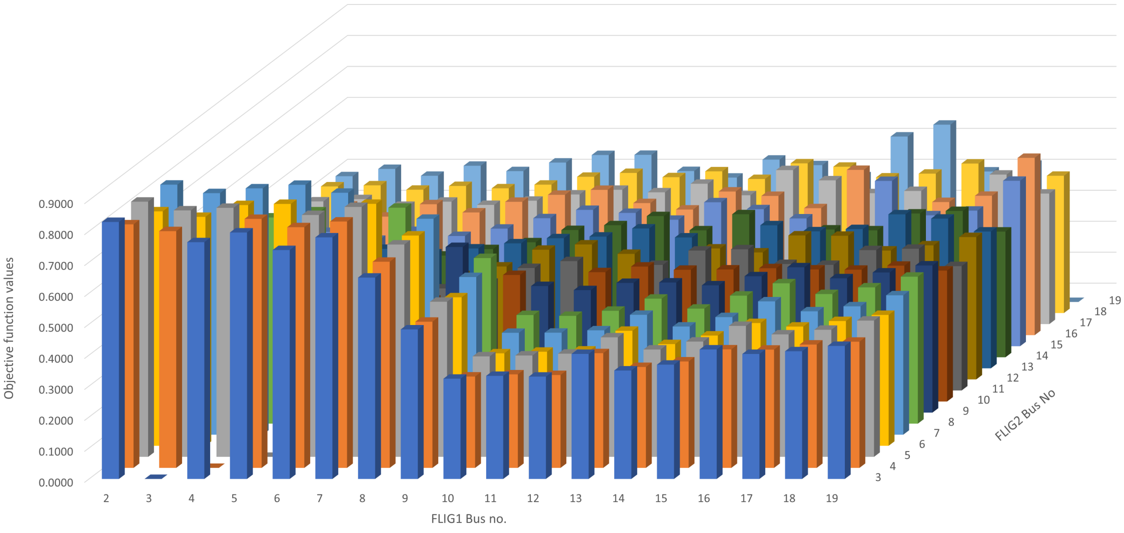

Fig. 4.18 Plotting of objective function for placement of two FLIGs in the 19-bus URDS using weighted factor-based MOPSO

Using Pareto front based MOPSO, the placement of two FLIGs results in two non-dominant solutions. Placing FLIGs of 123 kW and 215 kW at buses 6 and 10, respectively, yields the minimum real power loss, with SVUF, reactive power loss, and real power loss of 0.0662, 0.4214 kVAR, and 0.9795 kW, respectively. Placing FLIGs of 130 kW and 220 kW at buses 4 and 10, respectively, provides the maximum reduction in SVUF, with SVUF, reactive power loss, and real power loss of 0.0668, 0.4221 kVAR, and 0.9810 kW, respectively. The numerical findings and Pareto front of non-dominant solutions can be found in Table. 4.10 and Fig. 4.19, respectively.

Table 4.9 Comparison of results for placement of FLIGs in 19-bus URDS

	Without FLIG	With One FLIG	With Two FLIGs
Location	—	11	4 & 10
FLIG size (kW)	—	242	130 & 220
Real Power Loss (kW)	4.24	1.23	0.98
Reactive Power Loss (kVAR)	1.83	0.53	0.42
SVUF	0.1863	0.1176	0.0668

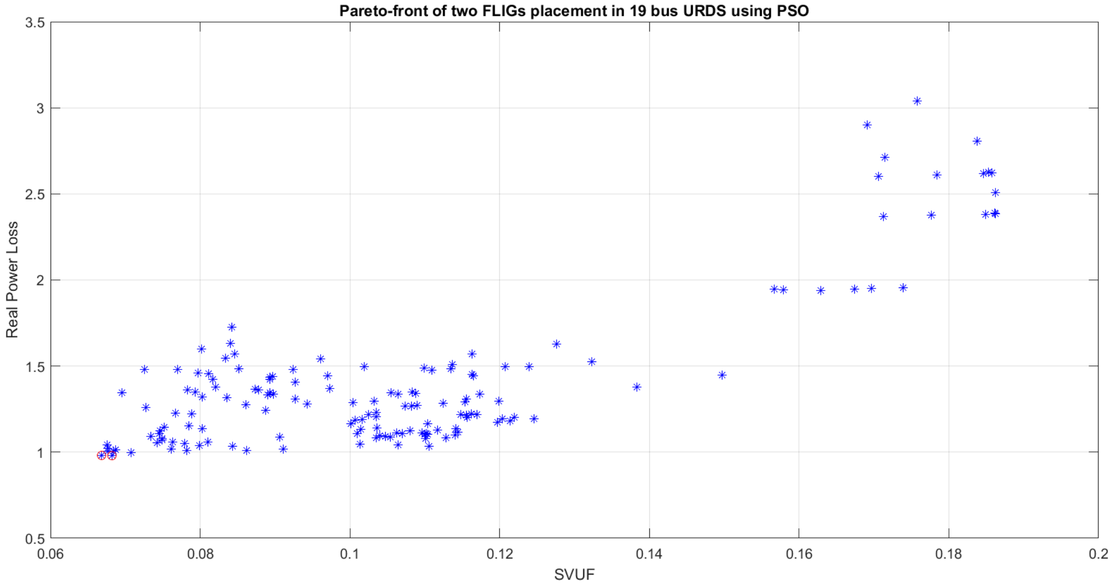

Fig. 4.19 Pareto front for placement of two FLIGs in the 19-bus URDS

Table 4.10 Non-dominant solutions for placement of two FLIGs in the 19-bus URDS

Location	FLIG Sizes (kW)	Reactive Power Loss (kVAR)	Real Power Loss (kW)	SVUF
4 & 10	130 & 220	0.4221	0.9810	0.0668
6 & 10	123 & 215	0.4214	0.9795	0.0682

4.5.4 Case Study IV: IEEE 34-bus system

The next test system is a IEEE 34-bus URDS, illustrated in Fig. A.5. The system's total load is 1399.5 kW and 851.69 kVAR. The SVUF, reactive power loss, and real power loss in the base case are 25.20, 198.21 kVAR, and 290.69 kW, respectively.

Optimal placement of one FLIG

The best location for one FLIG has been found using a weighted-factor approach to be bus-23. The optimal FLIG size is determined to be 1433 kW. The real power loss is determined to be 125.39 kW, the reactive power loss is determined to be 93.83 kVAR, and the SVUF is determined to be 3.4078. The placement of one FLIG reduces real power loss by 56.86%, reactive power loss by 52.66%, and SVUF by 86.48%. Fig. 4.20 depicts the objective function plot at various buses for the weighted-factor-based approach.

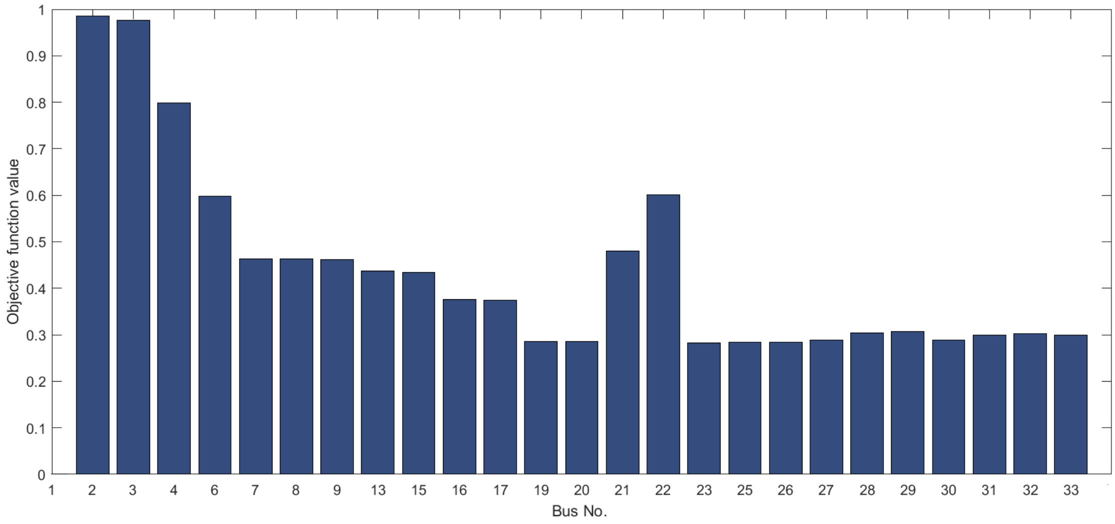

Fig. 4.20 Plotting of objective function for placement of one FLIG in the 34-bus URDS using weighted factor-based MOPSO

The Pareto-based approach yields two non-dominant solutions. The Pareto front of non-dominant solutions is depicted in Fig. 4.21, and the numerical results are presented in Table. 4.11. When a 1433 kW FLIG is installed in bus-23, a minimum SVUF of 3.4078 is obtained. The real power loss is 125.39 kW, and the reactive power loss is 93.83 kVAR. Bus-25 is determined to be the optimal location for minimising real power loss. The optimal FLIG size has been found to be 1403 kW. The real power loss obtained is 124.21 kW, the reactive power loss obtained is 93.36 kVAR, and the SVUF obtained is 3.5173.

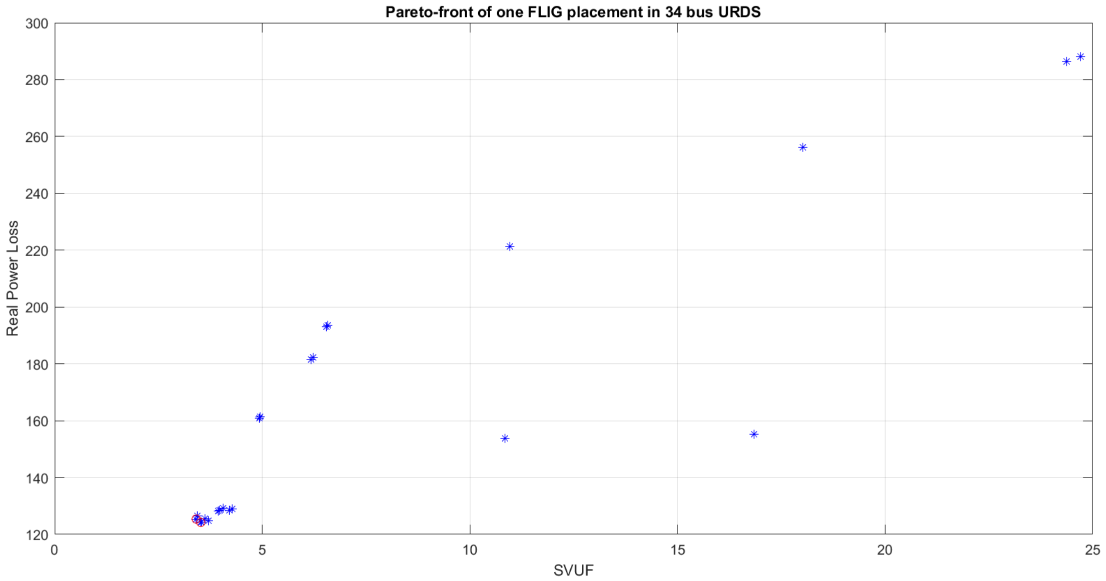

Fig. 4.21 Pareto front for placement of one FLIG in the 34-bus URDS

Table 4.11 Non-dominant solutions for placement of one FLIG in the 34-bus URDS

Location	FLIG Sizes (kW)	Reactive Power Loss (kVAR)	Real Power Loss (kW)	SVUF
23	1433	93.83	125.39	3.4078
25	1403	93.36	124.21	3.5173

4.6 Grey Wolf Optimization

The Grey Wolf Optimization (GWO) is a meta-heuristic technique for optimization problems that imitates the social hierarchy and hunting behavior of grey wolves [**?**]. The algorithm assigns alphas, betas, deltas, and omegas to represent the hierarchical structure of the pack. The alphas act as leaders who make decisions for the group, while betas serve as their subordinates and reinforce their commands. Deltas report to both alphas and betas, and omegas are followers with the lowest rank. In the GWO algorithm, the alpha represents the best solution, followed by beta and delta as the second and third best solutions, respectively. The optimization process is guided by these three wolves.

This method is an iterative computational process that involves wolves exploring a search area initially. As the process continues, the wolves gradually shift towards exploiting the search area until either the solution converges within a predetermined tolerance level or a fixed number of iterations is reached. In each iteration (t) of the process, the next coordinate of a wolf X is calculated using the positions of the alpha wolf, X_α, beta wolf, X_β, and delta wolf, X_δ. This is accomplished by utilizing eqns. (4.10) through (4.22), which are responsible for updating the positions of all the wolves.

$$A_1 = 2ar_1 - a \tag{4.10}$$
$$A_2 = 2ar_2 - a \tag{4.11}$$
$$A_3 = 2ar_3 - a \tag{4.12}$$
$$C_1 = 2r_4 \tag{4.13}$$
$$C_2 = 2r_5 \tag{4.14}$$
$$C_3 = 2r_6 \tag{4.15}$$
$$D_\alpha = |C_1 X_\alpha - X(t)| \tag{4.16}$$
$$D_\beta = |C_2 X_\beta - X(t)| \tag{4.17}$$
$$D_\delta = |C_3 X_\delta - X(t)| \tag{4.18}$$
$$X_1 = X_\alpha - A_1 D_\alpha \tag{4.19}$$
$$X_2 = X_\beta - A_1 D_\beta \tag{4.20}$$
$$X_3 = X_\delta - A_1 D_\delta \tag{4.21}$$
$$X(t+1) = \frac{X_1 + X_2 + X_3}{3} \tag{4.22}$$

Where, a is component which is linearly decreased from 2 to 0 as the iteration progress. r_1 through r_6 are random numbers between 0 and 1.

4.7 Proposed algorithm for placement and sizing of FLIGs using GWO

Step 1: Perform modified unbalanced load flow analysis discussed in Sec. 3.3 with ($P_{DG_1} = 0, \cdots, P_{DG_G} = 0$, $i_{inphase_1} = 0, \cdots, i_{inphase_G} = 0$, $i_{quadphase_1} = 0, \cdots, i_{quadphase_G} = 0$) . Where, G is the number of FLIGs that must be placed in G of the $N_{3\phi}$ buses of the microgrid.

Step 2: Calculate baseline $P_{Loss_{base}}$ and $SVUF_{base}$ of the microgrid.

Step 3: Generate all possible combinations of three-phase buses from the $N_{3\phi}$ buses, taking G three-phase buses at a time.

Step 4: Select the first combination of buses.

Step 5: (Applying GWO) Generate an initial population of wolves and randomly assign positions to each wolf. The dimensions of the search space are $[P_{DG_1}, \cdots, P_{DG_G}, i_{inphase_1}, \cdots, i_{inphase_G}, i_{quadphase_1}, \cdots, i_{quadphase_G}]$

Step 6: Set iteration counter to zero.

Step 7: Run the unbalanced load flow analysis for each wolf, and then determine the values of the objective function, real power loss, and SVUF. Test the constraints and discard the infeasible solutions.

Step 8: Update the best (X_α), second best (X_β) and third best (X_δ) positions.

Step 9: Modify the position of each wolf using eqns. (4.10) through (4.22).

Step 10: If the difference between the current iteration's best solution and the previous iteration's best solution is within the tolerance set or if a maximum number of iterations has been reached, continue on to Step 11; else, increase the iteration counter and repeat steps 7 to 10.

Step 11: Store the best solution and position for the current combination of buses along with the corresponding DG sizes, real power loss, SVUF and objective function value.

Step 12: If the current bus combination is not equal to the last combination of buses, select the next combination of buses and repeat steps 5 to 12 else continue to step 13.

Step 13: For weighted factor-based optimization, find the combination of buses for which the objective function given in eqn. (4.2) is minimum. For the Pareto-based approach find all the combinations of buses for which eqn. (4.3) has non-dominant solutions.

Step 14: Report.

4.8 GWO simulation results and analysis

The proposed GWO method has been employed on the 25-bus URDS and 19-bus URDS and tested for two different scenarios. The installation of one FLIG is examined first, followed by the installation of two FLIGs. The parameter settings for GWO is given in Table. 4.12.

Table 4.12 Parameter settings for GWO

a	*population*	*max iteration*
2	50	1000

4.8.1 Case Study I: 25-bus system

Optimal placement of one FLIG

The optimal placement of one FLIG is determined to be at bus 7 with a size of 1890 kW using the weighted factor-based GWO method. With one FLIG at bus 7, the observed SVUF is 2.49, the reactive power loss is 76.22 KVAR and real power loss is 67.67 kW. The results obtained from GWO and MOPSO are found to be identical in this case. When compared with Bhimarasetti et al.'s method [**?**], the proposed approach results in a reduction of 54.43% in reactive power loss, 54.94% in real power loss, and 74.06% in SVUF. Thus, both GWO and MOPSO demonstrate the advantages of the proposed approach.

The application of Pareto-based GWO to one FLIG placement yields three non-dominant solutions. The numerical findings are presented in Table. 4.13, and the Pareto front of the non-dominant solutions is depicted in Fig. 4.22. The obtained results are again found to be identical to those obtained using MOPSO. Therefore, both methods verify that the optimal location for maximum reduction in active power loss is bus-6, while for SVUF, bus-3 is the ideal location, and for a compromised solution, bus-7 is the optimal location. The convergence plot of GWO for real power minimization and VUF minimization at bus 2 is shown in Fig. 4.23 and Fig. 4.24, respectively.

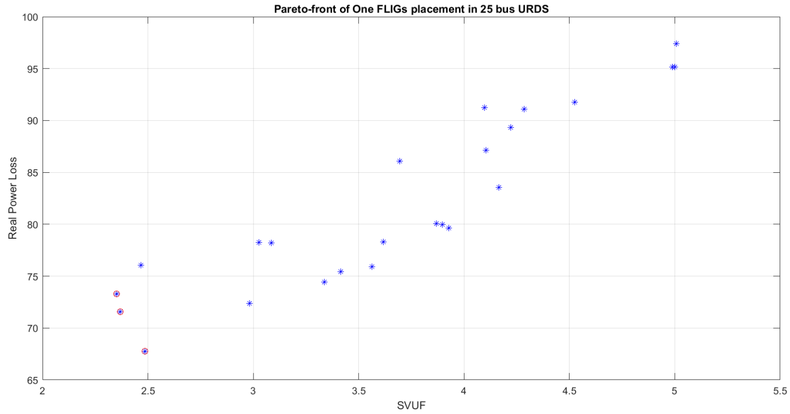

Fig. 4.22 Pareto front for one FLIG placement in the 25-bus URD using GWO

Optimal placement of two FLIGs

The placement of two FLIGs in the 25-bus system is investigated next. The optimal locations for installing two FLIGs, determined using a weighted factor-based GWO is found to be bus 7 and 18. The total SVUF, reactive power loss, and real power loss were found to be 0.81, 54.67 kVAR, and 50.30 kW, respectively.

From the results, it can be observed that the reduction in SVUF, reactive power loss, and real power loss achieved by installing two FLIGs is comparatively higher than

Table 4.13 Non-dominant solutions for placement of one FLIG in the 25-bus URDS using GWO

Location	FLIG Size (kW)	Reactive Power Loss (kVAR)	Real Power Loss (kW)	SVUF
3	2830	72.78	73.29	2.35
6	2296	76.41	71.57	2.37
7	1890	76.22	67.77	2.49

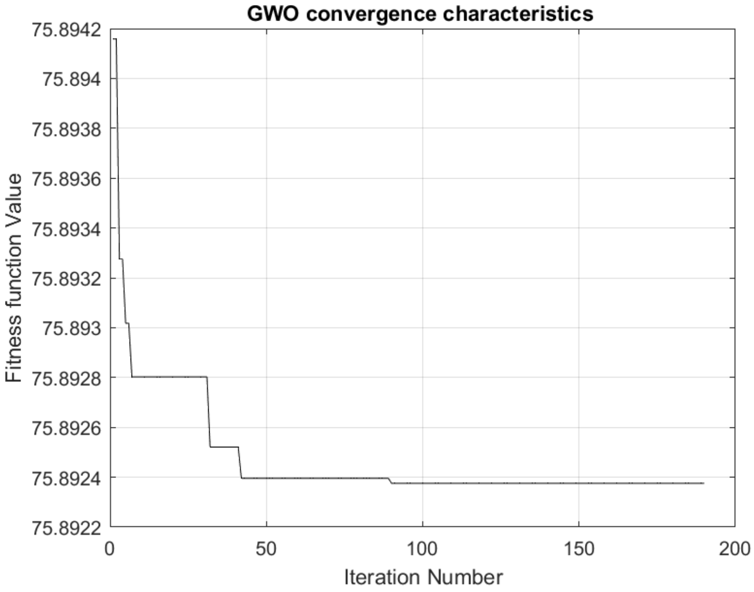

Fig. 4.23 GWO convergence plot with one FLIG in a 25-bus system for active power loss minimization

the reduction achieved by installing only one. Table 4.14 presents a comparison of the results for all the test scenarios.

Using Pareto front-based GWO, the placement of two FLIGs results in three non-dominant solutions. Placing FLIGs of 1502 kW and 1389 kW at buses 7 and 18, respectively, yields the minimum real power loss, with SVUF, reactive power loss, and real power loss of 0.81, 54.67 kVAR, and 50.30 kW, respectively. Placing FLIGs of 2022 kW and 1166 kW at buses 3 and 9, respectively, provides the maximum reduction in SVUF, with SVUF, reactive power loss, and real power loss of 0.75, 55.47 kVAR, and 52.40 kW, respectively. The optimal compromise solution, with FLIGs of 1853 kW and 1417 kW placed at buses 3 and 7, respectively, results in SVUF, reactive power loss, and real power loss of 0.76, 54.95 kVAR, and 51.82 kW, respectively. The numerical findings and Pareto front of non-dominant solutions is shown in Table. 4.15 and Fig. 4.25, respectively.

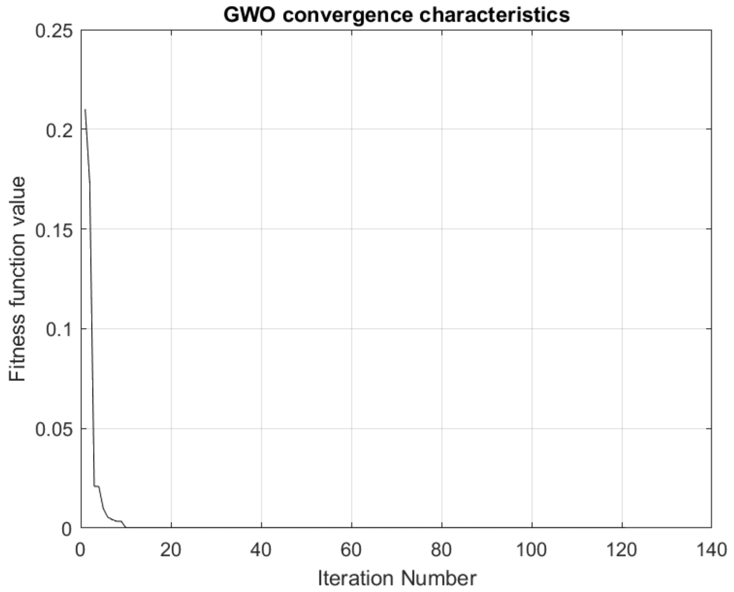

Fig. 4.24 GWO convergence plot with one FLIG in a 25-bus system for VUF minimization

Table 4.14 Comparison of results for all test scenarios in 25-bus URDS using GWO

	Without FLIG	With One FLIG using GWO	With Two FLIGs using PSO	With Two FLIGs using GWO
Location	—	7	7 & 18	7 & 18
DG size (kW)	—	1890	1503 & 1388	1502 & 1389
Real Power Loss (kW)	150.12	67.77	50.30	50.30
Reactive Power Loss (kVAR)	167.28	76.22	54.67	54.67
SVUF	8.34	2.49	0.80	0.81

Table 4.15 Non-dominant solutions for placement of two FLIGs in the 25-bus URDS using GWO

Location	FLIG Sizes (kW)	Reactive Power Loss (kVAR)	Real Power Loss (kW)	SVUF
3 & 7	1853 & 1417	54.95	51.82	0.76
3 & 9	2022 & 1166	55.47	52.40	0.75
7 & 18	1502 & 1389	54.67	50.30	0.81

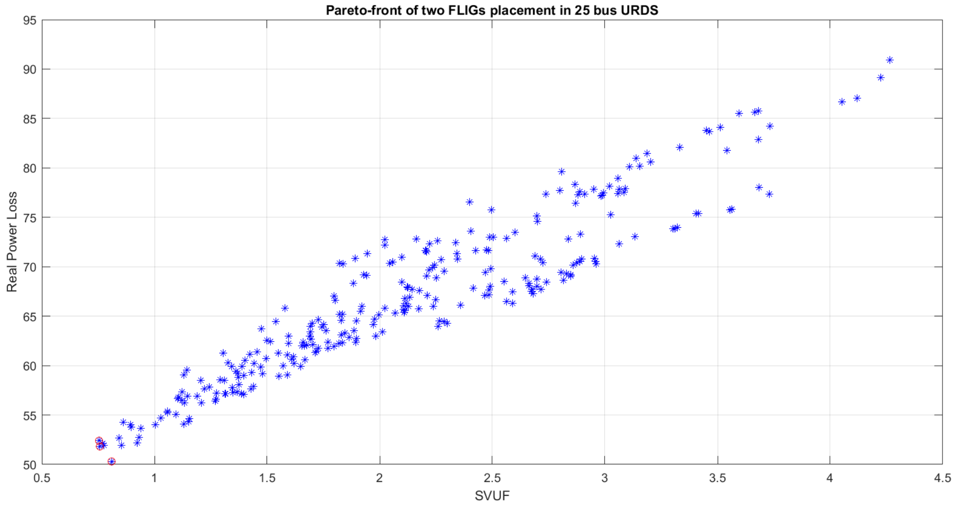

Fig. 4.25 Pareto front for placement of two FLIGs in the 25-bus URDS using GWO

The convergence plot of GWO for active power minimization is presented in Fig. 4.26, and the convergence plot for SVUF minimization is shown in Fig. 4.27.

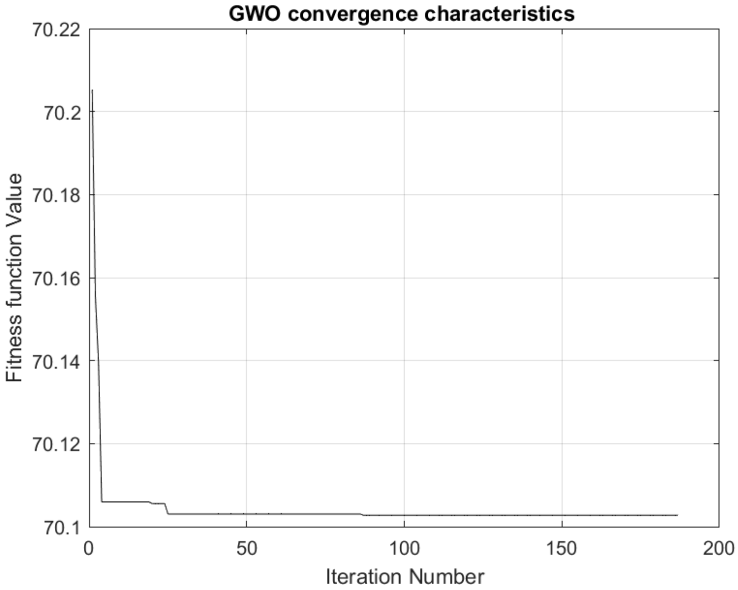

Fig. 4.26 Convergence plot of GWO for active power loss minimization with two FLIG in a 25-bus system

When considering the placement of two FLIGs, there are non-significant differences in the results obtained using the MOPSO and GWO methods. However, it was observed that the convergence rate of GWO is faster than that of MOPSO.

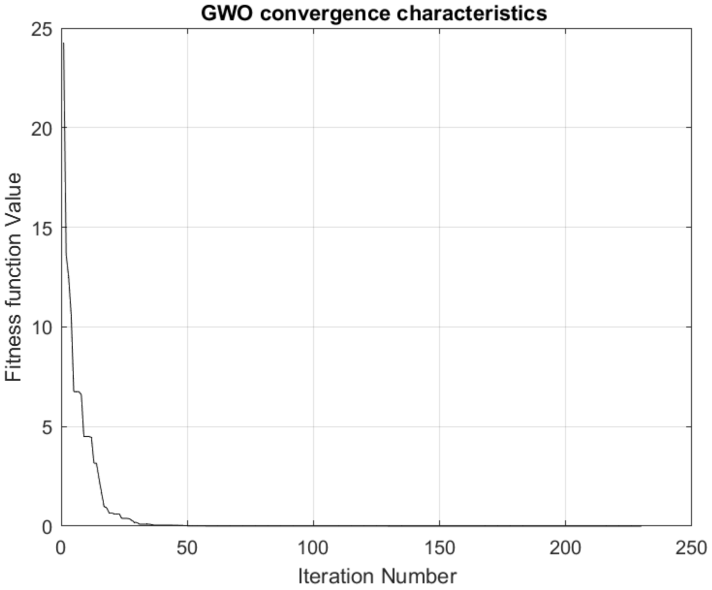

Fig. 4.27 Convergence plot of GWO for VUF minimization with two FLIG in a 25-bus system

4.8.2 Case Study II: 19-bus system

Optimal placement of one FLIG

The optimal placement of one FLIG is determined to be at bus 11 with a size of 242 kW using the weighted factor-based GWO method. With one FLIG at bus 11, the observed SVUF is 0.1176, the reactive power loss is 0.53 KVAR and real power loss is 1.23 kW. The placement of one FLIG reduces real power loss by 71%, reactive power loss by 71%, and SVUF by 37%. The results obtained from GWO and MOPSO are found to be identical in this case.

The Pareto-based approach yields three non-dominant solutions. The Pareto front of non-dominant solutions is depicted in Fig. 4.28, and the numerical results are presented in Table. 4.16. When a 231 kW FLIG is installed in bus-14, a minimum SVUF of 0.1175 is obtained. The real power loss is 1.34 kW, and the reactive power loss is 0.58 kVAR. Bus-10 is determined to be the optimal location for minimising real power loss. The optimal FLIG size has been found to be 257 kW. The real power loss obtained is 1.14 kW, the reactive power loss obtained is 0.49 kVAR, and the SVUF obtained is 0.1214. The best compromise solution is obtained when an FLIG of 242 kW is installed in bus-11. The SVUF is determined to be 0.1176, real power loss is determined to be 1.23 kW, and the reactive power loss is determined to be 0.53 kVAR.

Using GWO three non-dominant solutions are obtained, while using PSO two non-dominant solutions are obtained. However, for minimum SVUF as can be seen from the Table. 4.16 both bus-11 and bus-14 are suitable, as the difference in SVUF for these two buses are negligible.

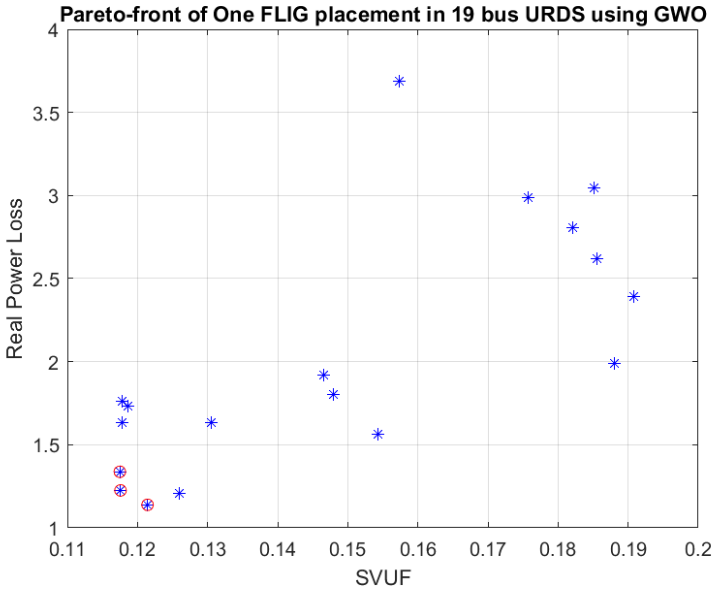

Fig. 4.28 Pareto front for one FLIG placement in the 19-bus URD using GWO

Table 4.16 Non-dominant solutions for placement of one FLIG in the 19-bus URDS using GWO

Location	FLIG Sizes (kW)	Reactive Power Loss (kVAR)	Real Power Loss (kW)	SVUF
10	257	0.49	1.14	0.1218
11	242	0.53	1.23	0.1176
14	231	0.58	1.34	0.1175

Optimal placement of two FLIGs

Using the weighted factor based approach, bus-4 and bus-10 are determined to be the ideal locations for the installation of two FLIGs. FLIG 1 and FLIG 2 have optimal sizes of 130 kW and 220 kW, respectively. The obtained SVUF is 0.0660, the reactive power is 0.4221, and the real power is 0.9810. The locations and sizes obtained by both methods, namely PSO and GWO, are identical. This verifies the accuracy of the obtained results.

Using Pareto front-based GWO, the placement of two FLIGs yields two non-dominant solutions. Placing FLIGs of 123 kW and 215 kW at buses 6 and 10, respectively, results in the lowest real power loss, with SVUF, reactive power loss, and real power loss of 0.0699, 0.4214 kVAR, and 0.9795 kW, respectively. Placing FLIGs of 130 kW and 220 kW at buses 4 and 10, respectively, results in the greatest reduction in SVUF, with SVUF, reactive power loss, and real power loss of 0.0660, 0.4221 kVAR, and 0.9810 kW, respectively. The numerical results and Pareto front of non-dominant solutions are shown in Table. 4.17 and Fig. 4.29, respectively.

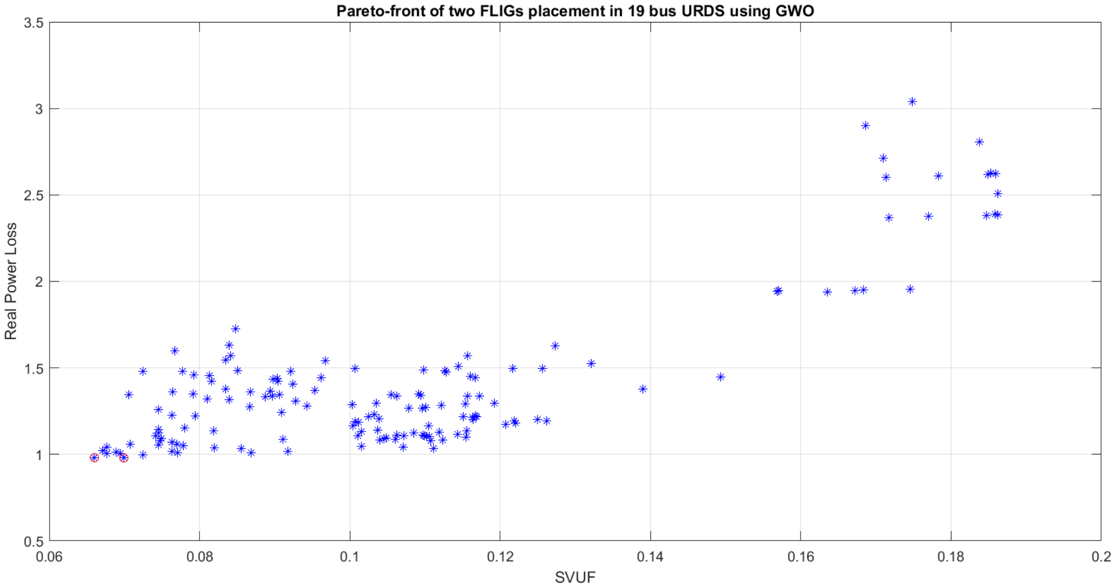

Fig. 4.29 Pareto front for placement of two FLIGs in the 19-bus URDS using GWO

Table 4.17 Non-dominant solutions for placement of two FLIGs in the 19-bus URDS using GWO

Location	FLIG Sizes (kW)	Reactive Power Loss (kVAR)	Real Power Loss (kW)	SVUF
4 & 10	130 & 220	0.4221	0.9810	0.0660
6 & 10	123 & 215	0.4214	0.9795	0.0699

4.9 Discussion

The following are the findings of the simulations:

- Deployment of FLIGs with unbalanced voltage correction leads to a significant reduction in voltage unbalance across all buses and a decrease in distribution losses.
- As the number of FLIGs is increased, the reduction in distribution losses and SVUF is more pronounced.

- The weighted factor-based approach allows the operator to give weightage to objectives and obtain a single solution to the optimization problem.
- The Pareto front-based approach provides all non-dominant solutions, allowing the network operator to choose locations that maximize reduction in real power loss, reduction in SVUF, or a compromise between the two objectives.
- Both PSO and GWO techniques are able to provide the results within the set iteration limit. Further, the GWO is able to converge faster than PSO.

The results demonstrate that four-leg inverters are a better choice for integrating DGs into an unbalanced microgrid. Although the FLIGs can be placed in any of the three phase buses, however, optimal placement of FLIGs can maximize the reduction in distribution losses and voltage unbalances. The proposed method can determine the best locations and FLIG sizes for any test systems and all test scenarios.

4.10 Conclusion

This chapter proposes two optimization approach based on MPSO and GWO to determine the optimal placement and rating of FLIGs in a microgrid. There are two objectives: finding the positions and DG ratings for which the real power distribution loss is lowest, and finding locations in the microgrid where if the FLIGs are placed and P&O applied, the total voltage unbalances are at their lowest levels. Two approaches are used to achieve the optimisation: first, a weighted factor-based approach is employed to find a distinct solution based on the relative importance of each objective. Second, all the non-dominated options are gathered using a Pareto-based approach so that a particular solution can be selected based on preference. The algorithm is tested on four unbalanced radial distribution systems, with simulations conducted for two scenarios. The first scenario involves analyzing the installation of one FLIG, while the second scenario studies the installation of two FLIGs. The study evaluates the effects of FLIG placement on network metrics such as SVUF, reactive power loss, and real power loss. Results obtained from both PSO and GWO are found to be similar in most cases, with few cases in which the results obtained are different but the difference obtained is negligible.

5

Conclusion

Voltage unbalance is one of the most significant operational issues in a low-voltage microgrid. The source of the voltage unbalance can be attributed to the presence of single-phase loads unequally distributed among the phases. Unbalanced three-phase loads and faulty equipment also contributes to voltage unbalance.

A comprehensive study of the available literature reveals several techniques for mitigating voltage unbalance. One straightforward technique involves installing devices such as active shunt or series filters, STATCOM, etc. However, these methods are often cost-inefficient and most of the time remain underutilized. Other methods involve unequal power injection into heavily loaded phases or drawing more power from lightly loaded phases. However, these methods require additional complex hardware. Unbalance voltage compensation through demand response management has also been proposed, but these methods heavily rely on consumer participation. There are techniques involving the injection of negative sequence current using suitable inverters. However, these existing methods require the installation of additional hardware or communication among DGs. Taking all these factors into consideration, this work aims to develop a simple, reliable, and effective unbalance voltage compensation technique suitable for four-leg inverter-interfaced distributed generators. The objective is to devise a straightforward and cost-effective technique that can be implemented using existing hardware without any modifications.

The compensation for unbalance voltage is achieved by injecting negative sequence current into the microgrid at the point of inverter connection. The reference for negative sequence current is generated by summing two orthogonal components of negative sequence current. The system is perturbed in four orthogonal directions, and the resulting VUFs are observed. The system is then shifted to the point where the minimum VUF is observed, and the perturbation and observation process is continued until the system remains close to the minimum VUF. A control strategy is developed and validated to implement the P&O technique. Additionally, a comprehensive guide is provided for developing a Simulink model for three-dimensional space vector modulation. It is worth mentioning that the impact of placing the FLIGs at different buses of the microgrid on VUFs has not been previously investigated.

The optimal placement of FLIGs has a significant effect on the degree of voltage correction achieved. Therefore, algorithms based on particle swarm optimization and grey wolf optimization techniques are employed to determine the ideal locations for installing FLIGs, where the active power loss and the SVUF are minimized. Furthermore, the sizing of the DGs is also determined.

Future scope of the work: The proposed P&O method can be implemented on grid to vehicle and vehicle to grid charging systems to reduce the voltage unbalance by injecting negative sequence current into the microgrid or absorbing negative sequence from the grid. In a similar manner, the method proposed in the this work can be implemented on energy storage systems and its effect can be investigated. Additionally, alternative optimization techniques can be explored to address the issue of FLIG placement for improving VUFs in unbalanced distribution systems. While this work focuses on MATLAB simulations for reducing VUFs using the P&O method, there is potential for developing hardware systems for the FLIGs proposed in this research.

A

To investigate the validity and performance of the proposed work in this thesis, simulation were carried out on four radial distribution systems with unbalanced loading conditions. Further, three types of loads are considered during simulation of the distribution networks. The types of load considered are given below.

- Constant power load.
- Constant current load.
- Constant impedance load.

A.1 Generalized expression for three phase constant power load, constant current load and constant impedance load

The expression for the complex load for a bus q is given as $S_{L_q} = P_{L_q} + jQ_{L_q}$, in terms of V_q, V_{q0} and $S_{L_{q0}} = P_{L_{q0}} + jQ_{L_{q0}}$. Where, V_q is the voltage at bus-q during the load flow iterations, V_{q0} is the base case assigned voltage for the bus-q and $S_{L_{q0}}$ is the base case complex load assigned at bus-q. Eqns. (A.1) and (A.2) represent the expression for complex star and delta connected load respectively [**?**].

$$\begin{bmatrix} S_{L_q}^{a} \\ S_{L_q}^{b} \\ S_{L_q}^{c} \end{bmatrix} = \begin{bmatrix} S_{L_{q0}}^{a}\left(\frac{V_q^{a}}{V_{q0}^{a}}\right)^{n} \\ S_{L_{q0}}^{b}\left(\frac{V_q^{b}}{V_{q0}^{b}}\right)^{n} \\ S_{L_{q0}}^{c}\left(\frac{V_q^{c}}{V_{q0}^{c}}\right)^{n} \end{bmatrix} \tag{A.1}$$

$$\begin{bmatrix} S_{L_q}^{ab} \\ S_{L_q}^{bc} \\ S_{L_q}^{ca} \end{bmatrix} = \begin{bmatrix} S_{L_{q0}}^{ab}\left(\frac{V_q^{ab}}{V_{q0}^{ab}}\right)^{n} \\ S_{L_{q0}}^{bc}\left(\frac{V_q^{bc}}{V_{q0}^{bc}}\right)^{n} \\ S_{L_{q0}}^{ca}\left(\frac{V_q^{ca}}{V_{q0}^{ca}}\right)^{n} \end{bmatrix} \tag{A.2}$$

Where, $n = 0, 1$ and 2 for loads with constant power, current, and impedance, respectively.

The current at a bus q is then calculated using eqn. (A.3) for star-connected loads, and eqn. (A.4) for delta-connected loads during load flow iteration steps.

$$\begin{bmatrix} I_{L_q}^{a} \\ I_{L_q}^{b} \\ I_{L_q}^{c} \end{bmatrix} = \begin{bmatrix} \left(\frac{S_{L_q}^{a}}{V_q^{a}}\right)^{*} \\ \left(\frac{S_{L_q}^{b}}{V_q^{b}}\right)^{*} \\ \left(\frac{S_{L_q}^{c}}{V_q^{c}}\right)^{*} \end{bmatrix} \tag{A.3}$$

$$\begin{bmatrix} I_{L_q}^{a} \\ I_{L_q}^{b} \\ I_{L_q}^{c} \end{bmatrix} = \begin{bmatrix} \left(\frac{S_{L_q}^{ab}}{V_q^{ab}}\right)^{*} - \left(\frac{S_{L_q}^{ca}}{V_q^{ca}}\right)^{*} \\ \left(\frac{S_{L_q}^{bc}}{V_q^{bc}}\right)^{*} - \left(\frac{S_{L_q}^{ab}}{V_q^{ab}}\right)^{*} \\ \left(\frac{S_{L_q}^{ca}}{V_q^{ca}}\right)^{*} - \left(\frac{S_{L_q}^{bc}}{V_q^{bc}}\right)^{*} \end{bmatrix} \tag{A.4}$$

A.2 Backward-forward sweep based unbalanced load flow algorithm

Algorithm for the basic backward-forward sweep based load flow analysis for an unbalanced radial system is provided below.

Step 1: Input line data (which includes line impedance and line charging) and base case load data.

Step 2: Initialize voltage at each bus to the nominal value.

Step 3: Set iteration count to zero and allowable maximum iteration.

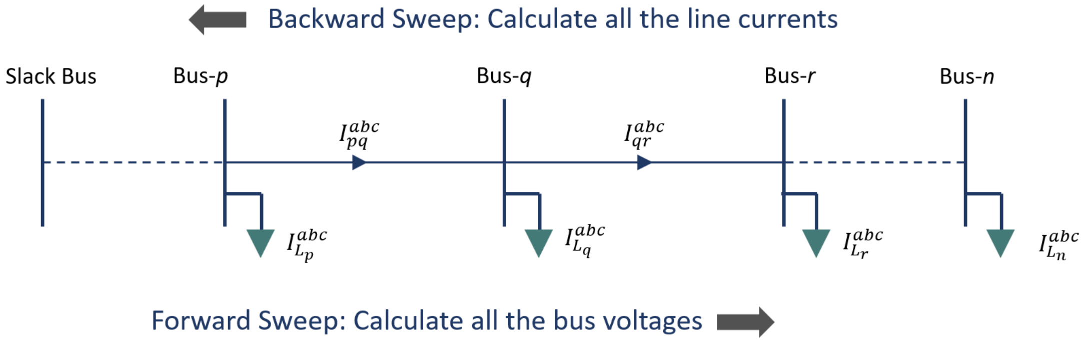

Fig. A.1 Section of an unbalanced radial distribution system.

Step 4: Calculate load current, ${I_{L_q}}^{abc}$ at each bus using eqn.(A.5) for star-connected load and using eqn. (A.6) for delta connected load.

$$\begin{bmatrix} I_{L_q}^a \\ I_{L_q}^b \\ I_{L_q}^c \end{bmatrix} = \begin{bmatrix} \left(\frac{S_{L_q}^a}{V_q^a}\right)^* \\ \left(\frac{S_{L_q}^b}{V_q^b}\right)^* \\ \left(\frac{S_{L_q}^c}{V_q^c}\right)^* \end{bmatrix} \tag{A.5}$$

$$\begin{bmatrix} I_{L_q}^a \\ I_{L_q}^b \\ I_{L_q}^c \end{bmatrix} = \begin{bmatrix} \left(\frac{S_{L_q}^{ab}}{V_q^{ab}}\right)^* - \left(\frac{S_{L_q}^{ca}}{V_q^{ca}}\right)^* \\ \left(\frac{S_{L_q}^{bc}}{V_q^{bc}}\right)^* - \left(\frac{S_{L_q}^{ab}}{V_q^{ab}}\right)^* \\ \left(\frac{S_{L_q}^{ca}}{V_q^{ca}}\right)^* - \left(\frac{S_{L_q}^{bc}}{V_q^{bc}}\right)^* \end{bmatrix} \tag{A.6}$$

Step 5: Calculate the line charging current, $I_{sh_{pq}}^{abc}$ at bus-q for the line between bus-p and bus-q using eqn. (A.7)

$$[I_{sh_{pq}}^{abc}] = \frac{1}{2}[Y_{sh_{pq}}][V_q^{abc}] \tag{A.7}$$

Where, $Y_{sh_{pq}}$ is the shunt admittance matrix of the line between bus-p and bus-q given by eqn. (A.8)

$$Y_{sh_{pq}} = \begin{bmatrix} -\left(y_{pq}^{aa} + y_{pq}^{ab} + y_{pq}^{ac}\right) & y_{pq}^{ab} & y_{pq}^{ac} \\ y_{pq}^{ba} & -\left(y_{pq}^{ba} + y_{pq}^{bb} + y_{pq}^{bc}\right) & y_{pq}^{bc} \\ y_{pq}^{ca} & y_{pq}^{cb} & -\left(y_{pq}^{ca} + y_{pq}^{cb} + y_{pq}^{cc}\right) \end{bmatrix} \tag{A.8}$$

Step 6: Calculate the total line charging current, $I_{sh_q}^{abc}$ at bus-q using eqn. (A.9)

$$\begin{bmatrix} {I_{sh_q}}^a \\ {I_{sh_q}}^b \\ {I_{sh_q}}^c \end{bmatrix} = \begin{bmatrix} \sum\limits_{qm=1}^{M} {I_{sh_{qm}}}^a \\ \sum\limits_{qm=1}^{M} {I_{sh_{qm}}}^b \\ \sum\limits_{qm=1}^{M} {I_{sh_{qm}}}^c \end{bmatrix} \tag{A.9}$$

Where, qm is a line directly connected to bus-q and M is the total number of such lines.

Step 7: Calculate the total current at bus-q using (A.10).

$$\begin{bmatrix} I_q^a \\ I_q^b \\ I_q^c \end{bmatrix} = \begin{bmatrix} {I_{L_q}}^a \\ {I_{L_q}}^b \\ {I_{L_q}}^c \end{bmatrix} + \begin{bmatrix} {I_{sh_q}}^a \\ {I_{sh_q}}^b \\ {I_{sh_q}}^c \end{bmatrix} \tag{A.10}$$

Step 8: (Backward Sweep) Starting from the radial network's last bus, calculate all the line currents upstream till slack bus using (A.11)

$$[I_{pq}]^{abc} = [I_q^{abc}] + \sum_{lm=1}^{M} [I_{lm}^{abc}] \tag{A.11}$$

Where, lm is a line directly connected to bus q downstream and M is the total number of such lines.

Step 9: (Forward Sweep) Starting from the slack bus and moving towards the last bus of the radial network, update the voltages of all the buses downstream using (A.12)

$$[V_q^{abc}] = [V_p^{abc}] - [Z][I_{pq}^{abc}] \tag{A.12}$$

Where, Z is the impedance matrix of the line between bus-p and bus-q.

$$Z = \begin{bmatrix} z_{pq}^{aa,n} & z_{pq}^{ab,n} & z_{pq}^{ac,n} \\ z_{pq}^{ba,n} & z_{pq}^{bb,n} & z_{pq}^{bc,n} \\ z_{pq}^{ca,n} & z_{pq}^{cb,n} & z_{pq}^{cc,n} \end{bmatrix} \tag{A.13}$$

Step 10: Compute the maximum error of voltage for all the buses during two successive iterations (i.e. the absolute value of voltage difference between the present and previous iteration for all buses). If the maximum error is greater than the set convergence criteria or if the number of iterations is less that the set maximum limit repeat steps 4 to 10. else goto step 11, provided that the load flow analysis converges. If the load flow iteration is terminated due to violation of maximum iteration limit terminate the load flow with warning message, "Load flow did not converge" and goto step 15.

Step 11: Calculate the real power and reactive power loss in phases a, b and c in each line T_{pq} by (A.14), (A.15), (A.16), (A.17), (A.18), and (A.19) respectively.

$$P^a_{L_{pq}} = \Re\Big\{V^a_p(I^a_{pq})^* - V^a_q(I^a_{qp})^*\Big\} \tag{A.14}$$

$$P^b_{L_{pq}} = \Re\Big\{V^b_p(I^b_{pq})^* - V^b_q(I^b_{qp})^*\Big\} \tag{A.15}$$

$$P^c_{L_{pq}} = \Re\Big\{V^c_p(I^c_{pq})^* - V^c_q(I^c_{qp})^*\Big\} \tag{A.16}$$

$$Q^a_{L_{pq}} = \Im\Big\{V^a_p(I^a_{pq})^* - V^a_q(I^a_{qp})^*\Big\} \tag{A.17}$$

$$Q^b_{L_{pq}} = \Im\Big\{V^b_p(I^b_{pq})^* - V^b_q(I^b_{qp})^*\Big\} \tag{A.18}$$

$$Q^c_{L_{pq}} = \Im\Big\{V^c_p(I^c_{pq})^* - V^c_q(I^c_{qp})^*\Big\} \tag{A.19}$$

Step 12: Calculate the total real power and reactive power loss in each line T_{pq} by (A.20) and (A.21).

$$P_{L_{pq}} = P^a_{L_{pq}} + P^b_{L_{pq}} + P^c_{L_{pq}} \tag{A.20}$$

$$Q_{L_{pq}} = Q^a_{L_{pq}} + Q^b_{L_{pq}} + Q^c_{L_{pq}} \tag{A.21}$$

Step 13: Calculate the total real power and reactive power loss of the system using (A.22) and (A.23).

$$P_{Loss} = \sum P_{L_{pq}} \tag{A.22}$$

$$Q_{Loss} = \sum Q_{L_{pq}} \tag{A.23}$$

Step 14: Report results.

Step 15: Stop.

A.3 25-bus unbalanced radial distribution system data

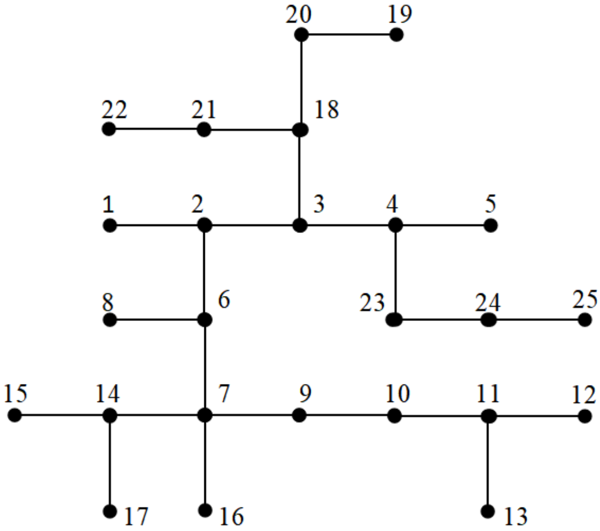

Fig. A.2 25-bus unbalanced radial distribution system single-line diagram.

Table A.1 25-bus unbalanced radial distribution system line and load data

Branch	Starting Node	Ending Node	Type of conductor	Length (km)	Receiving Node Load (kVA)		
					Phase a	Phase b	Phase c
1	1	2	1	1000	0	0	0
2	2	3	1	500	35 + j25	40 + j30	45 + j32
3	2	6	2	500	40 + j30	45 +j32	35 + j25
4	3	4	1	500	50 + j40	60 + j45	50 + j35
5	3	18	2	500	40 + j30	40 + j30	40 + j30
6	4	5	2	500	40 + j30	40 + j30	40 + j30
7	4	23	2	400	60 + j45	50 + j40	50 + j35
8	6	7	2	500	0	0	0
9	6	8	2	1000	40 + j30	40 + j30	40 + j30
10	7	9	2	500	60 + j45	50 + j40	50 + j35
11	7	14	2	500	50 + j35	50 + j40	60 + j45
12	7	16	2	500	40 + j30	40 + j30	40 + j30
13	9	10	2	500	35 + j25	40 + j30	45 + j32
14	10	11	2	300	45 + j32	35 + j25	40 + j30
15	11	12	2	200	50 + j35	60 + j45	50 + j40
16	11	13	3	200	35 + j25	45 + j32	40 + j30i
17	14	15	2	300	133.3 + j100	133.3 + j100	133.3 + j100
18	14	17	3	300	40 + j30	35 + j25	45 + j32
19	18	20	2	500	35 + j25	40 + j30	45 + j32
20	18	21	3	400	40 + j30	35 + j25	45 + j32
21	20	19	3	400	60 + j45	50 + j35	50 + j40
22	21	22	2	400	50 + j35	60 + j45	50 + j40
23	23	24	2	400	35 + j25	45 + j32	40 + j30
24	24	25	3	400	60 + j45	50 + j30	50 + j35

Table A.2 25-bus unbalanced radial distribution system line impedance details

Type	**Line impedance (ohms/mile)**		
1	0.3686 + j0.6852	0.0169 + j0.1515	0.0155 + j0.1098
	0.0169 + j0.1515	0.3757 + j0.6715	0.0188 + j0.2072
	0.0155 + j0.1098	0.0188 + j0.2072	0.3723 + j0.6782
2	0.9775 + j0.8717	0.0167 + j0.1697	0.0152 + j0.1264
	0.0167 + j0.1697	0.9844 + j0.8654	0.0186 + j0.2275
	0.0152 + j0.1264	0.0186 + j0.2275	0.9810 + j0.8648
3	1.9280 + j1.4194	0.0161 + j0.1183	0.0161 + j0.1183
	0.0161 + j0.1183	1.9308 + j1.4215	0.0161 + j0.1183
	0.0161 + j0.1183i	0.0161 + j0.1183	1.9337 + j1.4236

Table A.3 25-bus unbalanced radial distribution system base case load flow voltage profile

Bus	**Phase a**		**Phase b**		**Phase c**	
	Mag	**Angle**	**Mag**	**Angle**	**Mag**	**Angle**
1	1.0000	0.00	1.0000	-120.00	1.0000	120.00
2	0.9746	-0.48	0.9753	-120.35	0.9790	119.41
3	0.9677	-0.61	0.9687	-120.45	0.9734	119.25
4	0.9649	-0.67	0.9658	-120.51	0.9714	119.19
5	0.9637	-0.66	0.9644	-120.50	0.9704	119.19
6	0.9633	-0.48	0.9642	-120.31	0.9688	119.40
7	0.9544	-0.48	0.9551	-120.27	0.9605	119.38
8	0.9606	-0.48	0.9620	-120.29	0.9668	119.39
9	0.9500	-0.48	0.9510	-120.25	0.9565	119.37
10	0.9456	-0.47	0.9468	-120.22	0.9526	119.37
11	0.9436	-0.47	0.9449	-120.21	0.9507	119.36
12	0.9428	-0.47	0.9440	-120.21	0.9496	119.36
13	0.9429	-0.47	0.9442	-120.21	0.9500	119.36
14	0.9518	-0.48	0.9524	-120.26	0.9579	119.38
15	0.9512	-0.48	0.9520	-120.26	0.9574	119.38
16	0.9532	-0.48	0.9538	-120.26	0.9594	119.38
17	0.9509	-0.48	0.9513	-120.26	0.9569	119.38
18	0.9607	-0.61	0.9622	-120.43	0.9668	119.24
19	0.9577	-0.61	0.9593	-120.42	0.9634	119.24
20	0.9591	-0.61	0.9605	-120.42	0.9649	119.24
21	0.9573	-0.60	0.9594	-120.42	0.9635	119.25
22	0.9552	-0.60	0.9577	-120.42	0.9618	119.26
23	0.9623	-0.66	0.9631	-120.50	0.9691	119.19
24	0.9605	-0.66	0.9615	-120.51	0.9677	119.19
25	0.9585	-0.66	0.9599	-120.51	0.9660	119.19

Table A.4 25-bus unbalanced radial distribution system base case power flows

System			**Value**
Total input	kW	:	3355.9
	kVAr	:	2528.3
	kVA	:	4201.7
Total load	kW	:	3239.9
	kVAr	:	2393
	kVA	:	4027.8
Total losses	kW	:	116.03
	kVAr	:	135.29
	kVA	:	178.23

A.4 IEEE 13-bus unbalanced radial distribution system data

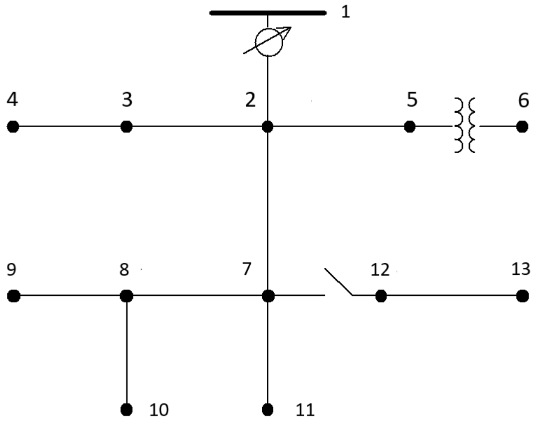

Fig. A.3 IEEE 13-bus unbalanced radial distribution system single-line diagram.

Table A.5 13-bus unbalanced radial distribution system line data

Branch	**Starting Node**	**Ending Node**	**Length (ft)**	**Type of conductor**
1	1	2	2000	1
2	2	7	2000	1
3	7	11	1000	1
5	12	13	500	6
6	7	8	300	4
7	8	9	300	5
8	8	10	800	7
9	2	5	500	2
11	2	3	500	3
12	3	4	300	3

Table A.6 13-bus unbalanced radial distribution system line impedance details

Type	**Line impedance (ohms/mile)**		
1	0.3465 + j1.0179	0.1560 + j0.5017	0.1580 + j0.4236
	0.1560 + j0.5017	0.3375 + j1.0478	0.1535 + j0.3849
	0.1580 + j0.4236	0.1535 + j0.3849	0.3414 + j1.0348
2	0.7526 + j1.1814	0.1580 + j0.4236	0.1560 + j0.5017
	0.1580 + j0.4236	0.7475 + j1.1983	0.1535 + j0.3849
	0.1560 + j0.5017	0.1535 + j0.3849	0.7436 + j1.2112
3	0.0000 + j0.0000	0.0000 + j0.0000	0.0000 + j0.0000
	0.0000 + j0.0000	1.3294 + j1.3471	0.2066 + j0.4591
	0.0000 + j0.0000	0.2066 + j0.4591	1.3238 + j1.3569
4	1.3238 + j1.3569	0.0000 + j0.0000	0.2066 + j0.4591
	0.0000 + j0.0000	0.0000 + j0.0000	0.0000 + j0.0000
	0.2066 + j0.4591	0.0000 + j0.0000	1.3294 + j1.3471
5	0.0000 + j0.0000	0.0000 + j0.0000	0.0000 + j0.0000
	0.0000 + j0.0000	0.0000 + j0.0000	0.0000 + j0.0000
	0.0000 + j0.0000	0.0000 + j0.0000	1.3292 + j1.3475
6	0.7982 + j0.4463	0.3192 + j0.0328	0.2849 + j0.0143
	0.3192 + j0.0328	0.7891 + j0.4041	0.3192 + j0.0328
	0.2849 + j0.0143	0.3192 + j0.0328	0.7982 + j0.4463
7	1.3425 + j0.5124	0.0000 + j0.0000	0.0000 + j0.0000
	0.0000 + j0.0000	0.0000 + j0.0000	0.0000 + j0.0000
	0.0000 + j0.0000	0.0000 + j0.0000	0.0000 + j0.0000

Table A.7 13-bus unbalanced radial distribution system line admittance details

Type	Line admittance (micro Siemens/mile)		
1	6.2998	-1.9958	-1.2595
	-1.9958	5.9597	-0.7417
	-1.2595	-0.7417	5.6386
2	5.6990	-1.0817	-1.6905
	-1.0817	5.1795	-0.6588
	-1.6905	-0.6588	5.4246
3	0.0000	0.0000	0.0000
	0.0000	4.7097	-0.8999
	0.0000	-0.8999	4.6658
4	4.6658	0.0000	-0.8999
	0.0000	0.0000	0.0000
	-0.8999	0.0000	4.7097
5	0.0000	0.0000	0.0000
	0.0000	0.0000	0.0000
	0.0000	0.0000	4.5193
6	96.8897	0.0000	0.0000
	0.0000	96.8897	0.0000
	0.0000	0.0000	96.8897
7	88.9912	0.0000	0.0000
	0.0000	0.0000	0.0000
	0.0000	0.0000	0.0000

Table A.8 13-bus unbalanced radial distribution system spot load data

Bus	Type of load	Load in kVA		
		Phase a	Phase b	Phase c
3	Y-PQ	0	170 +j125	0
4	D-Z	0	230 + j132	0
6	Y-PQ	160+j110	120 + j90	120 + j90
7	D-PQ	385 + j220	385 + j220	385 + j220
9	Y-I	0	0	170 + j80
10	Y-Z	128 + j86	0	0
12	D-I	0	0	170 + j151
13	Y-PQ	485 +j190	68 +j60	290 + j212

Table A.9 13-bus unbalanced radial distribution system distributed load data

Bus A	**Bus B**	**Type of load**	**Load in kVA**		
			Phase a	**Phase b**	**Phase c**
2	7	Y-PQ	17 + j10	66 + j38	117 +j68

Table A.10 13-bus unbalanced radial distribution system transformer data

Bus 1	**Bus 2**	**kVA**	**kV-high**	**kV-low**	**R%**	**X%**
5	6	500	4.16 – Gr.W	0.48 – Gr.W	1.1	2

Table A.11 13-bus unbalanced radial distribution system base case load flow voltage profile

Bus	**Phase a**		**Phase b**		**Phase c**	
	Mag	**Angle**	**Mag**	**Angle**	**Mag**	**Angle**
1	1.0000	0.00	1.0000	-120.00	1.0000	120.00
2	0.9498	-2.75	0.9839	-121.68	0.9300	117.80
3	-	-	0.9745	-121.86	0.9283	117.82
4	-	-	0.9729	-121.94	0.9264	117.87
5	0.9466	-2.82	0.9819	-121.73	0.9271	117.79
6	0.9207	-3.61	0.9624	-122.24	0.9064	117.22
7	0.9110	-5.90	0.9875	-122.21	0.8716	115.95
8	0.9093	-5.95	-	-	0.8683	115.91
9	-	-	-	-	0.8650	115.83
10	0.9042	-5.88	-	-	-	-
11	0.9110	-5.90	0.9875	-122.21	0.8716	115.95
12	0.9110	-5.90	0.9875	-122.21	0.8716	115.95
13	0.9028	-6.08	0.9886	-122.25	0.8675	116.08

Table A.12 13-bus unbalanced radial distribution system base case power flows

System			**Value**
Total input	kW	:	3527.6
	kVAr	:	2418.1
	kVA	:	4312.8
Total load	kW	:	3380.21
	kVAr	:	1984.66
	kVA	:	3919.78
Total losses	kW	:	147.39
	kVAr	:	433.44
	kVA	:	457.82

A.5 19-bus unbalanced radial distribution system data

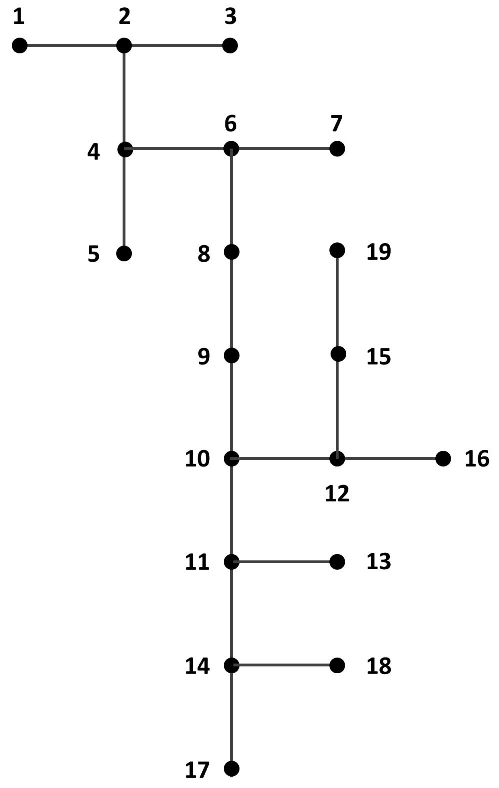

Fig. A.4 19-bus unbalanced radial distribution system single-line diagram.

Table A.13 19-bus unbalanced radial distribution system line and load data

Branch	Sending Node	Receiving Node	Type of conductor	Length (km)	Receiving Node Load (kVA)		
					Phase a	Phase b	Phase c
1	1	2	1	3	10.38 + j5.01	5.19 + j2.52	10.38 + j5.01
2	2	3	1	5	11.01 + j5.34	5.19 + j2.52	9.72 + j4.71
3	2	4	1	1.5	4.05 + j 1.95	5.67 + j2.76	6.48 + j3.15
4	4	5	1	1.5	6.48 + j3.15	5.19 + j2.52	4.53 + j2.19
5	4	6	1	1	4.20 + j2.04	3.09 + j1.50	2.91 + j1.41
6	6	7	1	2	9.72 + j4.71	8.10 + j3.93	8.10 + j3.93
7	6	8	1	2.5	7.44 + j3.60	5.34 + j2.58	3.39 + j1.65
8	8	9	1	3	12.3 + j5.97	14.91 + j7.23	13.29 + j6.42
9	9	10	1	5	3.39 + j1.65	4.20 + j2.04	2.58 + j1.26
10	10	11	1	1.5	7.44 + j3.60	7.44 + j3.60	11.01 + j5.34
11	10	12	1	1.5	9.72 + j4.71	8.10 + j3.93	8.10 + j3.93
12	11	13	1	5	4.38 + j2.13	5.34 + j2.58	6.48 + j3.15
13	11	14	1	1	3.09 + j1.50	3.09 + j1.50	4.05 + j1.95
14	12	15	1	5	4.38 + j2.13	4.86 + j2.34	6.96 + j3.36
15	12	16	1	6	7.77 + j3.78	10.38 + j5.01	7.77 + j3.78
16	14	17	1	3.5	6.48 + j3.15	4.86 + j2.34	4.86 + j2.34
17	14	18	1	4	5.34 + j2.58	5.34 + j2.58	5.52 + j2.67
18	15	19	1	4	8.76 + j4.23	10.05 + j4.86	7.14 + j3.45

Table A.14 19-bus unbalanced radial distribution system line impedance details

Type	Line impedance (ohms/km)		
1	1.5609 + j0.67155	0.5203 + j0.22385	0.5203 + j0.22385
	0.5203 + j0.22385	1.5609 + j0.67155	0.5203 + j0.22385
	0.5203 + j0.22385	0.5203 + j0.22385	1.5609 + j0.67155

Table A.15 19-bus unbalanced radial distribution system base case load flow voltage profile

Bus	Phase a		Phase b		Phase c	
	Mag	Angle	Mag	Angle	Mag	Angle
1	1.0000	0.00	1.0000	-120.00	1.0000	120.00
2	0.9959	0.01	0.9965	-119.99	0.9961	120.02
3	0.9952	0.00	0.9963	-119.99	0.9955	120.03
4	0.9943	0.01	0.9948	-119.99	0.9945	120.02
5	0.9941	0.01	0.9947	-119.99	0.9944	120.02
6	0.9933	0.01	0.9938	-119.99	0.9935	120.02
7	0.9930	0.01	0.9936	-119.99	0.9934	120.03
8	0.9912	0.02	0.9915	-119.98	0.9914	120.03
9	0.9889	0.03	0.9890	-119.97	0.9889	120.03
10	0.9858	0.03	0.9856	-119.96	0.9854	120.03
11	0.9854	0.03	0.9852	-119.96	0.9849	120.04
12	0.9853	0.04	0.9850	-119.96	0.9850	120.03
13	0.9852	0.03	0.9849	-119.95	0.9845	120.04
14	0.9852	0.03	0.9851	-119.95	0.9847	120.04
15	0.9847	0.04	0.9842	-119.95	0.9842	120.03
16	0.9849	0.04	0.9843	-119.96	0.9845	120.03
17	0.9849	0.03	0.9847	-119.95	0.9843	120.04
18	0.9850	0.03	0.9849	-119.95	0.9845	120.04
19	0.9843	0.04	0.9838	-119.95	0.9840	120.03

Table A.16 19-bus unbalanced radial distribution system base case power flows

System	Value		
Total input	kW	:	370.19
	kVAr	:	179.10
	kVA	:	411.23
Total load	kW	:	365.94
	kVAr	:	177.27
	kVA	:	406.62
Total losses	kW	:	4.24
	kVAr	:	1.83
	kVA	:	4.62

A.6 IEEE 34-bus unbalanced radial distribution system data

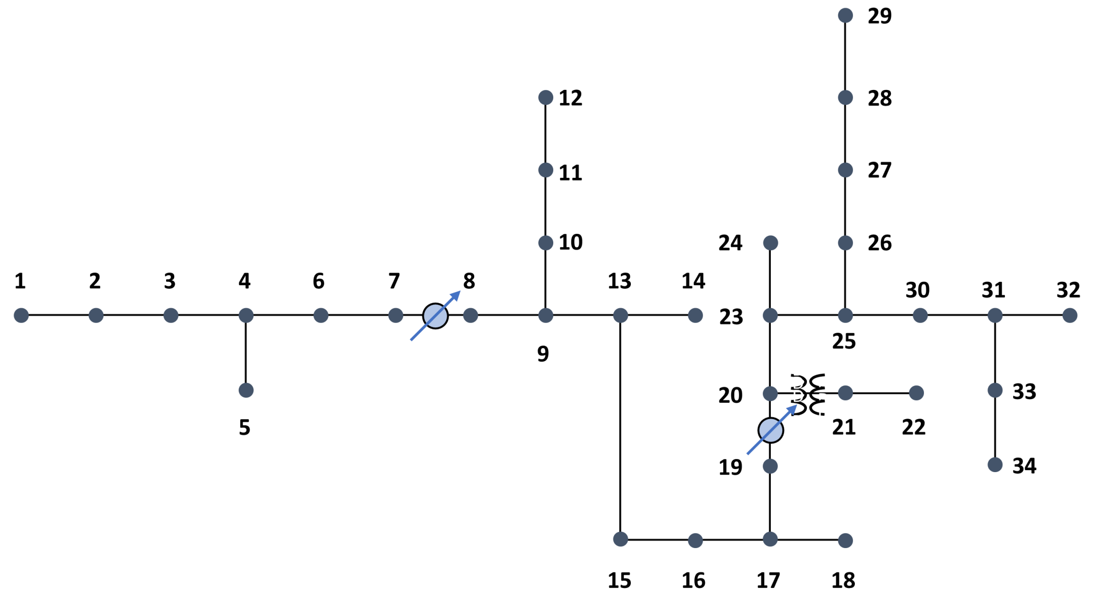

Fig. A.5 IEEE 34-bus unbalanced radial distribution system single-line diagram.

Table A.17 34-bus unbalanced radial distribution system line data

Branch	**Sending Node**	**Receiving Node**	**Length (ft)**	**Type of conductor**
1	1	2	2580	1
2	2	3	1730	1
3	3	4	32230	1
4	4	5	5804	4
5	4	6	37500	1
6	6	7	29730	1
7	7	8	10	2
8	8	9	310	2
9	9	10	1710	3
10	10	11	48150	3
11	11	12	13740	3
12	9	13	10210	2
13	13	14	3030	4
14	13	15	840	2
15	15	16	20440	2
16	16	17	520	2
17	17	18	23330	4
18	17	19	36830	2
19	19	20	10	2
20	20	21	0	XFM-1
21	21	22	10560	1
22	20	23	4900	2
23	23	24	1620	3
24	23	25	5830	2
25	25	26	280	2
26	26	27	1350	2
27	27	28	3640	2
28	28	29	530	2
29	25	30	2020	2
30	30	31	2680	2
31	31	32	860	2
32	31	33	280	2
33	33	34	4860	5

Table A.18 34-bus unbalanced radial distribution system line impedance details

Type	Line impedance (ohms/mile)		
1	1.3368 + j1.3343	0.2101 + j0.5779	0.2130 + j0.5015
	0.2101 + j0.5779	1.3238 + j1.3569	0.2066 + j0.4591
	0.2130 + j0.5015	0.2066 + j0.4591	1.3294 + j1.3471
2	1.9300 + j1.4115	0.2327 + j0.6442	0.2359 + j0.5691
	0.2327 + j0.6442	1.9157 + j1.4281	0.2288 + j0.5238
	0.2359 + j0.5691	0.2288 + j0.5238	1.9219 + j1.4209
3	2.7995 + j1.4855	0.0000 + j0.0000	0.0000 + j0.0000
	0.0000 + j0.0000	0.0000 + j0.0000	0.0000 + j0.0000
	0.0000 + j0.0000	0.0000 + j0.0000	0.0000 + j0.0000
4	0.0000 + j0.0000	0.0000 + j0.0000	0.0000 + j0.0000
	0.0000 + j0.0000	2.7995 + j1.4855	0.0000 + j0.0000
	0.0000 + j0.0000	0.0000 + j0.0000	0.0000 + j0.0000
5	0.0000 + j0.0000	0.0000 + j0.0000	0.0000 + j0.0000
	0.0000 + j0.0000	1.9217 + j1.4212	0.0000 + j0.0000
	0.0000 + j0.0000	0.0000 + j0.0000	0.0000 + j0.0000

Table A.19 34-bus unbalanced radial distribution system line admittance details

Type	Line admittance (micro Siemens/mile)		
1	5.3350	-1.5313	-0.9943
	-1.5313	5.0979	-0.6212
	-0.9943	-0.6212	4.8880
2	5.1207	-1.4364	-0.9402
	-1.4364	4.9055	-0.5951
	-0.9402	-0.5951	4.7154
3	4.2251	0.0000	0.0000
	0.0000	0.0000	0.0000
	0.0000	0.0000	0.0000
4	0.0000	0.0000	0.0000
	0.0000	4.2251	0.0000
	0.0000	0.0000	0.0000
5	0.0000	0.0000	0.0000
	0.0000	4.3637	0.0000
	0.0000	0.0000	0.0000

Table A.20 34-bus unbalanced radial distribution system spot load data

Bus	**Type of load**	**Load in kVA**		
		Phase a	**Phase b**	**Phase c**
30	Y-PQ	20 + j16	20 + j16	20 + j16
32	Y-I	9 + j7	9 + j7	9 + j7
27	Y-Z	135 + j105	135 + j105	135 + j105
29	D-PQ	20 + j16	20 + j16	20 + j16
22	D-I	150 + j75	150 + j75	150 + j75
16	D-Z	10 + j5	10 + j5	25 + j10

Table A.21 34-bus unbalanced radial distribution system distributed load data

Bus A	**Bus B**	**Type of load**	**Load in kVA**		
			Phase a	**Phase b**	**Phase c**
2	3	Y-PQ	0 + j 0	30 + j 15	25 + j 14
4	5	Y-I	0 + j 0	16 + j 8	0 + j 0
10	11	Y-Z	34 + j 17	0 + j 0	0 + j 0
11	12	Y-PQ	135 + j 70	0 + j 0	0 + j 0
9	13	D-I	0 + j 0	5 + j 2	0 + j 0
13	14	Y-I	0 + j 0	40 + j 20	0 + j 0
13	15	Y-PQ	0 + j 0	0 + j 0	4 + j 2
15	16	Y-PQ	7 + j 3	0 + j 0	0 + j 0
17	18	Y-PQ	0 + j 0	4 + j 2	0 + j 0
20	23	D-Z	7 + j 3	2 + j 1	6 + j 3
23	24	Y-PQ	2 + j 1	0 + j 0	0 + j 0
23	25	D-PQ	4 + j 2	15 + j 8	13 + j 7
25	30	D-Z	16 + j 8	20 + j 10	110 + j 55
30	31	D-PQ	30 + j 15	10 + j 6	42 + j 22
31	32	D-I	18 + j 9	22 + j 11	0 + j 0
33	34	Y-PQ	0 + j 0	28 + j 14	0 + j 0
26	27	Y-PQ	9 + j 5	0 + j 0	0 + j 0
27	28	Y-PQ	0 + j 0	25 + j 12	20 + j 11
28	29	Y-PQ	0 + j 0	23 + j 11	0 + j 0

Table A.22 34-bus unbalanced radial distribution system transformer data

Bus A	**Bus B**	**kVA**	**kV-high**	**kV-low**	**R%**	**X%**
20	21	500	24.9 – Gr.W	4.16 – Gr.W	1.9	4.08

Table A.23 34-bus unbalanced radial distribution system base case load flow voltage profile

Bus	**Phase a**		**Phase b**		**Phase c**	
	Mag	**Angle**	**Mag**	**Angle**	**Mag**	**Angle**
1	1.0000	0.00	1.0000	-120.00	1.0000	120.00
2	0.9973	0.00	0.9980	-120.02	0.9982	119.99
3	0.9955	0.00	0.9967	-120.04	0.9970	119.99
4	0.9613	-0.04	0.9738	-120.35	0.9750	119.96
5	-	-	0.9736	-120.35	-	-
6	0.9215	-0.11	0.9481	-120.71	0.9491	119.91
7	0.8899	-0.18	0.9277	-121.01	0.9284	119.88
8	0.8899	-0.18	0.9277	-121.01	0.9284	119.88
9	0.8894	-0.17	0.9274	-121.01	0.9281	119.88
10	0.8882	-0.13	-	-	-	-
11	0.8564	0.95	-	-	-	-
12	0.8522	1.10	-	-	-	-
13	0.8795	-0.02	0.9164	-121.00	0.9186	119.89
14	-	-	0.9162	-121.00	-	-
15	0.8787	0.00	0.9156	-121.00	0.9178	119.89
16	0.8591	0.29	0.8955	-120.95	0.8986	119.91
17	0.8586	0.30	0.8950	-120.95	0.8981	119.91
18	-	-	0.8949	-120.94	-	-
19	0.8247	0.85	0.8594	-120.86	0.8645	119.97
20	0.8247	0.85	0.8594	-120.86	0.8645	119.97
21	0.7883	-1.03	0.8232	-122.75	0.8279	118.17
22	0.7059	-1.69	0.7482	-124.10	0.7453	117.21
23	0.8217	0.92	0.8560	-120.85	0.8614	119.98
24	0.8217	0.92	-	-	-	-
25	0.8182	1.00	0.8521	-120.83	0.8580	119.98
26	0.8181	1.00	0.8520	-120.83	0.8579	119.98
27	0.8177	1.01	0.8514	-120.83	0.8574	119.98
28	0.8175	1.02	0.8508	-120.83	0.8572	119.98
29	0.8175	1.02	0.8508	-120.83	0.8572	119.98
30	0.8177	1.01	0.8516	-120.83	0.8576	119.98
31	0.8175	1.01	0.8512	-120.83	0.8574	119.98
32	0.8175	1.01	0.8511	-120.83	0.8574	119.98
33	0.8175	1.01	0.8511	-120.83	0.8574	119.98
34	-	-	0.8510	-120.84	-	-

Table A.24 34-bus unbalanced radial distribution system base case power flows

System	**Value**
Total input	kW : 1690.2 kVAr : 1049.9 kVA : 1989.7
Total load	kW : 1399.5 kVAr : 851.69 kVA : 1638.9
Total losses	kW : 290.69 kVAr : 198.21 kVA : 351.83